The Key Laboratory of Weak Light Nonlinear Photonics,
Ministry of Education

Annual Report 2014

南开大学弱光非线性光子学
教育部重点实验室

Annual Report 2014

The Key Laboratory of Weak Light Nonlinear Photonics,
Ministry of Education

南开大学弱光非线性光子学

教育部重点实验室

▼ 弱光非线性光子学教育部重点实验室学术年会在泰达应用物理研究院召开。（2014.1.4）

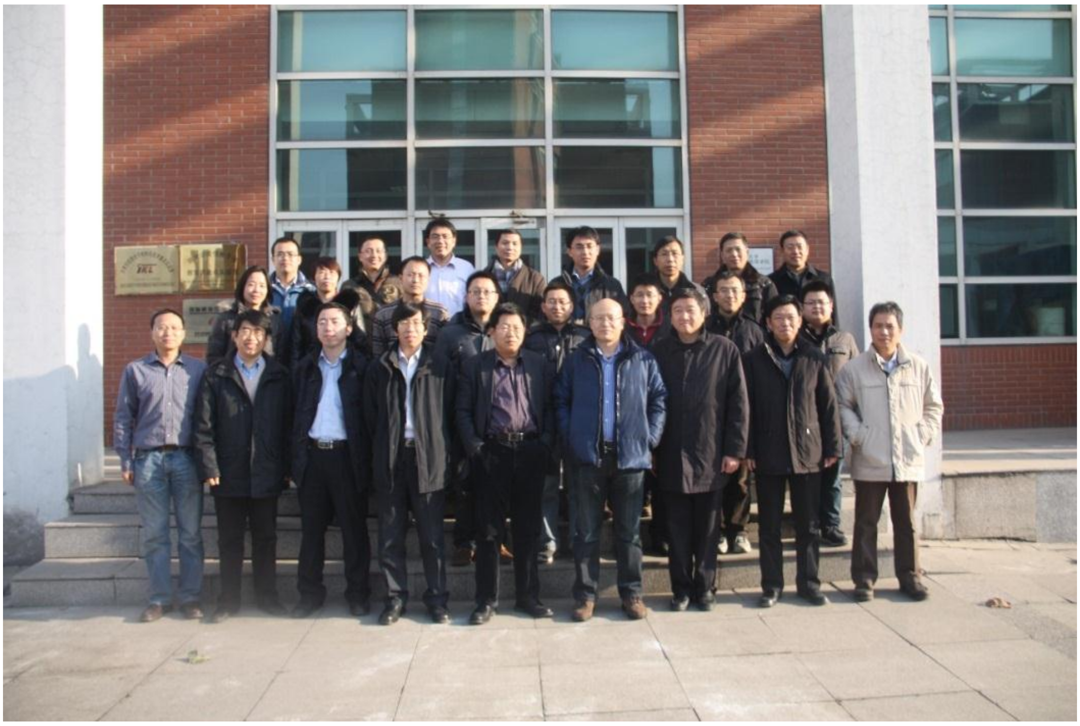

▼ 承办“魅力物理特色南开 2014 夏令营”，20 余名营员对弱光非线性光子学教育部重点实验室进行参观，与教师进行科研方向、科研内容等方面的交流。（2014.7.16）

▼ 承办“2014 年中科协青少年高校科学营南开大学分营”泰达学院实验板块，为 200 余名营员介绍南开物理的特色学科、专业及相关科研进展情况。（2014.7.18）

▼ 973 计划项目“介观尺度下光子行为及新型信息光子器件研究”中期总结会议于泰达应用物理研究院召开。（2014.8.9-8.10）

- 斯洛文尼亚斯特藩研究所的 Blaz Tasic 研究生来弱光非线性光子学教育部重点实验室开展合作研究。（2014.5.6-6.1）

- 美国 University of South Florida 的 Zhimin Shi 教授来弱光非线性光子学教育部重点实验室访问，并在泰达应用物理研究院为师生作两场学术报告。（2014.8.12-8.14）

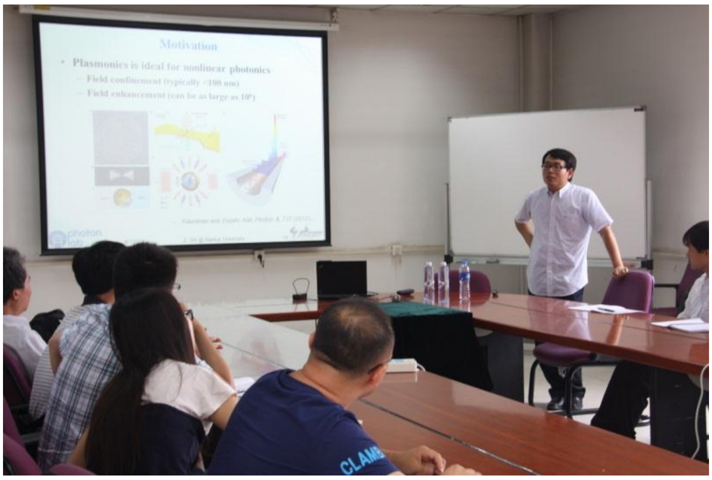

- 泰达应用物理研究院 Romano Rupp 教授邀请雷根斯堡应用科学大学的 Mikhail Chamonine 教授、Heiko Unold 教授和 Rupert Schreiner 来弱光非线性光子学教育部重点实验室访问，并作学术报告，进而探讨了教学、科研合作事宜。（2014.9.20-9.26）

▼ 美国圣路易斯华盛顿大学杨兰副教授来弱光非线性光子学教育部重点实验室访问，并作学术报告。（2014.10.12-10.14）

▼ 美国圣路易斯华盛顿大学 research scientist Dr. Sahin Ozdemir 来弱光非线性光子学教育部重点实验室访问，并作学术报告。（2014.10.13-10.15）

▼ 乌克兰切尔诺夫策国立大学教师 MYKHAILO GAVRYLIAK 博士在弱光非线性光子学教育部重点实验室做博士后研究。（2013.3-2015.2）

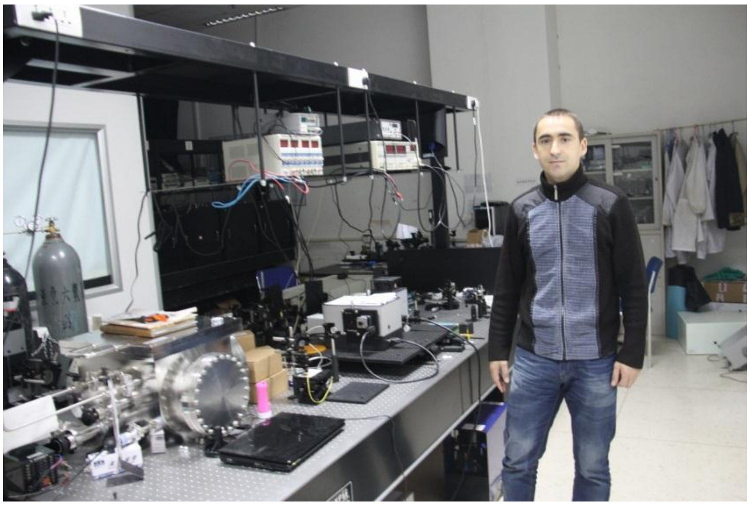

▼ 乌克兰国家科学院 Andriy Ilyin 研究员来弱光非线性光子学教育部重点实验室进行研究工作，为研究院和物理科学学院研究生授课，并作学术报告。（2014.10.9-11.17）

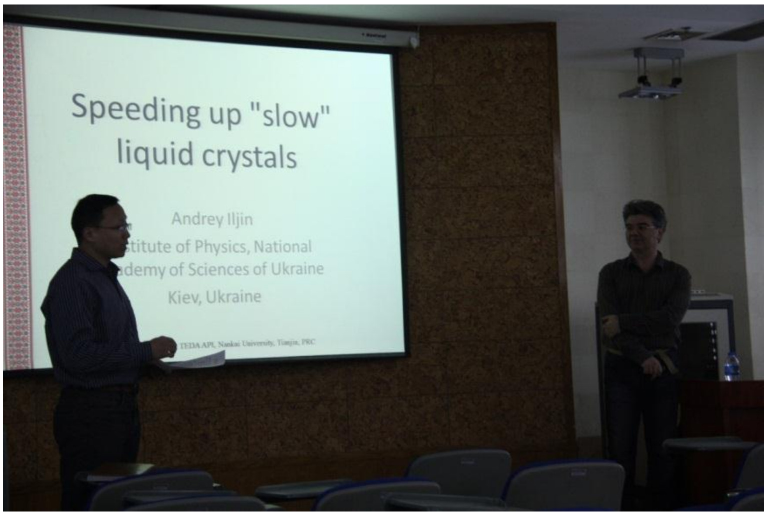

▼ 美国加州大学尔湾分校物理与天文系李绍巍来弱光非线性光子学教育部重点实验室访问，并作学术报告。（2014. 11.26-11.28）

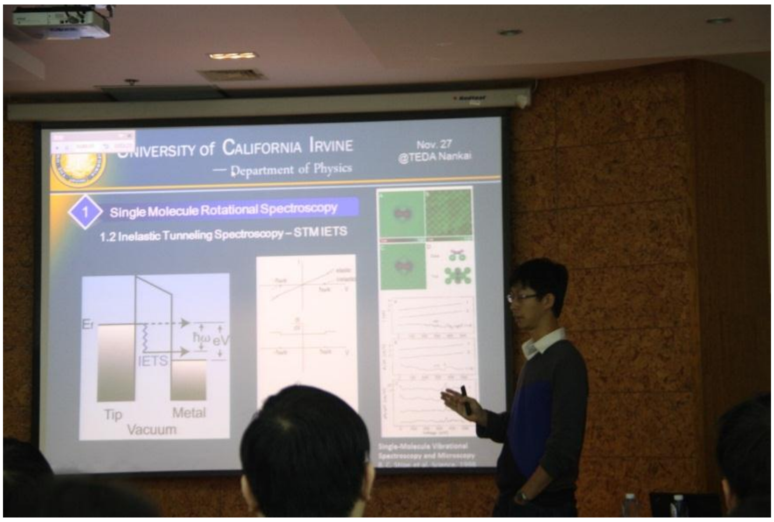

▼ 弱光非线性光子学教育部重点实验室承办的“第一届飞秒激光微构造材料及其器件研讨会”在泰达应用物理研究院召开。（2014.11.29-12.1）

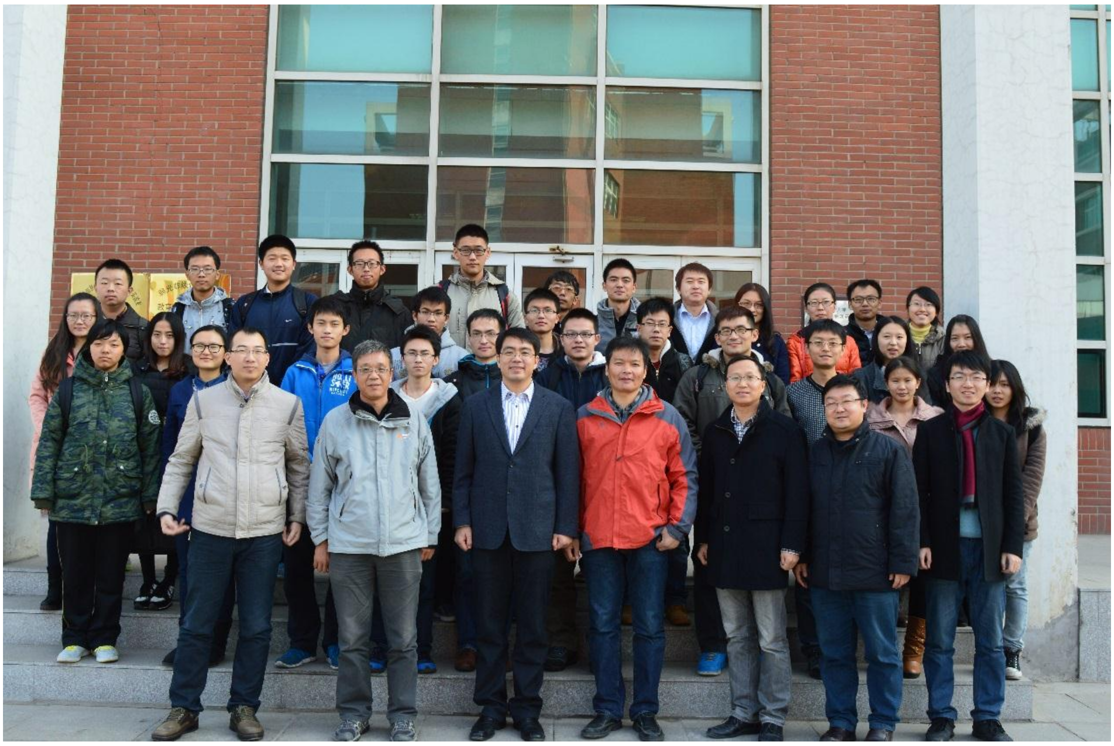

▼ 斯洛文尼亚卢布尔雅那大学数学物理系 Dr. Luka Cmok 来弱光非线性光子学教育部重点实验室访问，并作学术报告。（2014.12.11-12.18）

▼ 美国洛斯阿拉莫斯国家实验室集成纳米技术中心 Hou-Tong Chen 来弱光非线性光子学教育部重点实验室访问，并作学术报告。（2014. 12.14-12.18）

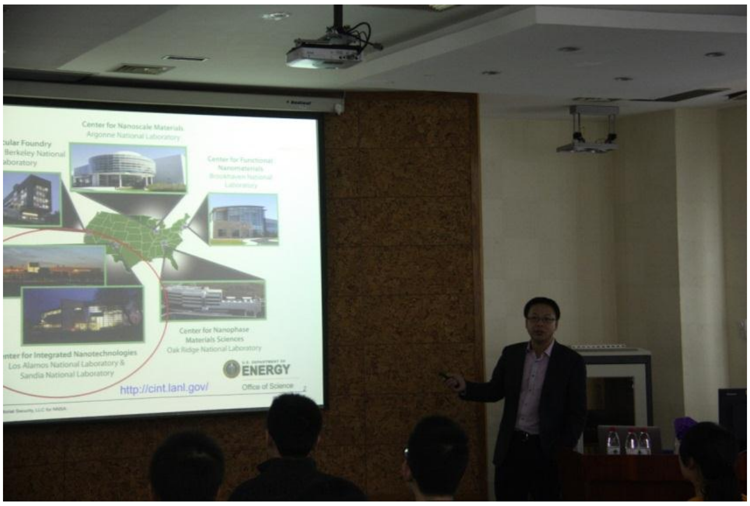

▼ 德国马克斯普朗克智能系统研究所 Na Liu 教授来弱光非线性光子学教育部重点实验室访问，并作学术报告。（2014. 12.18-12.21）

▼ 泰达二中物理兴趣小组 15 余名中学生来弱光非线性光子学教育部重点实验室参加科普教育活动。（2014.12.23）

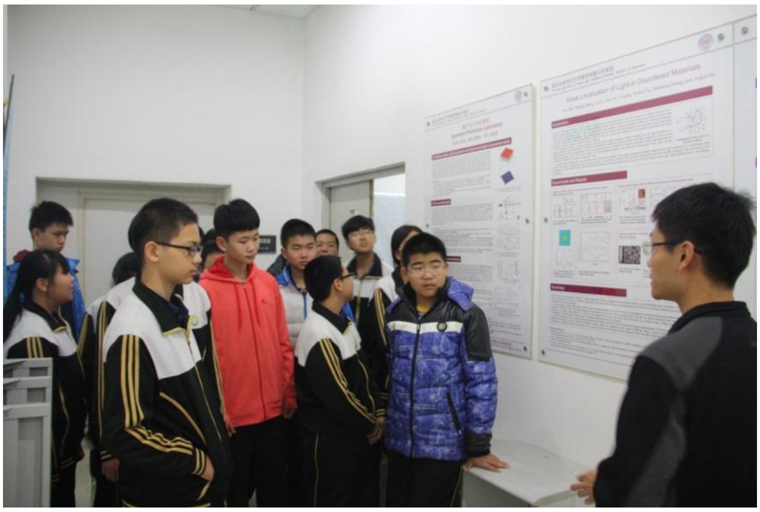

目　录/Contents

人员结构/Organization

实验室主任/Director

许京军 教授

实验室副主任/Deputy Directors

张国权 教授

孙骞 教授

学术秘书/Academical Secretary

禹宣伊 副教授

研究方向负责人/Research Group Leaders

弱光非线性及量子相干光学	许京军	教授
非线性物理与光子技术	田建国	教授
光子学材料及先进制备技术	孔勇发	教授
光谱表征及传感技术	宋峰	教授
光场调控及其应用	王慧田	教授

学术委员会/Academic Committee

主任/Chairman

李树深	院士	（中国科学院半导体研究所）

委员/ Committee Members

薛其坤	院士	（清华大学）
孙昌璞	院士	（中国科学院理论物理研究所）
许宁生	院士	（中山大学）
龚旗煌	院士	（北京大学）
陆卫	研究员	（中国科学院上海技术物理研究所）
徐现刚	教授	（山东大学）
资剑	教授	（复旦大学）
申德振	研究员	（中国科学院长春光学精密机械与物理研究所）
曾和平	教授	（华东师范大学）
田建国	教授	（南开大学）
王慧田	教授	（南开大学）
许京军	教授	（南开大学）

外籍学术顾问委员

D. Kip	教授	德国 Clausthal 工业大学
L. Hessenlink	教授	美国斯坦福大学物理系
R. A. Rupp	教授	奥地利维也纳大学实验物理所
T. Volk	教授	俄罗斯国家晶体研究所
Y. Tomita	教授	日本电气通信大学
K. A. Nelson	教授	美国麻省理工学院

杰出人才/Intelligent Staff

教育部“长江奖励计划”特聘教授

许京军（1999）　王慧田（1999）　陈志刚（2006）

国家杰出青年基金获得者

许京军（1998）　田建国（2001）　王慧田（2003）　李宝会（2009）

教育部“优秀青年教师资助计划”入选者

张国权（2002）　宋峰（2003）

教育部“跨世纪优秀人才培养计划”入选者

许京军（1998）　田建国（2000）　孙骞（2001）　孔勇发（2002）

教育部“新世纪优秀人才支持计划”入选者

张国权（2004）　宋峰（2004）　宋智（2004）　臧维平（2005）
李宝会（2005）　孙甲明（2007）　张心正（2008）　刘智波（2009）
陈璟（2009）　顾兵（2010）　楼慈波（2010）　张天浩（2011）
武莉（2011）　周向峰（2012）　陈树琪（2013）　孙军（2013）

首批新世纪百千万人才工程国家级人选

田建国（2004）

国家海外青年学者合作研究基金获得者

陈志刚（2005）

“天津市授衔专家”称号获得者

许京军（2005）　田建国（2005）

教育部“长江学者和创新团队发展计划”创新团队基金资助

弱光非线性光子学重点实验室人员名录/Name List

研究人员/Scientific Staff（52 人）

许京军 王慧田 田建国 Romano A. Rupp 陈志刚 张国权 孔勇发 孙骞 宋智
宋峰 臧维平 李宝会 舒永春 姚江宏 赵丽娟 曹亚安 孙甲明 张天浩 李玉栋
徐晓轩 张心正 周文远 邢晓东 禹宣伊 余华 吴强 孙同庆 武莉 楼慈波
高峰 刘智波 李祖斌 薄方 齐继伟 叶青 潘雷霆 蔡卫 陈树琪 宋道红
孙军 张玲（兼） 刘士国（兼） 李威（兼） 陈璟 李勇男 刘宏德 王斌
皮彪 任梦昕 涂成厚 周向峰 胡毅

技术人员/Technical Staff（4 人）

陈绍林 马玉祥 张玲 刘士国

行政人员/ administrative Staff（3 人）

梁建 李威 唐柏权

博士生/Ph.D Students（97 人）

蒋鹏翀 冀志超 张琦 杜成林 焦跃健 王杰 王新亚 王丕东 王垒 石彬
潘玉松 吴玉娥 张斌 王萌 潘崇佩 李存波 罗维维 王聪 李文华 夏峰
黄礼刚 李志向 王晓杰 韩彬 刘建基 张明偲 王午登 谭信辉 向吟啸 梁毅
刘鹏翊 杨明 陈战东 窦宜领 徐雷 洪佩龙 辛巍 蒋文帅 邓志超 姜美玲
李占成 刘文玮 于萍 孙腾骞 孙骥文 李毅 郜向阳 陈旭东 李健雄 姚筠
李志莉 赵子宇 徐建 邢飞 郝金龙 韩中兴 兰子鉴 付钰婷 武丽伟 李清连
单排 葛新宇 刘悦 诸玲 郑大怀 崔娇 彭永进 赵明天 邱文娟 李青霄
于彦龙 赵丹丹 闫亚斌 黄绍龙 韩凌云 曹丽萍 易欢 杨金凤 张荣纯 王景声
龚亮 郭丽梅 刘敏 王蒙 黄森鹏 张俊 崔文静 王风萧 钱升霞 任志成
董校 孔令军 潘岳 刘瑞 蔡孟强 司宇 李思黾

硕士生/M.S. Students（181 人）

魏巍 曾强 赵文娟 刘丹 薛淑情 牛林玉 战瑜 郝振中 常朋发 苏菁
裴雨苗 聂伟 廖宏艳 王世彪 左一平 赵丽 马增红 朱葛 金小娜 赵妍
赵国帅 张虹 李莹 李利明 彭伟华 杨浩 王晓欧 高晓梅 徐鹏伟 陈庆全
刘颖 杨淑英 崔伟 曹天祥 刘亭 王杰 彭景阳 高晓光 谢博洋 金晓伟
刘诗可 赵清波 刘远泽 王晓婉 王晨 郑宇 齐鹏飞 高承敏 曾欢欢 杨娜
晏敏 赵连云 陈春晖 陈伦杰 蔚浩义 赵芳 刘瑞雪 马晨欣 董斌 李文华
李秀霞 王鹏 蒋文帅 王群 刘楠 高赫 雷琴 朱闪闪 李金宸 李文灿
李聪聪 刘锦利 吴剑棋 郑玲飞 吴佳坪 赵侨 靳春燕 熊细欢 张晓娜 刘洋
宋晓波 栗亚楠 石亚辉 白宇星 陈静静 郭晓菁 秦娟 王海萍 齐禹纯 李庆红
孙颖 张健铭 张晓雨 江泽清 张心铭 张冠南 要佳莹 马睿 陈慕灵 钟海涛
孔腾飞 宋亚婷 陈艳红 谭庆志 李慧 李清 高飞 杨亚俊 古瑶 刘犇
刘晓芳 李娜 崔晓彤 王庆通 高露 王雄龙 栗瑜梅 司元春 周舰波 高少华
姬静远 孙少君 张勇军 王文庆 商继芳 张亚梅 胡伟 王策 常利芬 落爱青
吴增娜 王晓慧 张逍遥 解雅洁 王力伟 秦娇夷 史更新 黎莎 武迪 唐悦
郝冰雪 张会平 戈进 吴婷婷 李小静 徐海霞 吴学谦 高玲玲 郭辉 张荣
付苏阳 赖翔 宋飞飞 郑颖 周爱华 任杨阳 郭廷珂 赵春兰 李昊宇 郭昊
任爱兵 安双新 宛文顺 巨丹丹 陈展耀 孙希鹏 韩迎东 王文艳 李琼 王丹
王焱坤 吕家琪 张瑜 梁娟 戴凡 高旭珍 王周祥 张会会 李萍萍 冯丹
蔡孟强

承担课题/Projects under Researching

序号	项目名称	项目来源	起止时间	负责人
1	光子束超衍射纳米加工基本原理基础研究	973 项目	2010.1-2014.8	张心正
2	超快激光与硅表面相互作用机理研究	973 项目	2012.1-2014.8	姚江宏
3	纳/微结构中光学非线性增强机理及光调控研究	973 项目	2013.1-2017.12	张国权
4	硅基杂质与缺陷发光中心的构建及器件	973 项目	2013.1-2017.12	孙甲明
5	空间结构光场与微结构的线性和非线性耦合效应	973 项目子课题	2012.1-2016.12	陈树琪
6	新颖动量和角动量光场与微结构相互作用的量子效应	973 项目子课题	2012.1-2016.8	宋智
7	纳米器件制备工艺创新与应用基础研究	973 项目子课题	2012.1-2014.8	李威
8	减反与广谱吸收的黑硅材料研究	973 项目子课题	2012.1-2014.8	吴强
9	基于等离激元结构的材料制备与红外光电转换增强效应研究	973 项目子课题	2013.1-2017.12	宋道红
10	介观结构新型氧化物紫外/深紫外光电探测及器件研究	973 项目子课题	2013.1-2017.12	孔勇发

11	关联光子学微结构的非线性光学特性与调控机理研究	国家重大科学研究计划	2010.1-2014.12	田建国
12	空间结构光场的调控机理、生成技术和新颖性质	国家重点基础研究发展计划子课题	2012.01-2016.08	王慧田
13	多相聚合物溶液体系受限于软膜内的自组装行为研究	国家自然科学基金重大研究计划培育项目	2013.1-2015.12	李宝会
14	弱光非线性光子学材料的缺陷设计与构筑	国家自然科学基金重大研究计划培育项目	2013.1-2015.12	孔勇发
15	大功率DUV－DPL热效应研究	国家自然科学基金重点项目子课题	2012.1-2015.12	宋峰
16	基于微纳器件的飞秒矢量光场及其微纳结构制备研究	国家重大仪器专项项目子课题	2013.1-2016.12	李勇男
17	氧化锌铝纳米粉体及靶材中试技术研究	863计划	2012.1-2014.12	舒永春
18	XXX	科技部	2012.7-2015.7	宋峰
19	弱光非线性光子学科学与技术创新引智基地	111计划	2012.1-2016.12	许京军
20	新型聚合物纳米复合材料及其光子学微结构研究	国家国际科技合作专项	2012.1-2014.12	张心正
21	新型乳腺癌早期预警系统的建立及防治方法的合作研究	国家国际科技合作专项	2012.6.1-2015.5.31	田建国
22	非中心对称宽禁带氧化物高压光伏效应的合作研究	国家国际科技合作专项	2013.4-2015.12	孔勇发

23	Peter Hertel（MS2010NKDX023）	教育部“海外名师”项目	2010.1-2014.12	许京军
24	基于非线性光学表面波的可调谐长程传播表面等离子激元及其应用研究	国家自然科学基金	2012.1-2015.12	张天浩
25	碳基纳米材料超快光学非线性及其非线性光学显微成像研究	国家自然科学基金	2012.1-2015.12	刘智波
26	高增益光子晶体自发辐射增强效应及其生物传感应用	国家自然科学基金	2012.1-2015.12	周文远
27	通过非均匀随机介质体系的图像传输与成像研究	国家自然科学基金	2012.1-2015.12	张国权
28	介电纳米波导/金属纳米微结构复合体系光传输性能及其应用	国家自然科学基金	2012.1-2015.12	孙骞
29	无序非线性增益介质中光子局域化及上转换随机激光的研究	国家自然科学基金	2012.1-2015.12	张心正
30	可见光催化剂微观表面光生载流子特性的原位定量研究	国家自然科学基金	2012.1-2015.12	曹亚安
31	基于特异介质的矢量光场生成与调控	国家自然科学基金	2012.1-2015.12	陈璟
32	锂在铌酸锂晶体中的扩散行为及其应用研究	国家自然科学基金	2012.1-2014.12	孙　军
33	自适应光脉冲整形技术在电子加速中的应用研究	国家自然科学基金	2013.1-2016.12	臧维平
34	用于提高硅基太阳电池效率的表面等离子体激元增强量子剪裁效应研究	国家自然科学基金	2013.1-2016.12	宋峰

35	基于二阶姜－泰勒效应的非中心对称磷酸盐功能晶体化合物的设计、合成、结构与性质	国家自然科学基金	2013.1-2016.12	孙同庆
36	原子层沉积稀土氧化物和硅酸盐纳米复合薄膜硅基MOS电致发光器件的研究	国家自然科学基金	2013.1-2016.12	孙甲明
37	飞秒矢量光场的超衍射极限微结构制备及特性研究	国家自然科学基金	2013.1-2016.12	涂成厚
38	基于石墨烯表面等离激元的红外光场调控研究	国家自然科学基金	2014.1-2017.12	蔡卫
39	基于时间分辨定量成像的太赫兹声子极化激元的研究	国家自然科学基金	2014.1-2017.12	吴强
40	微米尺寸铌酸锂晶体回音壁模式微腔的制备和光学非线性增强研究	国家自然科学基金	2014.1-2017.12	薄方
41	多维光量子态空域调控及量子刻蚀研究	国家自然科学基金	2014.01-2017.12	李勇男
42	基于全内反射结构的石墨烯光学性质及其应用研究	国家自然科学基金	2014.01-2017.12	田建国
43	梯度渐变超材料光学特性调控及其应用	国家自然科学基金	2014.01-2017.12	陈树琪
44	高效率TiO2基光热协同催化剂	国家自然科学基金	2014.01-2017.12	曹亚安
45	单相多波长可调硼酸盐基荧光粉的合成与发光性能调控	国家自然科学基金	2014.01-2017.12	武莉
46	锂在铌酸锂晶体中的扩散行为及其应用研究	国家自然科学基金青年基金	2012.1-2014.12	孙 军
47	聚合物分散液晶体系的多光子聚合超衍射加工研究	国家自然科学基金青年基金	2013.1-2015.12	李威

48	基于宽场显微荧光成像技术的一氧化氮亚硝基化修饰对激活的嗜中性粒细胞质钙调节机制的研究	国家自然科学基金青年基金	2013.1-2015.12	潘雷霆
49	抗紫外光损伤铌酸锂晶体及其应用研究	国家自然科学基金青年基金	2013.1-2015.12	刘宏德
50	标量和矢量光束作用下复合超材料非线性光学特性研究	国家自然科学基金青年基金	2014.01-2016.12	程化
51	石墨烯超快载流子动力学及其在全光调制中的应用研究	国家自然科学基金青年基金	2014.01-2016.12	鄢小卿
52	基于超颖材料等离子体激元的可控发光研究	国家自然科学基金青年基金	2014.01-2016.12	任梦昕
53	非线性周期结构中的离散光涡旋现象研究	国家自然科学基金青年基金	2014.01-2016.12	宋道红
54		教育部新世纪优秀人才支持计划	2012.1—2014.12	张天浩
55		教育部新世纪优秀人才支持计划	2012.1—2014.12	武莉
56	基于新结构、新机理的超材料光学特性研究	教育部新世纪优秀人才支持计划	2014.1-2016.12	陈树琪
57	基于非线性光学表面波的可调谐长程传播表面等离子激元	教育部高等学校博士点基金（博导类）	2013.1-2015.12	张天浩
58	金属纳米颗粒对稀土掺杂液晶发光的增强	教育部高等学校博士点基金（博导类）	2014.1-2016.12	宋峰
59	基于光刻技术的细胞图案化控制及其数值仿真研究	教育部高等学校博士点新教师基金	2012.1-2014.12	潘雷霆
60	复合等离子体超材料非线性光学特性及其应用研究	教育部高等学校博士点新教师基金	2013.1-2015.12	程化

61	类石墨烯型光学微结构制备及光传播特性研究	教育部高等学校博士点新教师基金	2013.1-2015.12	宋道红
62	超颖材料中等离子体激元对荧光发射偏振的调控研究	教育部高等学校博士点新教师基金	2014.1-2016.12	任梦昕
63	基于近红外光谱的油料农作物品质快速检测的全固定式仪器研发和应用	天津市科技支撑计划重点项目	2012.4-2015.3	徐晓轩
64	农用轻便型全自主飞行器及配套设备的研发	天津市科技支撑计划重点项目	2014.4-2017.3	王斌
65	焦场调控及其微纳结构制备研究	天津市自然科学基金重点基金	2013.04-2016.03	李勇男
66	基于物联网的近海多参数水质分析仪及监测网络	天津市科技兴海项目	2012.1-2014.12	徐晓轩
67	云计算模式下基于手机信令的智能交通指挥与突发事件感知平台	天津市信息化项目	2012.1-2014.12	徐晓轩
68	一种无人机用低成本可见近红外成像光谱仪的研发	天津市科技特派员项目	2014.10-2015.9	王斌
69	楔形超声角锥驱动的光纤结构的滤波色散特性及其应用	天津市自然科学基金	2012.4-2015.3	高峰
70	矢量光场下的表面等离子共振及表面增强拉曼研究	天津市自然科学基金	2012.4-2015.3	齐继伟
71	石墨烯宽带光学非线性及其应用研究	天津市自然科学基金	2013.4-2016.3	刘智波
72	动态调控杂化超材料等离子激元诱导透明及其应用	天津市自然科学基金	2013.4-2016.3	陈树琪
73	LED用单相全色荧光粉的制备与发光性能调控	天津市自然基金	2014.4-2017.3	武莉

74	天津 131 人才工程第一层次	天津市人事局	2013.1-2015.12	宋峰
75	局域等离子激元微结构优化设计和表面增强应用研究	教育部重点实验室开放课题	2012.7-2014.6	王斌
76	高温度稳定性铌酸锂电光 Q 开关研制	中电 27 所	2013.4-2014.12	孙军
77	钢管制造信息化系统及管端参数测量系统的研究与开发	横向课题	2012.5-2014.10	田建国
78	溅射薄膜性能测试	横向课题	2014.1-2014.12	舒永春
79	高纯高密度氧化镁靶材制备	横向课题	2014.1-2015.12	舒永春
80	NK-7 铌酸锂电光晶体的研制	横向课题	2014.12-2015.12	孙军
81	光纤薄壁微腔的制备及其应用研究	南开大学基本科研业务费平台重大科学研究项目	2014.1-2014.12	高峰

仪器设备平台/Facilities

仪器设备名称	规格型号	购置时间
激光器工作站	899-29	2005.09
飞秒激光器	VF-T2S	2000.08
皮秒激光器	PY61	2003.11
纳秒激光器	Panther OPO	2003.11
光纤激光器	PLY-20-M	2003.11
可调频再生放大器	Spitfire F-1K	2000.04
时间分辨光谱及瞬态吸收光谱系统	Spectrapro.300i	2000.04
光谱分析仪	AQ6315A	2005.09
显微拉曼光谱仪	MKI2000	1998.09
分子速外延生长炉	Riber Compact 21T	2003.09
提拉法晶体生长炉	研制	2002.04
晶体切割研磨抛光系统	Logitech 系列	2001.06
扫描探针显微镜	Nanoscope IIIa	2006.08

注：除开放基金外，所有仪器设备均为有偿使用

研究工作报告/Scientific Report

非线性物理与光子技术/ Nonlinear Physics and Photonics Techniques

负责人：田建国

本方向涉及石墨烯光学性质、等离子激元、超材料、光学传感、光在介质中的传播、光子带隙材料、亚波长微结构等方面。本年度发表论文 18 篇；申请或授权专利 6 项。在研课题经费 1671.5 万元。2014 年度“非线性物理与光子技术”方向主要在以下方面取得了进展:

In this field, we mainly focused on optical properties of graphene, plasmonics, metamaterials, optical sensor, one dimensional photon crystal, and sub-wavelength microstructure. 18 papers have been published in international academic journals, and 6 patents applicanted. The total researching founds are 16.715 millions. This year, we obtained some important results as following:

(1) 石墨烯光学性质在全内反射结构下具有强的偏振依赖和吸收增强。将石墨烯置于棱镜底部，在全内反射结构下，对于 s 和 p 入射偏振光将产生不同的反射行为，而且石墨烯对 s 偏振光有着更强的吸收。我们利用全内反射下石墨烯对介质折射率异常敏感的光学现象，通过优化石墨烯厚度和光路结构，获得了非常高的折射率测量分辨率(折射率分辨率 1.7×10^{-8}，灵敏度 4.3×10^{7} mV/RIU)。结合微流控技术，实现了超灵敏单细胞实时流动传感。石墨烯的这一重要应用可以使癌细胞在其发展成为癌症之前被精确的识别出来，为癌症的预防提供了一条新途径。

On the basis of the polarization-dependent absorption of graphene under total internal reflection, we designed a graphene-based optical refractive index sensor with high resolution of 1.7×10^{-8} and sensitivity of 4.3×10^{7} mV/RIU, as well as an extensive dynamic range. This highly sensitive graphene optical sensor enables label-free, live-cell, and highly accurate detection of a small quantity of cancer cells among normal cells at the single-cell level and the simultaneous detection and distinction of two cell lines without separation. It provides an accurate statistical distribution of normal and cancer cells with fewer cells. This facile and highly sensitive sensing refractive index may expand the practical applications of the biosensor.

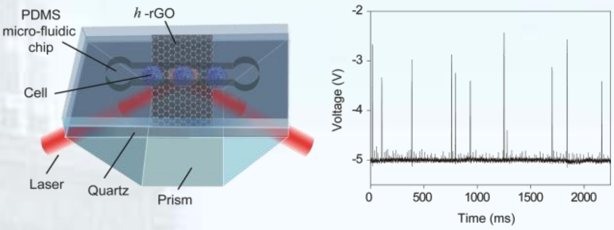

图 1（a）基于石墨烯的超灵敏单细胞实时流动传感结构图；（b）正常淋巴细胞和淋巴癌变细胞的测试结果，其中突起的大信号为癌变细胞。

Fig. 1 The schematic of the graphene-based optical single-cell sensor, which is a PDMS micro fluidic chip/ h -rGO/quartz sandwich structure on the prism. (b) Discrete time-dependent changes in voltage that correspond to mixed lymphocytes and Jurkat cells as they roll across the h-rGO detection window

(2) 使用简并和非简并泵浦-探测技术，通过差分信号对泵浦光偏振依赖性的研究揭示石墨烯中光激发载流子在能带结构中分布的演化。在激发态上，光激发载流子在动量空间的初始分布是各向异性的，随着载流子的弛豫，这种各向异性分布很快的变成各向同性。在远离激发态的能态上，热载流子在整个非平衡态中都是各向同性的。使用

倾斜的光束作为泵浦光束，差分信号的泵浦偏振依赖性并不改变，这说明石墨烯对平面内光场和平面外光场的吸收系数是一致的。

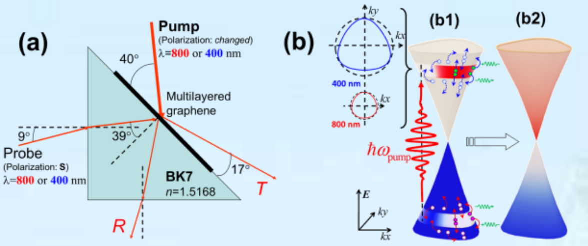

图 2.（a）飞秒时间分辨泵浦-探测测量中使用的测量布局，探测光以非全反射的方式入射到石墨烯样品上，泵浦光倾斜的入射到石墨烯片上。(b)光激发载流子的演化，b1,载流子从价带被激发到导带时的初始分布。b2,经过热化过程后载流子的分布，左上角两幅插图表示 400nm 和 800nm 光对应石墨烯能态的三角翘曲结构。

Fig. 2. (a) Experimental configuration. the probe beam was coming from the nontotal internal reflection at the interface between the graphene layer and a prism, and the pump beam was obliquely incident into the graphene sample. (b) Schematic illustration of the photoexcited carrier distribution evolution in the graphene electronic band structure. (b1) The anisotropic distribution of carriers generated by a linearly polarized beam and potential scattering pathway for carriers. (b2) Isotropic carrier distribution. Upper left inset: Electronic band curvature for excitation of 400-nm and 800-nm pulses.

Femtosecond degenerate and nondegenerate pump-probe spectroscopy in graphene reveals the evolution ofphotoexcited carrier distribution in the energy band during relaxation: the initial occupation of photoexcited carriers centered at the excitation state is anisotropic in momentum space; this anisotropic distribution rapidly relaxes through an intermediate state argued to be fully isotropic in the energy band due to phonon-involved cascade scattering. In addition, the experiment suggests that graphene optical absorbances for in-plane and out-of-plane optical fields are identical.

(3) 我们在理论上提出了通过不同超材料功能结构的组合来实现非对称透射，通过应用 L 型金属天线和双棒纳米天线形成的双层超薄杂化超材料，在近红外波段实现了对线偏振光的宽带单向透射。基于我们的基本理论，通过调节超材料结构参数就能在任意波段下实现非对称透射，为非对称透射器件的设计提供了指导。通过对不同超材料功能结构的组合，使得结构层与层的相对位置对于非对称透射的实现基本没有影响，从而极大的降低了对于微纳加工工艺的要求。基于双层超薄杂化超材料的宽带类二极管非对称透射的实现，为微纳光学领域非对称透射器件的研究提供了新的可能性。

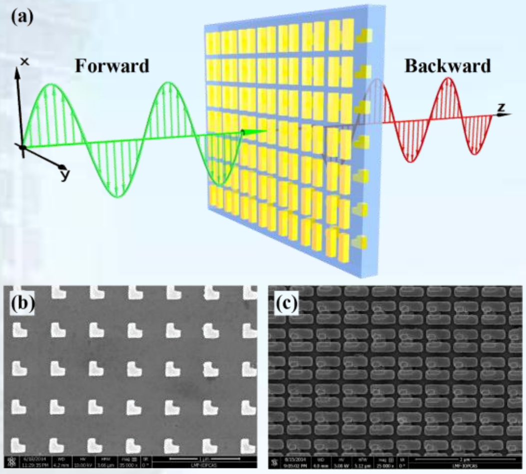

图 3（a）双层杂化超材料非对称透过示意图;（b）L 型天线 SEM 结构示意图;(c）双棒纳米天线 SEM 结构示意图。

Fig. 3 (a) Schematics of the proposed two-layer hybrid metamaterial for x-polarized propagation in the forward and backward directions. (b) Scanning electron microscopy (SEM) image of the L-shaped metallic particle and (c) the double nano antenna.

We present the underlying theory, the design specifications, and the experimental demonstration of the broadband diodelike asymmetric transmission of linearly polarized light in the near-infrared regime. This result is achieved through the use of a two-layer hybrid metamaterial, composed of an L-shaped metallic particle and a double nano antenna. The experimental results are shown to agree well with the theoretical predictions and the simulated transmission spectra. The realization of the diodelike asymmetric transmission can be attributed to the combination of two independently functioning metallic structures, which are shown to perform their respective function even when shifted away from perfect alignment. This work offers a further step in developing broadband diodelike asymmetric transmission for use in electromagnetic devices.

(4) 我们提出了一种在单平面结构上实现光的相干调控的方法。对于周期性旋转纳米天线阵列，当某一旋性圆偏光入射时，透射场除了该旋性的光还会产生遵循异常折射定律的相反旋性的光。利用这一性质，可以将两束相反旋性的圆偏光在某一角度下同时入射在天线阵列中，透射光场将同时出现两束入射光的叠加。通过调节入射光的相对相位，就可以对透射光进行强度调制；通过调节入射光的振幅比，就可以改变光强的调制度。由于这种调制方法具有普遍性，在含有正常光的相位调控超材料中具有广泛的应用，例如可以完全调控超透镜透射光、超材料全息图的光强。

We present a method of fully controlling anomalous refraction efficiency by introducing an interferometric cross-modulation for two circularly polarized incident lights based on plasmonic metasurfaces. Theoretical analyses and numerical simulations indicate that the anomalous and ordinary refracted beams generated from two opposite-helicity incident beams will have a superposition for certain incident angles, and the anomalous refraction efficiency can be dynamically controlled by changing the relative phase of the incident sources. As the incident wavelength nears the resonant wavelength of the plasmonic metasurfaces, two equal-amplitude incident beams with opposite-helicity can be used to change the anomalous refraction efficiency. Otherwise, two unequal-amplitude incident beams with opposite-helicity can be used to fully control the anomalous refraction efficiency. This work may offer a further step in the development of tunable anomalous refraction.

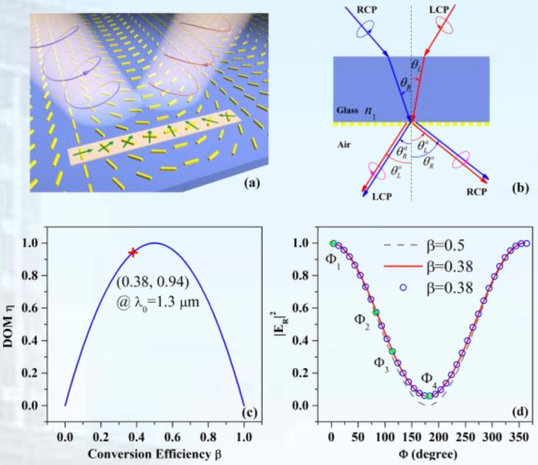

图 4（a）旋转纳米天线阵列结构超材料；（b）两束相反旋性圆偏光在某一角度入射，透射光会同时包含部分两束入射光；（c）调制度的大小与偏振转换率的关系；（d）在 1.3 微米光入射的情况下，右旋透射光的光强与两束入射光相对相位的关系。

Fig.4 (a) Schematic illustration of a representative plasmonic metasurface used as a model in our theory and simulation. (b) Schematic illustration of the anomalous and ordinary refracted lights for both LCP and RCP incident beams, which are superposable at all eigenstates. (c) Calculated DOM η with varying the conversion efficiency β. The red marker shows the values of $\beta = 0.38$ and $\eta = 0.94$ at the resonant wavelength of 1.3 μm. (d) Calculated (dashed gray line and solid red line) and simulated (blue circles) intensity $|E_R|^2$ of the RCP transmitted light for varying relative phase δ when $\beta = 0.38$ and $\beta = 0.5$.

(5) 我们提出了简单的双层金属微结构实现了基于四带耦合的宽带近完美吸收器，且存在广角特性，并通过引入非线性材料实现了其吸收特性的动态调控。同时，由

于结构设计中对称性的考虑，该吸收器对偏振弱依赖。通过对结构模式进行拆分，我们得到了四个带的来源，对应的吸收谱与理论有较好一致性。

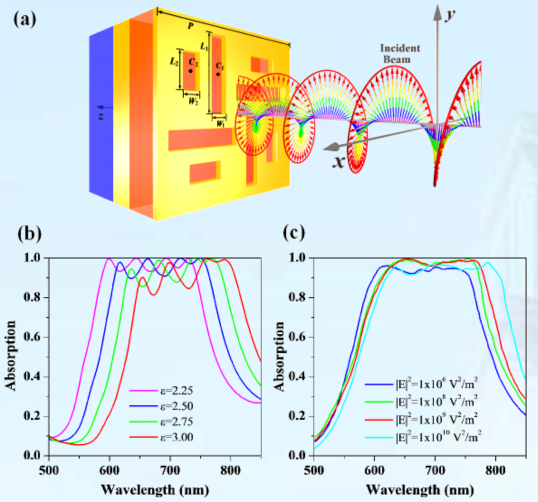

图 5（a）宽带近完美吸收器结构示意图；（b）不同电介质层介电常数对吸收谱的影响；（c）不同入射光造成的吸收谱动态调谐。

Fig.5 (a) Unit cell of the designed MPA showing the geometry parameters: P = 500 nm, L1 = 220 nm, L2 = 100 nm, W1 = 50 nm, and W2 = 50 nm. The coordinate of the two cut-out slots are C1(65, 110) nm and C2(155, 110) nm. Simulated absorption spectra for the different (b) dielectric constants ε of the dielectric spacer and (c) incident intensities of a single continuous beam.

We present the design and analysis of a polarization-insensitive and wide-angle broadband nearly perfect absorber by planar metamaterial in the visible regime. The bandwidth of absorption spectrum can be effectively expanded by combining multiple resonant elements. The forming mechanisms of the broadband metamaterial perfect absorber (MPA) are also demonstrated by the hybridization of the plasmonic system. The resonance of the broadband MPA can be dynamically tuned by varying the intensity of the incident beam. This kind of all-optically tunable perfect absorber will help to overcome some of the limitations of customary designs developed so far.

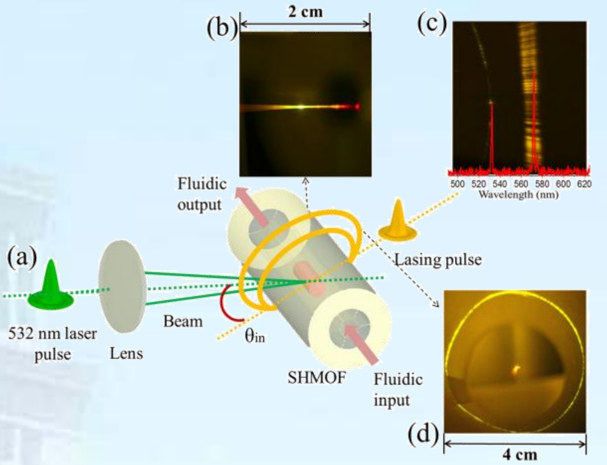

图 6 (a)微结构光纤染料激光器系统结构示意图与(b-d)激射光斑图。

Fig.6 (a) Experimental layout of the SHMOF based laser system. See text for explanation. (b) Lasing image of stimulated transverse SHMOF through an added long pass filter. (c) Typical spectrum of SHMOF laser with background of a filtered lasing on a plane screen. (d) The filtered output of the lasing ring on a conical screen on the lateral side of the SHMOF.

(6) 本工作将常规的基于微光纤谐振腔设备集成压缩到 MOF 平台，来增强稳定性和克服脆弱的不足，在简易型空心微机构光纤汇总实现微腔染料激光器。新型空心微结构光纤具有特殊的结构：包含中心一个大的六角形空气孔和六个环绕的花瓣形包层空气孔。微流通道由新型微结构光纤的中心孔组成，通过将罗丹明 6G 染料液体选择性填充进入新型微结构光纤的中心孔实现，纳秒脉冲激光器测量泵浦染料液柱。由于新型微结构光纤特殊的几何机构，其中环绕中心的纳米厚度的二氧化硅环与液芯填充的光纤作为微流体腔集成化一体，有强束缚光能力，和低损耗传输以及单模式光传导特性。由于传导光在亚波长波导中具大的倏逝场和强的光束缚能力，泵浦光横向耦合情况下，与围绕微环谐振腔的中心孔微通道中染料

相互作用，产生激射光，得到强的圆环辐射和低至 185nJ/pulse 的激光。进一步改进微环尺寸，得到可调的激光发射。通过改进谐振腔结构，优化泵浦方式，设计实现低阈值，高效率，发射稳定的一种微腔染料激光器。与目前报道的激光器相比嵌入 SHMOF 中的微环谐振腔提供可比性的坚固轻便架构，易控的微流体。

We scale down conventional microfiber based resonator setups into an integrated MOF platform, to address stability and overcome the fragility issues. The realization of a microcavity dye laser within a simplified hollow-core microstructural optical fiber (SHMOF) is demonstrated. Specifically, the SHMOF comprises a large hexagonal core with six surrounding crown-like air holes. The fiber core which is filled with a microfluidic gain medium (Rhodamine 6G) plug is lateral pumped by a nanosecond pulse laser. The silica microring surrounding the hollow core of the SHMOF plays the role of an unusual microring resonator. With sub-wavelength designs, this structure exhibits not only obvious features of large evanescent field but also strong ability in optical confinement. By transversely pump light to the internal cavity composed of microfluidic gain medium, which is surrounded by the silica microring in the fiber, both strong radial emission and low threshold laser (185 nJ/pulse) are achieved. Furthermore, a tunable laser emission is realized by changing the size of microring of a SHMOF. With the overlap area increases and the mode number decreases, low transmission losses and stable lasers are obtained. Compared with other recent reported optofluidic ring resonators, this microring resonator embedded in the SHMOF provides a competitive structure of tight, solid and easy to microflow control.

(7) 将石墨烯与超表面向结合，我们设计了一种简单的一维石墨烯超表面，即石墨烯光栅结构。通过改变石墨烯光栅的宽度，可以调控反射光的相位和振幅。通过增加金属衬底，可以获得约 2π 相位调控范围。改变介质衬底厚度，在合适的厚度，可以使同时获得较高反射率和 2π 的相位调控范围。利用石墨烯宽度与相位之间的关系，我们设计了平面透镜，实现了光聚焦。

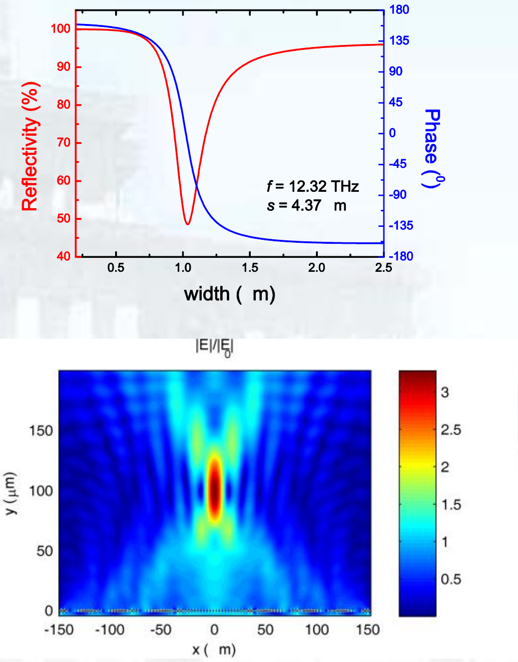

图 6 (a)反射率与相位随石墨烯宽度的变化规律,(b)用设计好的石墨烯超表面实现聚焦。

Fig.6 (a) Reflectivity and phase as the function of graphene ribbon width. (b) Focusing by designed graphene metasurface.

Considering graphene and metasurface together, we designed a simple graphene metasurface made of graphene ribbons. The phase and amplitude of the reflective light can be tuned by the graphene ribbon width. If we use a reflection pattern by adding a metal mirror under the substrate, the phase change can be modulated from 0 to 2π. At a certain substrate thickness, we can get 2π phase change as well as the higher reflectivity. By using the relation of graphene ribbon width and phase, we designed a flat lens and achieved focusing effect.

(8) 折射率成像在光通讯、光波导检测和生物医学领域都有着非常广泛的应用，高分辨率、高精度的折射率显微分布信息在相关研究、应用领域具有十分重要的意义。大多数传统的折射率成像方法都对通过样品的透射光进行检测，这些透射式的方法无法应用于非透明的样品，当应用于生物医学领域时必须对样品进行切片处理。我们提出了一种折射率显微分布测量的方法。该方法是一种基于全内反射，结合了投影放大、显微技术、扫描技术，得到物体定量的、高分辨率的、高精确度的折射率显微分布信息的技术。由于是一种反射式的测量方法，不需要检测物体的透射光信息，因而能够适用于非透明物质；被测量的物体也不需要制成切片或薄片，或者进行标记、着色处理，适合于定量的测量物质折射率显微分布测量。在此基础上，发展了一种光纤折射率定量测量的方法。利用扫描聚焦折射率显微方法对光纤进行折射率成像测量，适合于普通光纤，折射率对称分布及非对称分布的折射率渐变光纤。利用这种方式实现光纤折射率成像测量，空间分辨率高、测量准确等优势,能够适用于多种类型的光纤。该方法的空间分辨率达到了1μm，折射率精度达到了0.002。

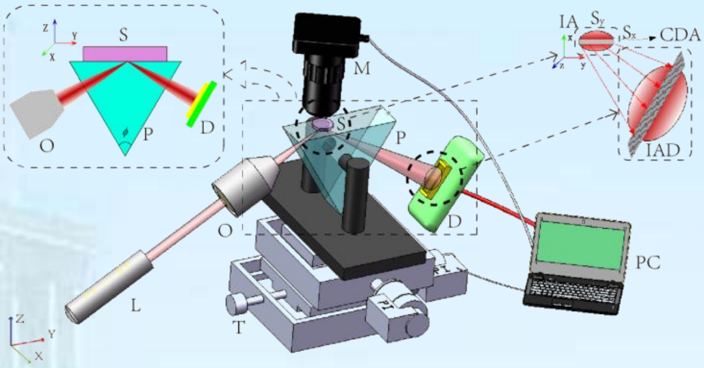

图8 扫描聚焦折射率显微装置图。

Fig.8 Structure diagram of scanning focused refractive-index microscopy.

Refractive index imaging is widely used in optical communication, assessment of optical waveguides, and biomedical fields. The detailed information of refractive index distribution with high spatial resolution and accuracy is essential in related researches and application fields. Most traditional refractive index imaging strategies tends to collect the transmission light that passes though the sample. Therefore the techniques cannot be applied to non-transparent samples. Bio-tissues should be cut into slices when the transmission-type techniques are used in the field of biomedical research. Here we propose a refractive index distribution measurement method. This total internal reflection-based method combines projection magnification, microscopy and scanning technique to quantitatively obtain refractive index distribution with high spatial resolution and accuracy. This method can be applied to non-transparent samples because of its detection of its reflected light. The target samples are free from being cut into slices, labeled or dyed in quantitatively refractive index distribution measurement with our method. A quantitatively optical fiber detection method is proposed on this basis. The scanning focused refractive index microscopy can be applied to step-index fibers, and graded-index optical fibers with symmetry and asymmetry refractive index distribution. The refractive index imaging of optical fibers with this technique has the advantages of high spatial resolution, high accuracy, and can be applied to a wide range of optical fibers. The spatial resolution of the technique is 1μm; and the RI accuracy is 0.002.

光子学材料及先进制备技术/ Photonics Materials and Advanced Fabrication Techniques

负责人：孔勇发

本方向涉及多功能光学晶体、低维功能材料、软物质、硅基发光、微晶玻璃陶瓷、光子学微结构等方面。本年度发表论文22篇，获得授权专利2项，在研课题经费1557万元。取得的代表性成果如下：

In this field, we mainly focused on the multi-functional optical crystals, low-dimensional functional materials, soft matter, silicon based light emitting materials, nano-crystalline glass ceramics, and photonic microstructure. 22 papers were published in international academic journals, and 2 patents issued. The total researching founds are 15.57 million. This year, we obtained some important results, they are mainly shown as following:

本年度我们用提拉法生长了一系列铋镁双掺铌酸锂晶体，在保持Bi_2O_3的掺杂比例为1.0 mol%不变的前提下，调节MgO的掺杂比例为3.0 mol%, 5.0 mol%和6.0 mol%，分别标为：LN:$Bi_{1.0}$,$Mg_{3.0}$，LN:$Bi_{1.0}$,$Mg_{5.0}$ 和 LN:$Bi_{1.0}$,$Mg_{6.0}$。通过单透镜法测量晶体的抗光损伤阈值，如图1所示，LN:$Bi_{1.0}$:$Mg_{6.0}$在光强密度为7.26×10^6 W/cm^2条件下未发生明显光斑畸变，这表明和现有的单掺镁或锆铌酸锂晶体相比该晶体有较好的抗光损伤能力。同时采用双光束干涉法，测量铋镁双掺铌酸锂晶体的光折变性能，激光波长488 nm，光强密度400 mW/cm^2，如图2所示，$Bi_{1.0}Mg_{6.0}$ 的光折变衍射效率达到18%，而响应时间仅为 170 ms。该研究结果打破了光损伤又称作光折变的固有观念，证明光损伤不等于光折变，为设计高抗光损伤非线性晶体指明了正确方向。

We have designed and grown a series $LiNbO_3$ crystals co-doped with Bi_2O_3 and MgO (LN:Bi,Mg), the doping concentrations of MgO were 3.0 mol%, 5.0 mol% and 6.0 mol% while kept the doping concentration of Bi_2O_3 as 1.0 mol%, labeled as LN:$Bi_{1.0}$,$Mg_{3.0}$, LN:$Bi_{1.0}$,$Mg_{5.0}$ and LN:$Bi_{1.0}$,$Mg_{6.0}$, respectively. As shown in Fig. 1, the optical damage resistance of LN:$Bi_{1.0}$:$Mg_{6.0}$ can reach to 7.26×10^6 W/cm^2, just as high as that of LN:Zr and higher than mono-doped LN:Mg. In the meantime, Fig. 2 shows that the photorefractive diffraction efficiency of LN:$Bi_{1.0}$:$Mg_{6.0}$ reaches 18% while the response speed is only 170 ms. The experimental results indicate that LN:$Bi_{1.0}$:$Mg_{6.0}$ has both high resistance to optical damage and high photorefraction, which proves that optical damage doesn’t equal photorefraction.

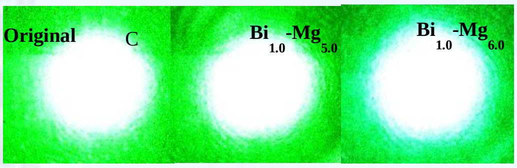

图 1 铋镁双掺铌酸锂晶体抗光损伤示意图，激光波长 532 nm，光强密度：7.26×10^6 W/cm^2。

Fig.1 Distortion of transmitted laser beam spots after 5 min of irradiation. The laser wavelength is 532 nm with light intensity of 7.26×10^6 W/cm^2.

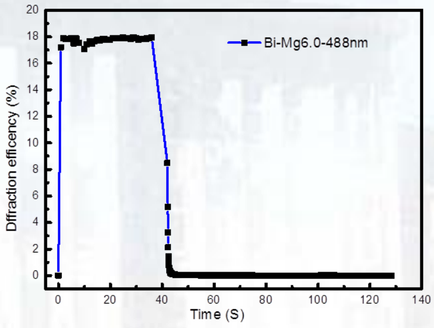

图 2 铋镁双掺铌酸锂晶体的衍射效率随写入与擦出时间的变化，激光波长 488 nm，光强密度 400 mW/cm^2，写入时间 170 ms。

Fig2 The time dependence of photorefractive diffraction efficiency of LN:$Bi_{1.0}$,$Mg_{6.0}$ crystals. Incident light is at 488 nm with light intensity of a single beam approximately 400 mW/cm^2. The writing time is as short as 170 ms.

我们开展了新型深紫外非线性光学晶体的探索，采用助熔剂缓冷方法和自发成核技术生长出尺寸达28 mm×14 mm×5 mm、具

有非中心对称结构的$CsLa(PO_3)_4$单晶。实验表明，$CsLa(PO_3)_4$晶体具有引人注目的深紫外吸收边，短至167 nm。$CsLa(PO_3)_4$多晶粉末的倍频强度约为KDP的一半。该晶体平行于(100)和(001)面完全解理，这与晶体结构对称性和不同化学键键强的较大差别有关。我们还调查了该晶体的热稳定性和比热容。为了解该晶体的构效关系，我们分析了晶体中不同多面体的偶极矩，通过密度泛函理论进行了能带、态密度和光学性质等的计算。

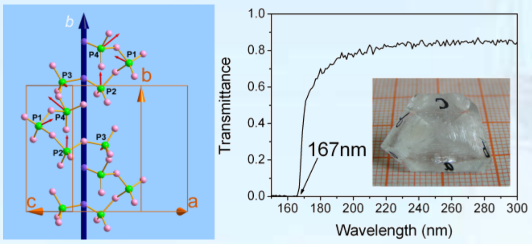

图 3（左）$CsLa(PO_3)_4$ 晶体结构中沿 b 轴延伸的$[PO_3]_\infty$螺旋链（红色箭头指示了不同氧多面体偶极矩的方向和大小）；（右）$CsLa(PO_3)_4$ 晶体的真空紫外透过谱（插图为生成态晶体）。

Fig.3 (Left) The $[PO_3]_\infty$ helical chain along the b axis in $CsLa(PO_3)_4$ (The red arrows indicate the approximate direction and magnitude of the dipole moments) and (Right) the VUV transmission spectrum of $CsLa(PO_3)_4$ (The inset is the as-grown single crystal).

To explore new deep-ultraviolet (deep-UV) nonlinear optical crystals, $CsLa(PO_3)_4$ crystal with noncentrosymmetric crystallographic structure was grown by spontaneous nucleation using the flux method and slow-cooling technique. A single crystal with a size of 28 mm ×14 mm ×5 mm was easily obtained. Two perfect cleavage behaviours of $CsLa(PO_3)_4$ crystal were found and the reason was discussed from the point of view of bond length and symmetry. The thermal stability and specific heat capacity of $CsLa(PO_3)_4$ were investigated. $CsLa(PO_3)_4$ crystal remarkably exhibits a deep-UV cutoff edge of 167nm, which is one of the shortest values among phosphates to date. Polycrystalline powder of $CsLa(PO_3)_4$ presents a moderate second harmonic generation (SHG) response, which is about one half of that of KH_2PO_4 (KDP). The analysis of the dipole moments for the polyhedra and the theoretical calculation by the density functional theory (DFT) were performed for understanding the structure-function relationships in $CsLa(PO_3)_4$ crystal.

采用TSSG-SC技术生长出Nd^{3+}掺杂的$KGdP_4O_{12}$单晶。该晶体具有C2/c空间群对称性，晶胞参数为a = 7.812(2) Å，b = 12.307(3) Å，c = 10.474(2) Å，β = 110.84(3)°，Z = 4。IR与Raman光谱也证实磷氧多面体形成了环状结构。我们分析了晶体的元素含量，计算了Nd^{3+}的分凝系数；同时确定了晶体的形态。我们研究了$Nd:KGdP_4O_{12}$晶体的热稳定性、比热和热导率等热学性质。$Nd:KGdP_4O_{12}$晶体展现出宽带吸收特征，798nm的吸收峰的半峰宽达到14.8nm，使得该晶体非常适于AlGaAs激光二极管泵浦。我们还研究了该晶体的发光性质，5at% Nd^{3+}掺杂的$KGdP_4O_{12}$晶体具有长的荧光寿命（300 μs）和高的量子效率（96%）。

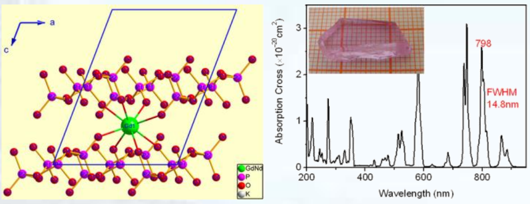

图 4（左）$Nd:KGdP_4O_{12}$ 晶体中稀土离子的配位环境；（右）$Nd:KGdP_4O_{12}$ 晶体在室温下的吸收谱（插图为用于测量的晶体）。

Fig.4 (Left) The coordination of rare earth ion in $Nd:KGdP_4O_{12}$ crystal and (Right) the absorption spectrum of $Nd:KGdP_4O_{12}$ crystal at room temperature.

A single crystal of Nd^{3+}-doped $KGdP_4O_{12}$ was successfully grown with the top-seeded solution growth and slow cooling (TSSG–SC) technique. It crystallizes in space group C2/c with cell parameters a = 7.812(2) Å, b = 12.307(3) Å, c = 10.474(2) Å, β = 110.84(3)° and Z = 4. The IR and Raman spectra also indicated that the phosphoric polyhedra of $Nd:KGdP_4O_{12}$ has a cyclic symmetry. The chemical composition of the crystal was analyzed and the distribution coefficient of

Nd^{3+} was calculated. The crystal morphology of $KGdP_4O_{12}$ was identified using X-ray diffraction. The compound has good thermal stability to 920 °C. Its specific heat and thermal conductivity were determined for potential applications. The spectral properties of $Nd:KGdP_4O_{12}$ indicates that it exhibits broad absorption and emission bands, which are attributed to low symmetry of the crystal. The broad absorption band around 798 nm has a full-width at half-maximum (FWHM) of 14.8 nm and is suitable for AlGaAs laser diode pumping. Moreover, 5 at% Nd^{3+}-doped $KGdP_4O_{12}$ crystal has a long luminescence lifetime of 300 μs and a high quantum efficiency of 96%.

我们在Mn^{2+}激活的$KMgBO_3$荧光粉中发现了Mn^{2+}的反常发光，经过光谱研究表明，该反常发光主要是由于Mn^{2+}的d-d跃迁中自旋和宇称禁戒部分解除。完成了$KSr_4(BO_3)_3:Sm^{3+}$系列橙红色发光材料的制备。Rietveld结构精修表明，掺入的Sm^{3+}离子占据Sr2(8c)和Sr3(4a)晶体学格位。Sm^{3+}的非辐射浓度猝灭是通过电偶极相互作用实现的。对Eu^{3+}在同时含有Zn^{2+}和Ba^{2+}的$Ba_2ZnB_2O_6$基质中的格位占据情况进行了研究，结果表明尽管Ba^{2+}的离子半径接近Eu^{3+}，但是Eu^{3+}更倾向于占据Zn1和Zn2位置。由于具有较大离子半径的Eu^{3+}取代较小离子半径的Zn^{2+}格位，使得晶场强度增加，发射光谱出现红移。

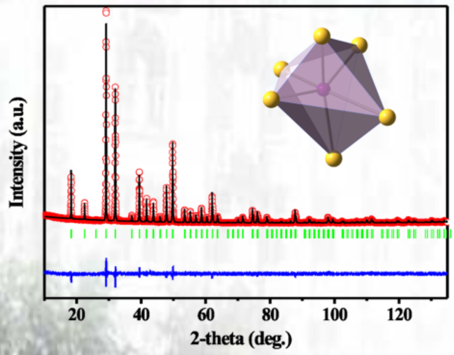

图 5 $KMgBO_3:0.09Mn^{2+}$的结构精修图，插图为 MgO_6 多面体。

Fig.5 Rietveld refinement result of $KMgBO_3:0.09Mn^{2+}$, and the inset is the structure of $[MgO_6]$ octahedron.

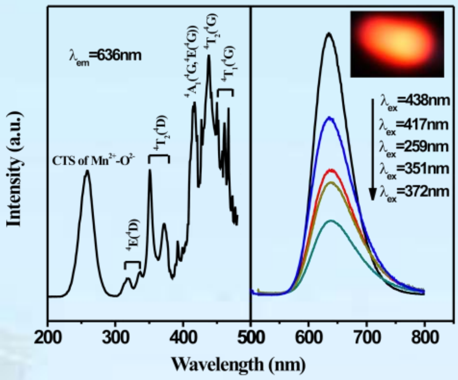

图 6 $KMgBO_3:0.09Mn^{2+}$的激发光谱和发射光谱。插图为 351nm 激发下样品光斑照片。

Fig.6 Typical excitation spectra monitored at 636 nm and emission spectra excited at different wavelengths of $KMgBO_3:0.09Mn^{2+}$ phosphor. Inset is the corresponding luminescence photograph for the sample excited at 351 nm in the dark with bright red color as seen by the naked eye.

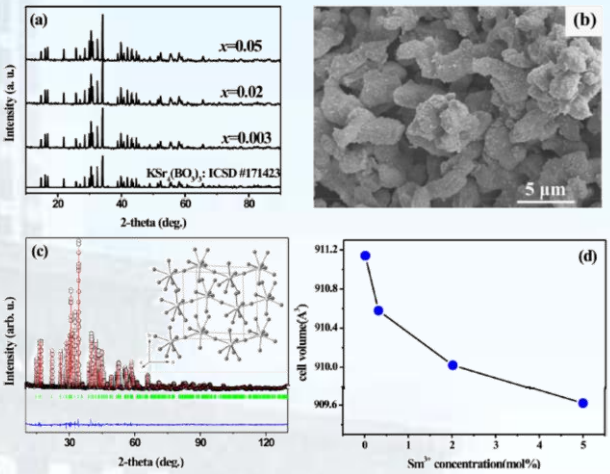

图 7 (a) $KSr_4(BO_3)_3:xSm^{3+}$ (x = 0.003, 0.02, 0.05)荧光粉的 X 射线衍射图。(b) $KSr_4(BO_3)_3:0.02Sm^{3+}$荧光粉的 SEM 形貌图。(c) $KSr_4(BO_3)_3:0.02Sm^{3+}$的结构精修图，插图为 Sr^{2+}的配位环境。(d) $KSr_4(BO_3)_3:Sm^{3+}$的体积随 Sm^{3+}浓度变化曲线。

Fig.7 (a) The XRD patterns of $KSr_4(BO_3)_3:xSm^{3+}$ (x = 0.003, 0.02, 0.05) phosphors. (b) SEM morphology of $KSr_4(BO_3)_3:0.02Sm^{3+}$ phosphor. (c) Final Rietveld refinement plots of the $KSr_4(BO_3)_3:0.02Sm^{3+}$. Small circles (o) correspond to experimental values, and the continuous lines, the calculated pattern; vertical bars (|) indicate the position of Bragg peaks. The bottom trace depicts the difference between the experimental and the calculated intensity values. Inset is the coordination environments of Sr^{2+} with O^{2-}. The large white balls are Sr^{2+} ions, the small black balls are O^{2-} ions. (d) the dependence of cell volume of $KSr_4(BO_3)_3:Sm^{3+}$ to the Sm^{3+} concentration.

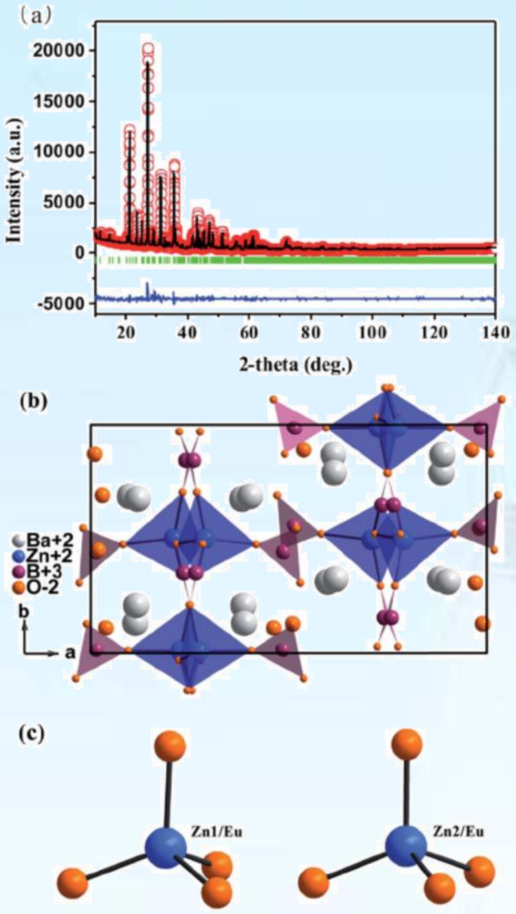

图 8 (a) $Ba_2ZnB_2O_6$:0.05Eu^{3+}的结构精修图。(b) $Ba_2ZnB_2O_6$沿 c 轴的晶体结构投影。(c) 两种不同 Zn^{2+}/Eu^{3+}离子的配位环境。

Fig.8 (a) Rietveld refinement plot on the XRD pattern of $Ba_2ZnB_2O_6$:0.05Eu^{3+}. (b) Crystal structure projection of $Ba_2ZnB_2O_6$ along c axis. (c) The coordination environments of two different Zn^{2+}/Eu^{3+} ions.

An abnormal photoluminescence is observed in Mn^{2+} activated $KMgBO_3$ phosphors. It is indicated by photoluminescence properties that the abnormal strong emission is because of the strong relaxation of spin and parity forbidden d-d transitions of Mn^{2+}. A series of $KSr_4(BO_3)_3$:Sm^{3+} orange reddish phosphors are synthesized by tranditional solid state reaction process. Rietveld on step XRD indicates that the doped Sm^{3+} ions occupy Sr2(8c) and Sr3(4a) sites in $KSr_4(BO_3)_3$ host. The nonradiative concentration quenching among two nearest Sm^{3+} centers occurs via electric multipolar interactions. As for the site occupancy of Eu^{3+} in $Ba_2ZnB_2O_6$, which contains both Zn^{2+} cation and Ba^{2+} cation, it is disclosed by Rietveld refinement that Eu^{3+} is preferred to occupy Zn1 and Zn2 sites though the radius of Zn^{2+} is smaller than that of Eu^{3+}. When the large Eu^{3+} ion occupy Zn site, the volume of the crystal structure will be expanded and the polyhedron will be distorted, which will result in the increase the crystal field strength. As a consequence, a red shift will be observed in Zn-based phosphors.

我们在掺稀土氟化物纳米晶结构的研究基础上，主要研究了掺稀土氟化物纳米晶结构对稀土离子发光特性的调控。以单掺Yb^{3+}离子和 Yb^{3+}-Tb^{3+}共掺为对象，用“热诱导-腐蚀法”制备了不同浓度掺杂的氟化物纳米晶颗粒。首先针对单掺 Yb^{3+}离子的纳米晶材料，通过对 1YbGC 和 5YbGC 中的纳米晶结构和 Yb^{3+}离子电荷分布的研究，分析了Yb^{3+}离子分布对 Yb^{3+}-Yb^{3+}离子对合作上转换发光的影响，得出 Yb^{3+}离子之间的距离、之间的敏化作用是影响它们之间能量传递的主要因素。其次，Yb^{3+}离子作为敏化中心，在单掺 Yb^{3+}样品的研究基础上，讨论了Yb^{3+}-Tb^{3+}共掺的纳米晶材料。通过纳米晶结构的研究，提出了纳米晶结构中两种不同的三中心分布情况。这两种分布的主要区别在于涉及到的两个 Yb^{3+}离子之间是否有相互作用。随后基于两种不同分布，提出了相应的能量传递模型。当两个 Yb^{3+}离子之间无相互作用时，三中心能量传递发生在一个 Tb^{3+}离子和两个无相互作用的 Yb^{3+}离子之间，遵循 CET 模型；当两个 Yb^{3+}离子之间存在很强的相互作用时，三中心能量传递发生在一个 Tb^{3+}离子和一个 Yb^{3+}-Yb^{3+}离子对之间，遵循 AET 模型。不同能量传递模型的提出解释了以前文献中存在的争议性问题。最后，通过近红外量子剪裁和上转换荧光光谱的分析，并由相应的荧光发射强度和泵浦功率之间的依赖关系验证了本章所提的两种三中心能量传递模型的正确性。同时，通过对不同能量传递机制下荧光寿命的测量和发光量子效率的计算，得知三中心中 Yb^{3+}离子

之间的敏化作用促进了量子效率的提高。遵循 AET 能量传递机制的材料更适合用在太阳能上以提高太阳能电池的转化效率。

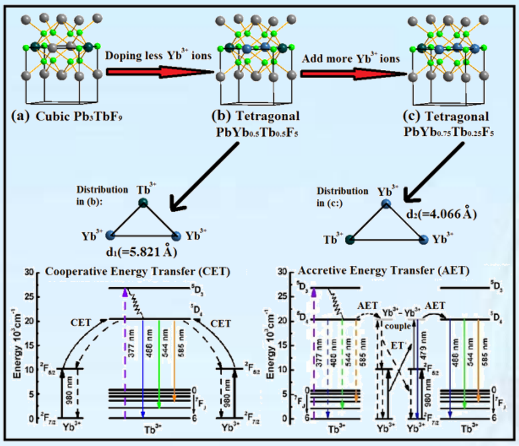

图 9　稀土离子 Tb^{3+}和 Yb^{3+}之间的能量传递方式与其所处的晶格场结构之间的关系。

Fig.9 The relationship between energy transfer of Tb^{3+}/Yb^{3+} process and crystal field structure.

Three-center energy transfer for upconversion and NIR quantum cutting has been investigated systematically in Yb^{3+}-Tb^{3+} co-doped tetragonal $PbYb_xTb_{1-x}F_5$ nanocrystals. Firstly we studied the structure effect on cooperative upconversion luminescence of Yb^{3+}-Yb^{3+} couples in singly Yb^{3+} doped samples and it is found that the sensitization between Yb^{3+} ions can be modulated by the nanocrystal structures. Then based on the distributions of three centers in tetragonal $PbYb_xTb_{1-x}F_5$ nanocrystals, the cooperative and accretive energy transfer mechanisms are proposed. In terms of energy distribution between one Tb^{3+} ion and two non-interacting Yb^{3+} ions, the double-photon excitation and second-order nonlinear processes are observed in CET pathway for upconversion and NIR quantum cutting luminescence, respectively. While it is different in AET pathway, both the upconversion and NIR quantum cutting emission intensities increase linearly with the excitation power because of the energy transfer between one Tb^{3+} ion and an Yb^{3+}-Yb^{3+} couple. The AET process is observed and verified in this work for the first time. Applying rate equations in these models, it explained both the upconversion and quantum cutting experiment phenomena perfectly. Our work clarifies the previous controversies in excitation power dependence of NIR quantum cutting luminescence intensities. And the results that the calculated luminescence quantum efficiency in AET quantum cutting process is much higher than that in CET process (134% and 104%, respectively), can be applied to the study of conversion efficiency in c-Si solar cells.

对于 Er^{3+}/Yb^{3+}共掺的发光材料，980 nm 激光激发时既可以在可见光范围产生上转换发光，也可以在近红外波段产生下转换发光，二者存在竞争关系，如何调控二者相对强度一直困扰科学工作者。研究利用熔融淬火法制备了一系列掺杂不同 Er^{3+}/Yb^{3+}浓度的氟氧化物玻璃陶瓷，测量了样品在 980 nm 激光激发下的上转换及下转换发射光谱，发现改变 Er^{3+}的掺杂浓度可以调控上下转换发光强度，在此基础上提出上下转换发光的能量传递模型。

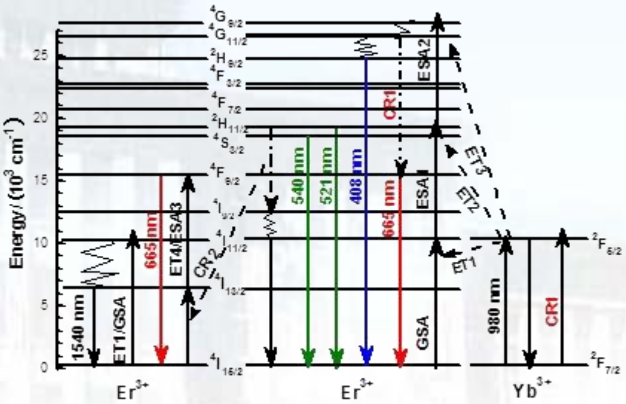

图 10　980 nm 半导体激光器激发下 Er^{3+}/Yb^{3+}共掺玻璃陶瓷材料的能量传递过程。

Fig.10 The energy transfer processes in Er^{3+}/Yb^{3+} co-doped glass ceramics under the excitation of 980 nm laser.

The competitive process of UC and DC emission can be modulated by Er^{3+} concentration in the oxyfluoride glass ceramics co-doped with Er^{3+}/Yb^{3+}. It is found that the energy transfer processes of the UC and DC emission are different in samples with different Er3+ concentration, which clarifies the previous disagreements about the UC and DC energy transfer processes in Er^{3+}/Yb^{3+} co-doped materials. The blue and green UC emissions belong to three-photon and two-photon absorption, respectively. In addition, the red UC emission results from the three-photon absorption for lower Er^{3+} concentration, but it is a difference process for the higher Er^{3+} concentration. The two-photon absorption dominates gradually with increasing the Er^{3+} concentration. Meanwhile, the cross relaxation and multi-phonon relaxation of RE ions could emerge, which enhances the DC emission at 1540 nm. Consequently, the intensities of UC and DC emissions can be modulated by changing Er3+ doping concentration, which benefits for UC or DC materials selection.

制备了不同Pb和Cd比值的一系列样品，通过Raman和FTIR分析了Pb^{2+}和Cd^{2+}在玻璃形成中的不同作用，研究了氟化物含量的改变对稀土掺杂氟氧化物玻璃微结构的影响。结果表明，在玻璃熔融过程中，Cd^{2+}破坏$[SiO_4]$和$[AlO_4]$之间的桥氧，吸引O^{2+}进入玻璃网络，最终形成四配位；Pb^{2+}将把F^-吸引到自己周围，形成大量无规则排列的Pb-F键。在热处理时，Pb-F键整齐排列，以β-PbF_2晶相析出，形成微晶玻璃。

要扩大氟氧化物微晶玻璃在激光介质中的应用，急需找到减小微晶散射的方法。针对以上研究背景，对微晶的散射效率进行研究，比较了Rayleigh散射模型，Mie散射模型和离散偶极子(DDA)模型计算的散射效率，确定了离散偶极子模型作为氟氧化物微晶玻璃散射效率研究的理论基础。随后，从实验和理论模拟中获得散射效率并进行比较，实现了实验和理论的拟合，验证了离散偶极子模型适合研究氟氧化物微晶散射效率这一观点，并利用离散偶极子模型的理论成功解释了在微晶玻璃中一直存在的“超透明”现象。最后，利用离散偶极子理论模拟的结果给出了散射效率随玻璃陶瓷物理参数的变化规律，并得到了散射效率最低的条件。

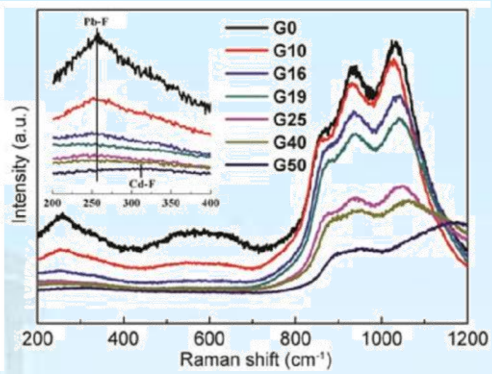

图 11 不同CdF_2含量的玻璃材料的拉曼光谱，插图为200-400 cm^{-1}区间的拉曼光谱放大图。

Fig.11 Raman spectra of OFGs with different CdF_2 contents. Inset is Raman spectra in the 200-400 cm^{-1} region.

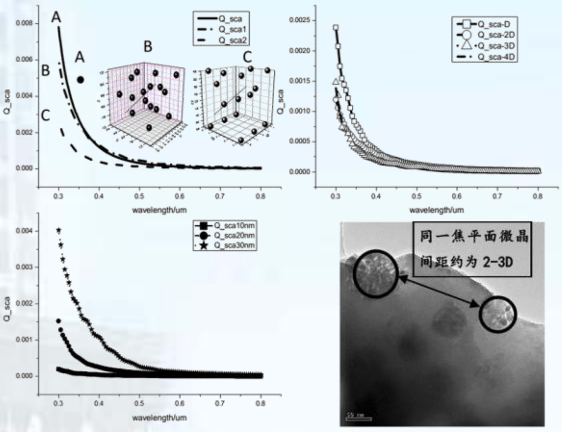

图 12 微晶玻璃中散射效率的研究。(a)单个微晶以及不同周期性单元分布玻璃陶瓷中，散射效率随波长变化关系；(b) 相同周期性单元分布时不同微晶间距下散射效率随波长变化关系；(c) 周期性单元分布时，不同微晶尺寸散射效率随波长变化关系；(d) 掺 Er3+氟氧化物玻璃陶瓷的 TEM 图像。

Fig.12 Scattering efficiency per particle in a periodic unit with different distances and radius between two particles and the TEM figure of fluoride nanocrystals in glass ceramic. (a)Different scattering efficiencies with different particles' distributions and separated particle;(b) Different scattering efficiencies per particle in a periodic unit with different distances between two particles;(c) Different scattering efficiencies with different radius;(d)TEM figures of fluoride nanocrystals in glass ceramic with doped Er^{3+}.

DTA results reveal that the glass ceramics based on β-PbF_2 crystalline can be obtained when CdF_2 content is less than 16 mol%. The in fluence of Pb^{2+} and Cd^{2+} on the glass network structure is analyzed by FTIR and

Raman spectra. As classical network modifiers, Pb^{2+} breaks the Si–O–Si bond, while Cd^{2+} mainly breaks the Si–O–Al bond. Moreover, Pb^{2+} has intense attraction to F^-, which leads to Pb^{2+} bonding with F^-. After the phase separation, Cd^{2+} remains in oxide matrix because it is surrounded by O^{2-}. Proper amount of CdF_2 has the advantage in improving the stability of the glasses and its crystallization, which is significantly important to control the crystallization in fabricating transparent OFGCs. Based on the research results, we can control and modify the formation process of fluoride nanocrystals through the introduction of other metal cations. It is significant for designing glass network structure and studying luminescent properties of fluoride nanocrystals in fabricating transparent OFGCs.

Three methods have been introduced to calculate the scattering efficiency: Rayleigh, Mie and discrete dipole approximation. First of all, we make a comparison between these three models and ascertain the discrete dipole approximation the best way to deal with the scattering in oxyfluoride vitroceramics. Then, we measured the scattering efficiency from experiments and compared it with the simulated results to ensure that the theory is suitable for our samples. Later on, based on the theoretical calculation in discrete dipole approximation, we try to explain the ultra-transparency in oxyfluoride vitroceramics and get a satisfied result. In the end, we make some exploration of the relation between scattering efficiency and factors of vitroceramics to find the condition for lowest scattering efficiency.

我们使用模拟退火方法对线形ABC三嵌段共聚物受限在球形纳米孔内的自组装行为进行了系统研究。发现在中性孔壁或当孔壁对两端嵌段A、C同时具有吸引作用时，共聚物始终形成表面带有圆形补丁结构的纳米粒子。而且补丁的数目和大小可以通过改变孔径的大小以及共聚物和孔壁的相互作用进行调节。提出了利用体相形成三色层结构的线形ABC 三嵌段共聚物受限在球状纳米孔内自组装形成补丁粒子的方法。

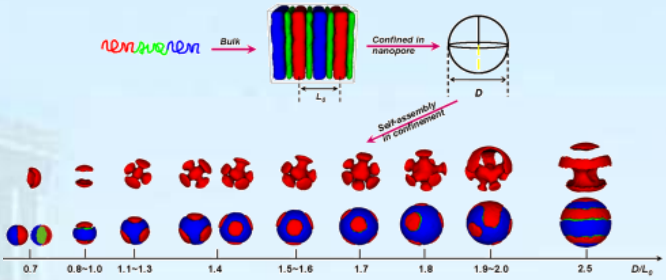

图 13 ABC 三嵌段共聚物受限在球形纳米孔内自组装形成的典型形态。

Fig.13 Typical morphologies formed with the self-assembly of linear ABC triblock copolymers confined in spherical nanopores.

The self-assembly of linear ABC triblock copolymers confined in spherical nanopores is studied using a simulated annealing technique. A variety of patchy nanoparticles and multiple morphological transitions are identified. The size of each patch increases periodically. The number of patches also increases with increasing the wall selectivity. The distribution of the patches on the surface of a given particle is highly symmetric. A series of entropy-driven morphological transitions is predicted. Furthermore, it is found that the overall patchy morphology is largely controlled by the volume fraction of the middle B-block, while the internal structure is largely controlled by the volume fraction ratio of the two terminal blocks. Our study demonstrates that the size of nanopores, the pore-wall selectivity, and the copolymer composition could be utilized as effective means to tune the structure and properties of the anisotropic nanoparticles.

我们利用原子层沉积技术优化制备了SiO_2、ZnO、Al_2O_3、TiO_2、Gd_2O_3、Tb_2O_3和Er_2O_3薄膜等基础薄膜材料，在对各类氧化物薄膜的光学和电学性能的系统研究基础上，利用ALD技术从原子层尺度精确配比

制备出应用于硅基发光器件的多种功能薄膜，比如$ZnO:Al_2O_3$复合透明导电薄膜、TiO_2:Al_2O_3 high-k介质缓冲复合薄膜、稀土掺杂的$SiO_2:Re_2O_3$纳米层状发光复合薄膜。今年我们首次全部利用原子层沉积技术在硅衬底上构建了由透明导电薄膜、high-k复合介质缓冲薄膜、以及稀土掺杂的氧化硅薄膜构成的硅基MOS结构复合薄膜电致发光器件，获得了高效率的绿色和红外硅基电致发光，其中$ZnO:Al/TiO_2:Al_2O_3/SiO_2:Tb/Si$绿色MOSLED，发光阈值电流为纳安量级，器件的量子效率大于15%。同时我们与德国开姆尼茨德累斯顿罗森道夫研究中心合作，用我们的ALD方法制备的SiO_2:Tb薄膜，结合标准硅CMOS工艺制备了$ITO/SiO_2:Tb/SiON/Si$ MOS结构电致发光器件。采用ALD方法制备的SiO_2：Tb绿色电致发光器件的外量子效率达到了已报道的热氧化和离子注入方法获得的同类硅基MOS绿色电致发光器件的最高水平。最近利用以ALD方法在Tb_2O_3原子层旁边精确定位生长Al_2O_3原子层进行共掺杂来局部微调稀土离子周围的发光环境，可以将可激发的稀土离子数量提升一倍。

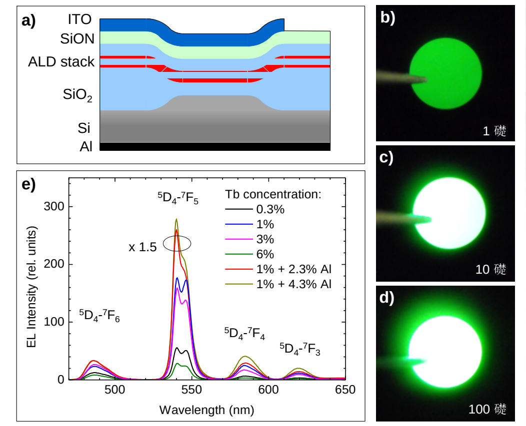

图 14 采用 ALD 和标准 CMOS 工艺制备的高效率 SiO_2:Tb MOS 结构电致发光器件。

Fig.14 Efficient SiO_2:Tb MOSLED prepared by ALD and standanrd MOS technology.

Based on the comprehensive study of the optical and electrical properties of different oxide films, such as SiO_2、ZnO、Al_2O_3、TiO_2 、Gd_2O_3 、Tb_2O_3 and Er_2O_3 prepared by atomic layer deposition technology in the past years. Composite functional nanolaminate films, such as $ZnO:Al_2O_3$ transparant conductive layers, $TiO_2:Al_2O_3$ dielectric buffering layers and the rare-earth doped SiO_2 luminescent layers were prepared by precisely adjusting the atomic layer ratio in the multiple layer films. Highly efficient green electroluminescence (EL) devices were prepared on silicon substrate with a multiple layered MOS structure of $ZnO:Al/TiO_2:Al_2O_3/SiO_2:Tb/Si$，the threshold current for EL emission is only 1 nA with the external quantum efficiency above 15%. In addition， silicon based MOSLEDs with a $ITO/SiO_2:Tb/SiON/Si$ structure were prepared by standard CMOS techonology in collaboration with Helmholtz-Zentrum Dresden-Rossendorf, in which the SiO_2:Tb layer were grown by our ALD technology. The external quantum efficiency reaches the highest level reported from the rare-earth doped MOSLED prepared by ion implantation. Recently the EL efficiency was strongly increased by neighboring co-doping Al_2O_3 oxide layer beside the rare-earth doping layers.

采用溶胶凝胶法将氮掺杂TiO_2和硼酸铟复合，制备了一种新型复合催化剂（$N-TiO_2/InBO_3$）。XRD, HR-TEM, XPS, UV-vis DRS, PL and time-resolved PL技术表征结果证明，由于异质结和掺杂态的作用，导致了$N-TiO_2/InBO_3$具有较高的紫外光和可见光催化活性。该结果表明掺杂离子和材料的选择，异质结能带的匹配是提高光催化活性的重要因素。该研究对高性能光电功能材料的设计和制备提供了理论依据。

A new type of composite photocatalysts ($N-TiO_2/InBO_3$ heterostructure) were synthesized by coupling nitrogen doped TiO_2 ($N-TiO_2$) with indium borate ($InBO_3$) via a one-step sol-gel method. Characterized by XRD, HR-TEM, XPS, UV-vis DRS, PL and time-resolved PL techniques, it is revealed that $N-TiO_2/InBO_3$ exhibited an excellent photocatalytic performance compared with TiO_2, N-TiO_2 and $InBO_3$ under both visible and UV light irradiation, due to the formation of a heterojunction at interface and introduction of doping states. This means that the selection of materials and doped ions, matching of energy bands at heterojunction are very important factors for fabrication of photocatalysis. The results offer a paradigm for design and fabrication the optoelectronic functional materials, such as solar cells and photocatalysis.

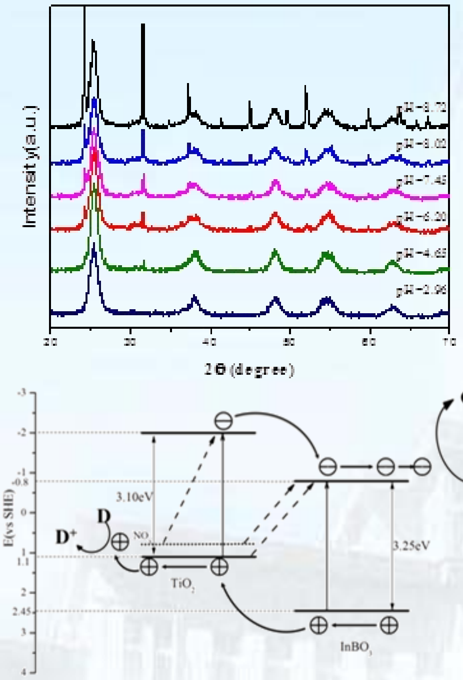

图 15 TiO_2-N-Nx%Ni 的 XRD 谱和能带结构及光催化机理图。

Fig.15 XRD patterns and Schematic diagram for the band structure of N-TiO_2/$InBO_3$ heterostructure and the photocatalytic mechanism.

通过建立TiO_2纳米粒子，纳米管和纳米片的模型，计算了相应的能带结构和态密度；计算结果暗示着三种纳米结构材料的光催化活性为纳米片 >纳米管>纳米粒子。通过实验合成了以上三种纳米结构材料，光催化活性实验验证了理论计算的结果，并进一步研究了TiO_2纳米粒子，纳米管和纳米片的能带结构和光生载流子行为，从而揭示了光催化机理。

The models of nanoparticle, nanotube and nanosheet are designed and their corresponding band structure and density of states (DOS) are calculated theoretically. The calculation results imply the photocatalytic activity of different nanostructure may rank in the order of nanosheet > nanotube > nanoparticle. The desired TiO_2 nanostructures were synthesized and the experiment results confirmed theoretical forecast about the band structure and photocatalytic activity. The detailed band structure and the behaviors of photogenerated charge carriers as well as the photocatalytic mechanism for TiO_2 nanoparticles, nanotubes and nanosheets are studied and analyzed.

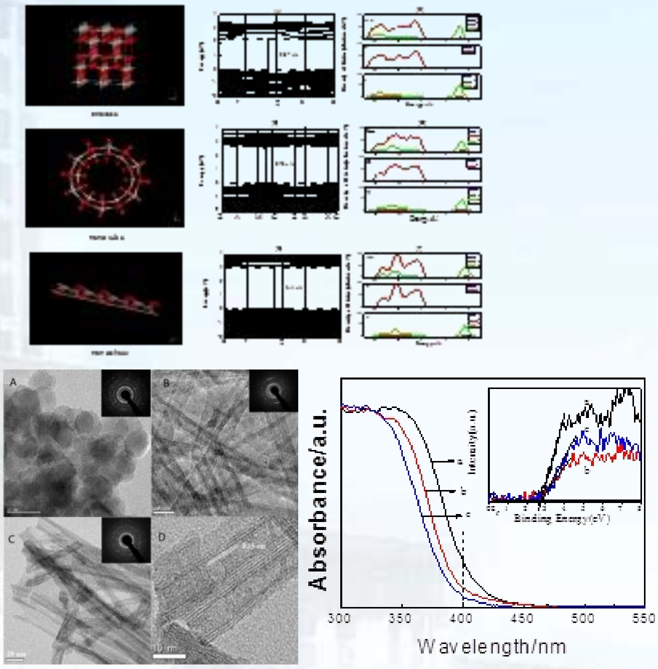

图 16 TiO_2 纳米粒子、TiO_2 纳米管和 TiO_2 纳米片的能带结构和态密度、TEM 和吸收光谱。

Fig.16 Band structure and density of states, TEM image and UV-visible spectra for TiO_2, TiO_2 nanotube and TiO_2 nanosheet.

根据理论计算结果，预测到氮掺杂的ZrO_2其禁带宽度减小，而且氮掺杂ZrO_2与TiO_2之间能够产生电子跃迁。由此采用溶胶凝胶法制备了TiO_2-N/$ZrO_{2-x}N_x$复合催化剂，结果表明氮以取代式掺杂进入ZrO_2晶格，而且相应的禁带宽度有效减小。由于掺杂态的引入和电子界面跃迁，使TiO_2-N/$ZrO_{2-x}N_x$复合催化剂表现出了极强的催化活性。研究结果对于研制高性能的光电功能材料提供重

要的依据。

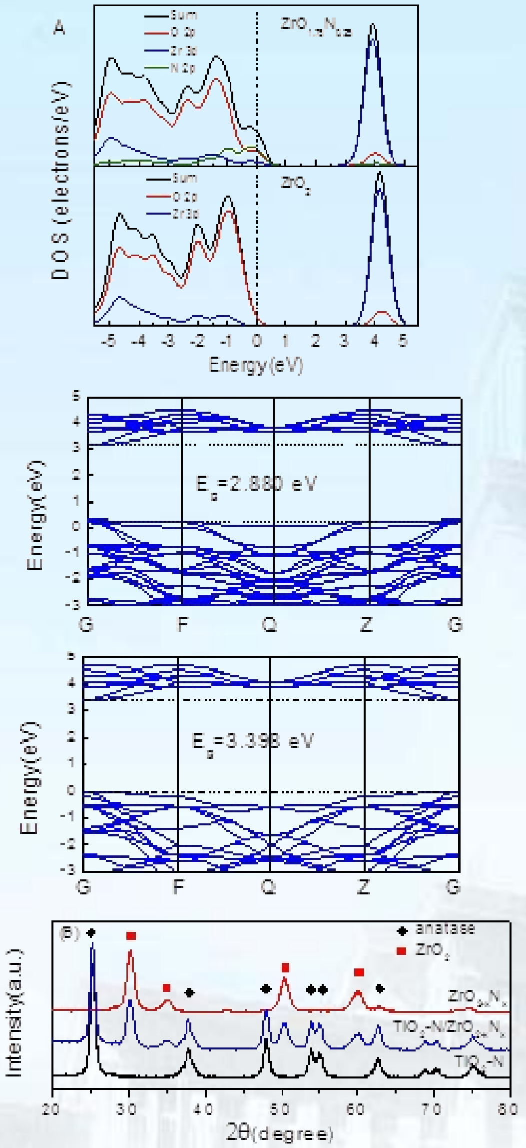

图 17 ZrO_2 and $ZrO_{2-x}N_x$ 的能带结构和态密度(A)，TiO_2-N, TiO_2-N/$ZrO_{2-x}N_x$ and $ZrO_{2-x}N_x$ 的 XRD 谱(B)。

Fig.17 Band structure plots and density of states for the ZrO_2 and $ZrO_{2-x}N_x$ (A), and XRD patterns of TiO_2-N, TiO_2-N/$ZrO_{2-x}N_x$ and $ZrO_{2-x}N_x$(B).

We theoretically predicted the narrowness of band gap for the nitrogen doped ZrO_2 and a possible transition at interface between TiO_2 and ZrO_2. According to the theoretical calculation, TiO_2-N/$ZrO_{2-x}N_x$ composite photocatalyst was prepared by sol-gel method. It was revealed that the nitrogen ions were doped into ZrO_2 lattice in substitutional mode and the corresponding band gap was narrowed effectively. The TiO_2-N/$ZrO_{2-x}N_x$ composite photocatalyst exhibited an excellent photocatalytic performance, due to the electrons' transition at interface as well as the introduction of doping states. The results may offer a paradigm for develop the advanced optoelectronic functional materials which may be used in many fields, such as solar cell, photocatalysis and photosynthesis.

采用溶胶凝胶法，用N和Zr对TiO_2进行修饰，制备出TiO_2-N-X%Zr催化剂。结果表明N以表面物种（NOx）的形式存在于价带上方（高于0.3eV），Zr以取代式掺杂方式进入TiO_2晶格，同时多余的Zr形成了$ZrTiO_4$存在于TiO_2表面。电子可以从NOx物种的能级和$ZrTiO_4$的价带激发到TiO_2的导带，产生强的可见光吸收，而且NOx的存在能够促进光生载流子的分离，导致N,Zr掺杂TiO_2的光催化活性是N掺杂TiO_2的四倍。

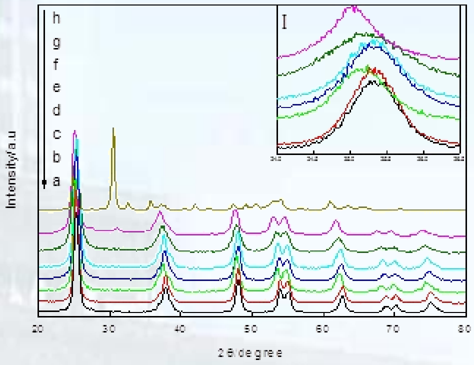

图 18 TiO_2, TiO_2-N, TiO_2-10%Zr and TiO_2-N-X%Zr 样品的 XRD 谱。

Fig.18 XRD patterns of TiO_2, TiO_2-N, TiO_2-10%Zr and TiO_2-N-X%Zr.

In this work, we modified TiO_2 with nitrogen and zirconium by a simple sol-gel method. Our findings suggest that, nitrogen is present as surface species (NO_x) whose energy levels locate at 0.3eV above the valence band. Zirconium is incorporated into the TiO_2 crystal lattice in substitutional mode and surplus zirconium formed $ZrTiO_4$ surface species on TiO_2. There for, the electronic excitations from energy level of NO_x species to the conduction band of TiO_2 and from valance band of $ZrTiO_4$ to the conduction band of TiO_2 lead to significant absorption in the visible-light region. Moreover, the surface nitrogen specials together with the substitutional Zr^{4+} irons lead to an efficient separation of charge carriers. Accordingly, the photocatalytic activity of nitrogen and zirconium co-doped TiO_2 can be enhanced up to about four times of TiO_2-N.

我们发明了一种绿光直写铁电畴翻转技术。按照目前的文献结果，用可见光做光诱导铁电畴翻转时需要同时外加电场。我们设计了一种两步光诱导铁电畴翻转技术，如图3所示，第一步在外加电场的情况下用532 nm激光均匀辐照晶体，第二步，撤去外加电场，用另外一束532 nm的激光可以在晶体上直接写入畴结构。分析认为，第一步外加电场光辐照在晶体中形成了空间电荷场，该电荷场随着外加电场的强度增加而增大。基于该实验现象，我们建立了铁电畴翻转的载流子漂移模型。

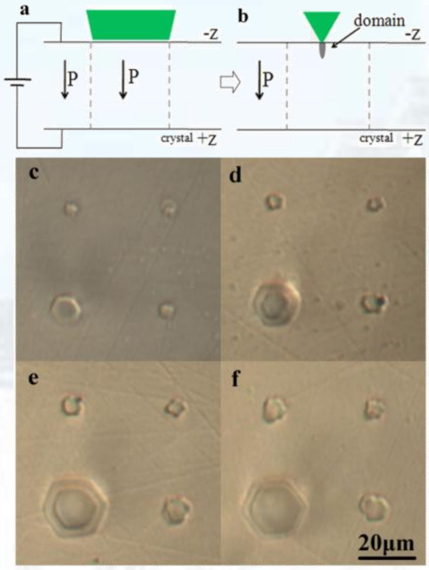

图 19 (a)光致铁电畴翻转两步直写法第一步实验示意图；(b)第二步示意图。(c)-(f)第二步完成后晶片在氢氟酸中腐蚀 10 分钟后的显微镜照片，分别对应第一步外加 1, 2, 3, 4 kV/mm 的电压。这些铁电畴被从左到右、从上到下逐个写入。

Fig.19 (a) Schematic images of the first step of two-step method. (b) Schematic images of the second step of two-step method. (c)-(f) Etching results of domain size in HF acid in 10 minutes in the second step after applying external electric fields of 1, 2, 3, and 4 kV/mm, respectively in the first step. Those domains were written one by one from left to right and from bottom to top.

So far, visible light-induced domain reversal in $LiNbO_3$ has only been observed to occur under assistance of an external electric field. Here a two-step technique named as directly green-light-induced domain reversal was achieved for the first time. In the first step, an external electric field as well as the green laser of 532 nm wavelength is applied on the $LiNbO_3$ crystal. In the second step, direct writing of domain structures in $LiNbO_3$ is realized by another 532 nm laser without assistance of external electric field. Green-light-induced domain reversal results from a light-induced space-charge field generated by the prior application on an external electric field in the first step. Due to the unique two-step method, our further experiments show that light-induced space-charge field in light-induced domain reversal enhances with increasing the applied external electric field. Therefore, a carrier-drift model about this phenomenon was proposed.

弱光非线性及量子相干光学/ Weak Light Nonlinear Optics and Quantum Coherent Optics

负责人：许京军

本方向主要围绕纳微结构的制备与表征、金属等离激元与超材料的光学性质、耦合波导阵列中的光传输、飞秒超快探测技术以及生物光子学等方面开展研究，2014 年度本方向共发表论文 35 篇，出版中英文专著章节各 1 章，申报国家发明专利 3 个。主要取得如下进展：

Our research topics are focused on the fabrication of nano/micro-structures, optical properties of metal plasmonics and metamaterials, light propagation in coupled waveguide arrays, development of detection technology using fs laser pulses, and biophotonics. We published 35 peer-reviewed journal papers, 2 book chapters (Chinese and English version, each), and applied for 3 patents in 2014. The main research progresses in 2014 are as follows.

(1) 纳微结构的制备与表征

Fabrication and characterization of nano/micro-structures

我们展示了用一个飞秒激光脉冲（800nm，120 fs，线性偏振）在纳米颗粒覆盖的硅表面产生和擦除飞秒激光致周期表面结构，这个过程取决于脉冲通量。我们提出这个过程是由于周期表面织构化和表面熔化相关的表面平滑化的竞争引起的。其中，表面织构化是由于入射光和表面等离激元的干涉引起的。我们用双温和德鲁德模型模拟了相应过程，实验结果和理论预期符合得很好。

We experimentally show that the generation and erasure of femtosecond laser-induced periodic surface structures on nanoparticle-covered silicon induced by irradiation with a single laser pulse (800 nm, 120 fs, linear polarization) depend on the pulse fluence. We propose that this is due to competition between periodic surface structuring originating from the interference of incident light with surface plasmon polaritons and surface smoothing associated with surface melting. Experimental results are supported by theoretical analysis of transient surface modifications based on combining the two-temperature model and the Drude model.

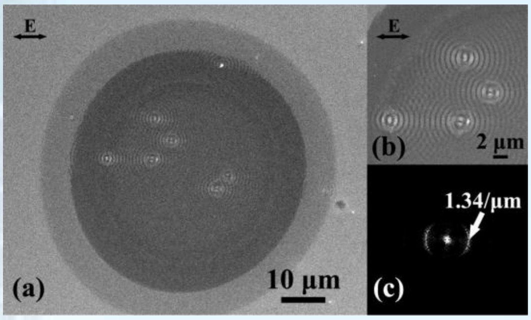

图1. 低能量下，一个飞秒激光脉冲在硅表面引起的周期结构。

Fig1. (a) SEM image of the nanoparticle-covered silicon surface irradiated (in vacuum) by a single femtosecond laser pulse where laser fluence F=1.6 J/cm^2. (b) Details of fs-LIPSS formed on the sample surface. (c) 2D-FFT spectrum of (b). The arrows represent laser polarization direction..

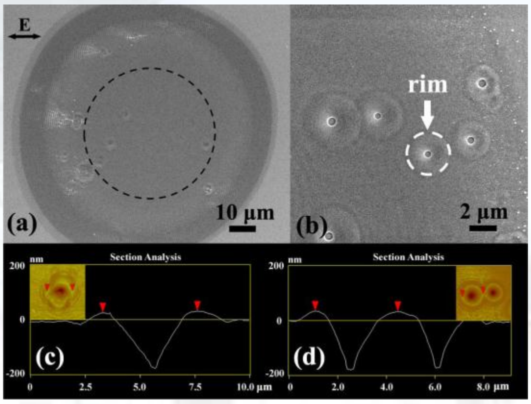

图2. 高能量下，一个飞秒脉冲形成的微纳结构。

Fig2. (a) SEM image of the nanoparticle-covered silicon surface irradiated (in vacuum) by a single femtosecond laser pulse where laser fluence F = 6.7 J/cm^2. Inside the dashed circle, only some bubble-like pits are formed; out of the dashed circle, fs-LIPSS appear. (b) Bubble-like pits with similar size are observed in the central region of a damage spot irradiated by a single pulse with F = 6.0 J/cm^2. (c) and (d) are the AFM images of the craters corresponding to (a) and (b), respectively. The arrows represent laser polarization direction..

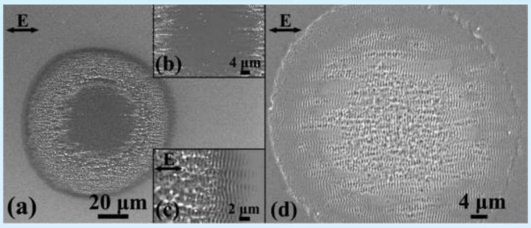

图3. 五个飞秒脉冲在低能量和高能量下形成的微纳结构。

Fig3. SEM image of the nanoparticle-covered silicon surface irradiated by five pulses (in vacuum). (a) Damage spot with F = 6.7 J/cm^2. (b) and (c) Central region and periphery of (a). (d) Damage spot with F = 1.6 J/cm^2. The arrows represent laser polarization direction.

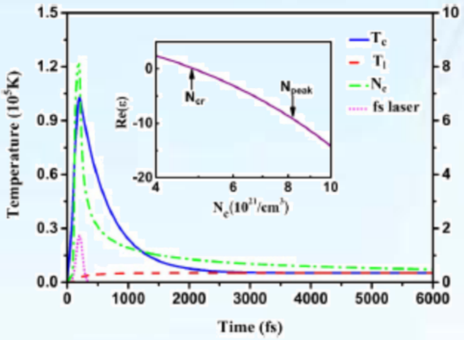

图4. 基于双温-德鲁德模型计算的载流子浓度、温度和晶格温度的变化情况。

Fig4. Evolution of carrier density Nc (green dash dot curve), carrier temperature Tc (blue solid curve), and lattice temperature Tl (red dash curve) calculated for laser fluence F = 1.6 J/cm^2. The purple dot curve shows the laser pulse whose duration is 120 fs. The insert shows a relationship between Nc and the real part of dielectric constant Re(ε), where Ncr is critical carrier density and Npeak is the peak value of the Nc.

我们用两步法制备了自定向液晶-聚合物薄片器件，并研究了其电光调控性能。本方法首先利用基于双光子聚合的激光直写技术在 SU-8 上制备周期结构，再在此结构中填充液晶。由此基本结构加上 ITO 基片直接做成可以用于电光调制的器件。实验表明该电光开关的外加电场在 0.5 V/µm 量级，开关时间在毫秒量级。由于此种制备方法不同于传统的相分离技术制备；液晶通过周期结构的精细结构直接定向，省去了定向膜；选取的 SU-8 材料的折射率与液晶的非寻常光折射率相似。此器件在零电压状态对光的偏振敏感，衍射特性与电压的关系与“经典”方式制备的器件不同，可有望应用于一些特殊的情况。

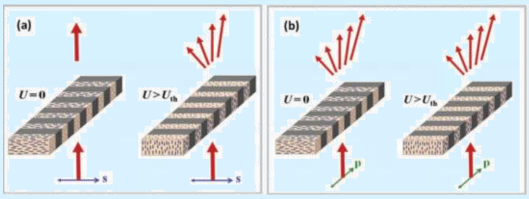

图5. 两步法制备的POLICRYPS光栅电光调控光学衍射示意图。(a) s偏振光在偏压作用下衍射从弱变强；(b) p偏振光在偏压作用下衍射效率基本不变。

Fig5. Schematic drawing of the operation principle of POLICRYPS gratings fabricated by a two-step process. Rods indicate orientation of the nematic director in the channels between the polymer slices. (a) A voltage-induced transition from weak to strong diffraction regime takes places for an s-polarised beam (extraordinary polarisation). (b) Diffraction properties for a p-polarised beam are practically independent of the applied voltage.

We describe optical diffraction properties of polymer liquid-crystal polymer slices (POLICRYPS) assembled through a two-step procedure. At first, a scaffold of periodic polymer slices is fabricated by a direct laser writing method based on two-photon polymerisation. Then the channels between the slices are filled with liquid crystal, and the assembly is incorporated between two ITO-coated glass plates. In contrast to the ‘classical’ POLICRYPS that are fabricated on the basis of a phase separation process and that exhibit spontaneous liquid crystal alignment in the direction perpendicular to the polymer slices (homeotropic alignment), the structures fabricated by the two-step method exhibit spontaneous liquid crystal alignment in a direction parallel to the polymer slices (planar alignment). Consequently, their optical diffraction properties as a function of the polarisation direction of the optical radiation exhibit orthogonal behaviour with respect to the classical structures. The threshold external field for electro-optic switching is in the range of 0.5 V/µm. The associated electro-optic switching times are in the range of milliseconds.

透过率渐变的灰度掩模被广泛用来制作三维微光学元件（MOEs）和微电子机械系统（MEMS）。目前，灰度掩模主要有 COG（Chromium On Glass）灰度掩模和 HEBS (high energy beam sensitive)玻璃灰度掩模，但它们复杂的制作过程和高昂的制作费用限制了其在工业上的应用。激光直写 MTMO 灰度掩模是指激光氧化一些具有透明氧化物的金属薄膜来制作灰度掩模，激光功率可以调节氧化程度和灰度值。MTMO 灰度掩模具有高分辨，简单便宜的制作过程和良好的光热稳定性等优点，近年来受到人们的关注。由于用于制作 MTMO 掩模的激光光斑大小和脉冲时间都在微纳量级上，几十纳米的金属薄膜的氧化过程很难被测量，数值分析金属薄膜的温度场和吸收功率密度可以帮助我们理解金属薄膜氧化过程和灰度掩模的加工原理。

我们首先建立了激光直写基于玻璃基底的 In 薄膜的模型。基于 Airy 求和法（Airy summation）计算了模型的光学性质，如反射率、金属薄膜的吸收系数等。利用时域有限差分法（FDTD）模拟了样品的温度场分布。基于 Mott-Cabrera 氧化理论的分析，推定高功率下的熔化金属薄膜的氧化区域与其吸收功率密度 Q 相关，并存在一个判断氧化的吸收功率密度阈值 Q_{th}。通过分析激光功率为 10 mW 时的加工分辨率，推断 Q_{th} 为 2.17×10^{17} W/m^3，从而计算出激光功率在 6.0 – 8.0 mW 时，MTMO 灰度掩模的平均氧化区域大小为 302 nm，与实验中测量的 300 nm 相一致，从而验证了利用 Mott-Cabrera 理论进行分析激光直写 MTMO 灰度掩模加工原理的正确性。

Metal-transparent-metallic-oxide (MTMO) grayscale photomasks fabricated by direct laser writing have been proposed in recent years. The fabrication mechanism is attributed to light-induced melt oxidization. The temporal-spatial distribution of temperature fields of indium film-glass samples under a laser pulse have been calculated by the Finite-Difference Time-Domain method. The laser action area of the indium film is studied based on the oxidation theories and the absorbed laser power density distribution in molten indium films. The calculated average sub-wavelength fabrication diameter of 302 nm is consistent with the experimental fabrication size under a laser power of 6.0 - 8.0 mW.

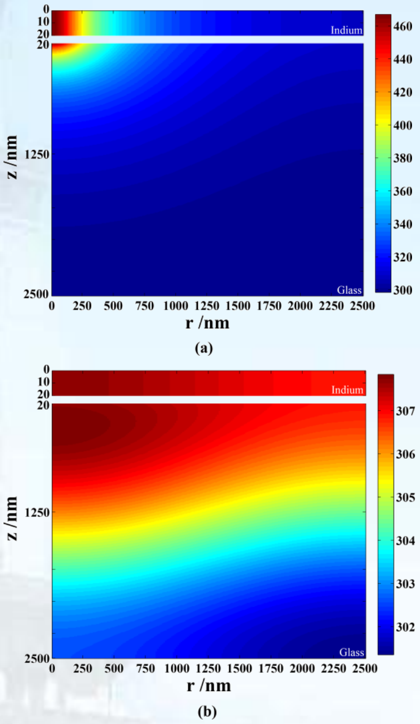

图6. (a) 样品经5.0 mW 1μs激光脉冲加热后的温场分布 (b)加热后的样品经过1μs冷却后的温场分布。

Fig6. Temperature fields of the sample after (a) 1 μs the heating time and (b) after another 1 μs self-cooling time with a laser power of 5.0 mW. For visibility, the indium film (upper pictures) and the substrate (lower pictures) are drawn separately with different scales at *z* direction.

通过改进楔形玻璃光学微腔的加工工艺，采用两次 HF 和两次 XeF_2 刻蚀，我们成功地在硅基芯片上制备了回音廊模式反楔形玻璃光学微腔（Inverted Wedge Resonator，如图 7（a-c）所示）。直径为 150 微米、厚度为 2 微米的微腔的品质因子可以达到 10^6。该微腔制备过程中未采用 CO_2 激光烧蚀技术或者热处理技术，因此，可以实现微腔尺寸的精确控制。通过控制 HF 刻蚀的时间，我们可以制备如图 7（a）和（b）所示的具

有几十纳米厚度边缘的反楔形玻璃微腔。如图 7（f）所示，厚度为几十纳米的边缘没有光场分布，因而即使锥形光纤贴在其表面也不会与微腔的模式发生耦合作用。利用反楔形微腔很薄的边缘作为锥形光纤的支撑，固定锥形光纤和微腔之间的相对位置，可以实现稳定的光耦合，相关的结果如图36所示。反楔形玻璃微腔的这一性质，有利于其在实验室外存在扰动的环境中应用。此外，反楔形玻璃微腔的上表面平整，并且在加工过程中一直受到良好保护，可以在该表面预制或者后期制备光学微结构，实现其它的功能。

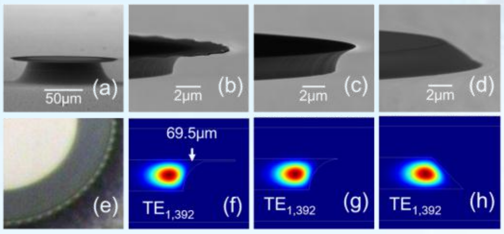

图7. 反楔形（a-c）和楔形（d）玻璃光学微腔的显微镜照片及其典型模式的光场分布。

Fig7. SEM and optical micrographs and typical light intensity distribution of the inverted-wedge resonators (a-c, e-g) and the wedge resonators (d, h).

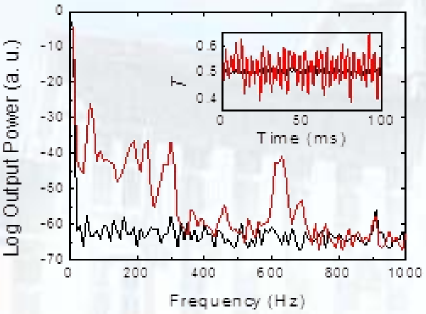

图8. 反楔形光学微腔与锥形光纤耦合稳定性的实验数据。黑色曲线为光纤与微腔边缘接触时的结果，红色曲线为未接触的情况。可见在光纤与微腔边缘接触时，系统的稳定性大大提高。

Fig8. Output spectra indicating the mechanical stability of the taper–resonator system. The inset shows the measured normalized transmission as a function of time. Black and red curves are the results when the taper is in contact and out of contact with the top surface of the inverted-wedge-shaped resonator, respectively.

Silica microresonators with an inverted-wedge shape as shown in Figs. 7 (a-c) were fabricated using conventional semiconductor fabrication methods. Controllable coupling from undercoupling to the overcoupling regime through the critical coupling point was demonstrated by horizontally moving a fiber taper while in touch with the top surface of the resonator. The measured quality factors of the resonators with 150-μm diameter and 2-μm thickness were greater than 10^6 in 1550-nm band. By controlling the second round HF etching time, we can fabricate inverted-wedge resonator with a thin outer ring as shown in Figs. 7 (a,b). As shown in Fig. 7 (f), there is no high-Q mode supported in the thin outer ring. The thin outer ring of the resonator provided a support for the fiber taper leading to robust stable coupling (see Fig. 8). Therefore, these resonators can be used without worrying about perturbations that can affect the coupling conditions for in-field applications outside the laboratory setting. Additionally, the silica surface is well-protected during the fabrication process, and microstructures could be created on top of the silica wafer in advance.

超细晶铟薄膜在光电产业、微电子行业、灰度掩模等领域有着广泛的应用。无疑晶粒大小对薄膜的物理性能有很重要的影响。为了研究晶粒大小对薄膜光电性能的影响，我们制备了铟、氧化铟、氧化铟锡超细晶薄膜样品，并研究了晶粒尺寸与光密度、方块电阻的关系。这些样品通过多层沉积，每层都表面氧化的方式获得。实验结果表明，超细晶铟薄膜在 350 到 700nm 有较高的 OD 值，而氧化铟薄膜在可见紫外区有一个较低的 OD 值。当晶粒变小，氧化铟和氧化铟锡薄膜的导电性变好。这些结果表明，薄膜的晶粒尺寸对其光电性能有密切的关系，这种特性可以应用到灰度掩膜和透明导电播磨的加工制造领域。此外，我们还研究了铟薄膜的成分组成、化学价态以及超细晶薄膜的形成机理。

Indium nanofilms composed of ultrafine grains have many applications in photovoltaic technology, microelectronics industry, grayscale lithography and so on. It is unquestionable that ultrafine grains have an important influence on physical properties of the films. For investigating the role of grain size in optical and electric properties of the films, we took In as an example to deeply study the relationship between grain sizes and the optical density (OD) spectra as well as the square resistance in the In, In_2O_3 and ITO nanofilms with ultrafine grains, which were prepared by multiple-oxidation fabrication technique for stopping nucleation-growth. The experimental results show that In films with ultrafine grains have a high OD value in the range from 350 to 700 nm, In_2O_3 films, nevertheless, have a smaller OD in the visible and NUV region; while the grain size can greatly improve the conductivity of In_2O_3 and ITO film but has less effect on that of the indium films. These results demonstrate that the grain size of the film is closely related to its optical and electric properties, and indicate ultrafine-grained In nanofilm, meanwhile, can be used in fabrication of grayscale masks and transparent conductive films due to its good optical and electric properties. Moreover, the morphology as well as composition and chemical bonding states of In nanofilms are analyzed, and the controllability of ultrafine grains is deeply investigated theoretically.

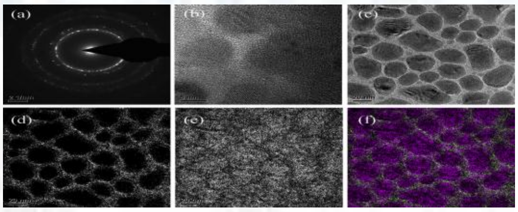

图9. 沉积4次的20nm厚铟膜的 (a) SAED图像；(b) HRTEM图像。沉积1次的20nm厚铟膜的EELS图像：(c) 零损失谱；(d) 氧分布；(e)铟分布；(f)铟（红）和氧（白）分布。

Fig8. In film (20 nm) deposited for four times. (a) SAED pattern (b) HRTEM image; EELS maps of the indium film (20 nm) deposited for one time: (c) the zero loss map (d) oxygen map (e) indium map (f) the indium and oxygen map (red is indium while white is oxygen)

由于拉曼光谱能够很好地反映样品的物理信息，所以关于物质拉曼特性的研究就显得尤为重要。我们通过磁控溅射和溅射间隙氧化的方式制得了 In/InOx 核壳结构，并在 In/InOx 核壳结构中发现一个围绕 558cm^{-1} 的异常峰，这个峰的峰位不随温度变化。通过 TEM、XRD 进行成分分析，发现这个结构中存在 In 晶体和 InOx 的不完全氧化物，我们推断这个峰可能来自壳层中铟的不完全氧化物。

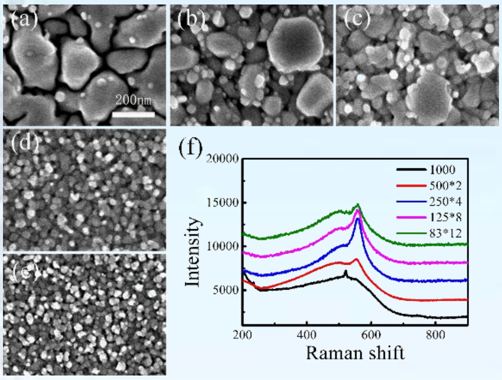

图10. 相同总的沉积时间不同沉积次数In/InO$_x$核壳结构的SEM图像和拉曼谱(a)1次沉积1000s； (b)2次沉积； (c) 4次沉积； (d)8次沉积； (e) 12次沉积； (f)拉曼光谱。

Fig10. SEM images, Raman spectra of In/InO$_x$ core–shell structured nanoparticles deposited for different times, showing films deposited (a) one time (1000 s), (b) twice (500 s×2), (c) four times (250 s×4), (d) eight times (125 s×8), (e) twelve times (83 s×12) respectively, (oxygen was introduced into the deposition chamber during all the sputtering intervals), and (f) Raman spectra.

The properties of Raman phonons are very important due to the fact that they can availably reflect some important physical information. An abnormal Raman peak is observed at about 558 cm^{-1} in In film composed of In/InO$_x$ core–shell structured nanoparticles, and the phonon mode stays very stable when the temperature changes. Our results indicate that this Raman scattering is attributed to the existence of incomplete indium oxide in the oxide shell.

(2) 金属等离激元与超材料的光学性质
Optical properties of metal plasmonics and metamaterials

不同于三维手性结构，当从不同的方向观察二维平面手性结构时，其手性对称性将发生（左右）反转。这一特殊性质产生了入射光波的非对称透射效应，即同手性圆偏振光自相反方向入射二维手性结构时具有不同的透射率（见图11a）。该效应来源于手性结构对于左、右旋圆偏振光间互相转换效率的差异。自从2006年首次从实验上观察到超材料中的非对称透射效应以来，该效应得到了人们广泛地研究与关注，并提出多种等离子超材料结构设计。之前多数工作主要集中于效应强度的提高，而带宽较小。而在实际应用中，往往还需要较宽的响应带宽。我们使用数值计算的方法提出了一种在可见-近红外波段具有较宽非对称透射带宽的二维平面螺旋超材料（见图11b）。我们发现只需简单地通过增加螺旋结构的螺旋匝数，便可以将非对称透射带宽从单匝结构的60nm展宽至940nm覆盖了近红外波段的965nm至1905nm（见图11c）。我们这一工作为可见-近红外宽带非对称手性超材料的实现与加工提供了理论指导与依据。

It was understood that a 2D planar chiral structure reverses its handedness when observed from opposite side. This results in a novel phenomenon that does not happen in conventional 3D chiral systems called asymmetric transmission (AT), which manifests itself as a difference in the total transmission of a circularly polarized wave between forward and backward propagations (Fig.11a). Such effect arises from differences of left-to-right and right-to-left circular polarization conversion efficiencies of the structure. Since its first experimental demonstration in 2006, AT effects have been studied from various metamaterial structures. Recent efforts have been devoted to increase the magnitude of the effect. On the other hand, real applications of AT effects may demand broad spectral response. Despite some works have been done to broaden the spectral range of AT effect in microwave. We numerically demonstrate a method to achieve broadband AT in the visible to near-infrared (NIR) part of the spectrum on the basis of a 2D planar spiral metamaterial design (Fig.11b). We found that by increasing the number of turns of the spiral meta-atom, the bandwidth of the AT effect is broadened dramatically from 60 nm for 1-turn structure to more than 940 nm ranging from 965 nm to 1905 nm is realized for multi-turn structure (Fig.11c).

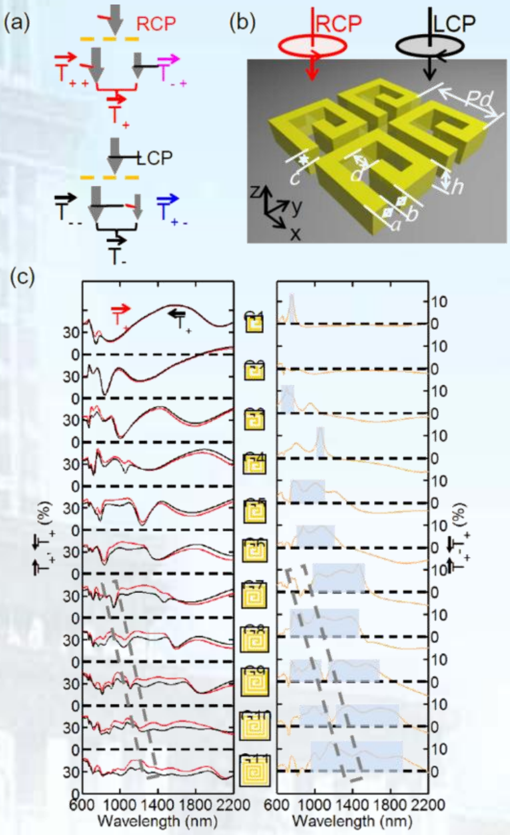

图11.（a）非对称透射以及圆偏振转换。（b）螺旋结构超材料。（c）超材料透射光谱随着外界折射率的变化。（d，e）超材料的波长与光强模式传感性能。

Fig11. (a) Illustration of transmission and polarization conversion of circularly polarized light. Incident circularly polarized light partially directly transmit remaining the same handedness and partially convert to the opposite handed component. (b)Design of the gold G-shaped chiral metamaterial suspended in air. (c)The total transmission and transmission asymmetry for RCP light with increasing number of circles in one unit cell. Grey (Red online) and black (black online) curves correspond, respectively, to propagating directions along -z and +z.

常规的全光开关有开关阈值高，尺寸大不易集成等缺点。我们提出了一种新型的全光双稳开关，这种开关由常规的电介质平板波导和含有克尔介质的布拉格谐振腔组成，布拉格谐振腔位于纳米尺度的金属-电介质-金属表面等离子体波导中。在电磁场从电介质平板波导到纳米尺度的表面等离子体波导的耦合过程中，由于空间尺度的压缩效应，电场强度可以得到极大的增强，而这种电场增强又可以用来降低全光开关的功率。此外，我们还提出了一种基于阻抗的半解析传输矩阵方法来计算设计这种开关，开关的反射、透射以及双稳回路都可以通过这种方法快速准确的计算。为了验证我们的传输矩阵算法，我们使用了有限时域差分法（FDTD）来计算开关的反射、透射和双稳回路，FDTD的计算结果和传输矩阵算法得到的结果符合得非常好。

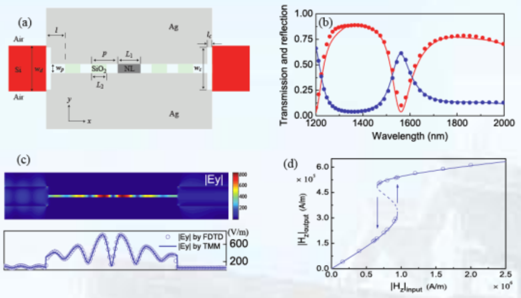

图12. (a) 全光双稳开关基本结构。(b) 传输矩阵法（实线）与有限时域差分法（点）计算得到的反射谱线（红）与透射谱线（蓝）对比。(c) （上）透射率峰值时电场在双稳开关内的分布情况。（下）有限时域差分法与传输矩阵法求得的电场分布对比。(d)传输矩阵法（线）与有限时域差分法（点）求得的双稳开关的双稳回路对比。

Fig12. (a) Sketch of the optically bistable device. (b) Transmission (initially decreasing curve, blue) and reflection (initially increasing, red) calculated using the FDTD (dots) and the TMM (full lines). (c) Distribution of $|E_y|$ calculated using the FDTD at 1550 nm and Comparison between $|E_y|$ calculated by the TMM and FDTD along x. (d) Bistability loops calculated by the FDTD (blue open circles) and E=0:862Ey (blue line) for L1=240 nm.

Traditional all-optical devices have two main drawbacks: large scale and relatively high operational light intensity, which prevent practical applications. We present a bistable device consisting of a Bragg grating resonator with a Kerr medium sandwiched between two dielectric slab waveguides. The resonator is situated in a nanometer-scaled metal–insulator–metal plasmonic waveguide. Due to the dimensional confinement from the dielectric waveguide to the nanoscaled plasmonic waveguide, electric fields are enhanced greatly, which will further reduce the threshold value. Moreover, a semi-analytic method, based on the impedance theory and the transfer matrix method, is developed to study the transmission and reflection spectra as well as the bistability loop of such a switch. Our method is fast and accurate, as confirmed by the finite-difference time-domain simulation.

我们通过在纳米尺寸下的金属-电介质-金属波导下面引入布拉格光栅，提出一种在纳米尺度下的新型塔姆态，并将这种态命名为表面等离子体塔姆态。由于这种塔姆态的作用，可以实现电磁场的双重增益：第一次增益源自电磁场耦合到纳米波导时的空间尺度压缩效应；第二次增益源自布拉格光栅末端与金属界面处的塔姆效应。以我们的二维耦合结构为例，该结构可以对1550 nm波长的电场强度实现1050倍的放大。整个结构参数由基于阻抗的传输矩阵算法进行优化设计，并由有限元算法验证。

We propose a novel type of nano-scaled Tamm states for light enhancement by introducing a Bragg reflector (BR) in a nanoscaled metal-insulator-metal (MIM) waveguide, which we call plasmonic Tamm states (PTSs). Due to PTS effects, fields can be enhanced for a second time at the terminal side of the MIM BR on the basis of the dimension confinement. The enhancement of $|E|^2$ is up to 1050-fold for light of 1550 nm, as shown in our 2D focusing configuration. Structural design and optimizations are performed by an impedance-based transfer matrix method and are further confirmed by a finite element method.

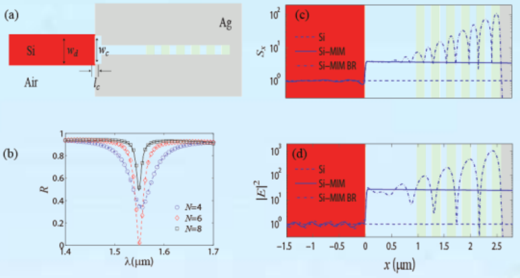

图13. (a) 表面等离子体塔姆态结构示意图。（b）入射光场反射率随布拉格光栅周期数变换结果，点为有限元算法计算得到的结果，线为传输矩阵法计算结果。(c) 波印亭矢量在硅波导，硅-金属-电介质-金属波导以及硅-金属-电介质-金属布拉格谐振腔结构中的分布情况，波印亭矢量的最大增益倍数为110倍。(d) 电场强度在三种结构中的分布情况，其最大增益倍数为1050倍。

Fig13. (a) 2D coupling configuration. (b) Comparison of reflection spectra calculated by TMM [N = 4 (dash–dot line), 6 (dashed line), and 8 (solid line)] and by FEM [N = 4 (open circle), 6 (open diamond), and 8 (open rectangle)]. The reflection reaches a minimum of 1.4% for N =6 at 1550 nm. (c) Distribution of the S_x along the central axis. Maximum enhancement factor is 110. (d) Distribution of $|E|^2$ along the central axis. Maximum enhancement factor is 1050. It should be noted that the Ohmic loss is considered in the simulation, which is not obvious, especially in the logarithmic co-ordinate.

我们提出了一种复合纳米结构，由一个纳米球对和一个纳米方孔复合而成。这种结构可以极大增强局域的光学近场至入射光场的 2100 倍。如果我们将这种复合结构周期性排列，我们可以将共振波峰由 560 nm 转移到 760 nm，并且电场强度比单个复合结构增加了 37%。我们将这些现象归因于光电场的两步限域和复合结构间的耦合效应。单个和周期阵列的纳米复合结构都可以满足单分子探测的要求。

We bring a design of nanostructure composed of a metallic nanosphere pair and a rectangle nanoaperture, which can dramatically enhance the localized optical near-field up to 2100 times larger than the incident optical field. When the composite nanostructures are periodically arranged, the resonance peak can be varied from 560 nm to 760 nm and the electric field enhancement is about 37 percent larger than that of single composite nanostructure. We attribute these phenomena to two-step confinement of the optical electric field and the coupling effect of the composite nanostructures. Both enhancement factors of single and periodic composite nanostructures are sufficient for single molecule detection.

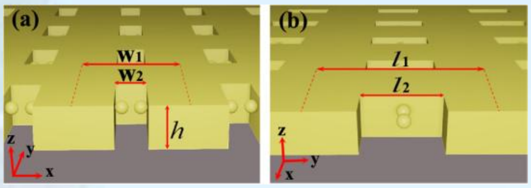

图14. 样品结构示意图。

Fig14. A sketch of periodic NSNAs from different perspectives. The width of the nanoaperture is *w*2, the diameter of nanosphere is 50 nm, the height of nanoaperture is *h*. (a) The front view, *w*1 = 400 nm, *w*2 is tunable, *h* = 160 nm. (b) The side view, *l*1 = 650 nm, *l*2 = 292 nm.

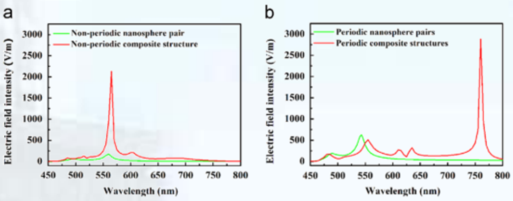

图15. (a) 非周期的纳米球对和复合结构的电场增强对比。(b) 周期这列的纳米球对和复合结构的电场增强对比。

Fig15. (a) Calculated /*E*/ spectra in the center point of the gap for non-periodic nanosphere pair and NSNA. The geometrical parameters of non-periodic NSNA are same as periodic NSNAs, and the diameter of each nanosphere is still 50 nm. (b) Calculated /*E*/ spectra in the center point of the gap for periodic nanosphere pairs and NSNAs.

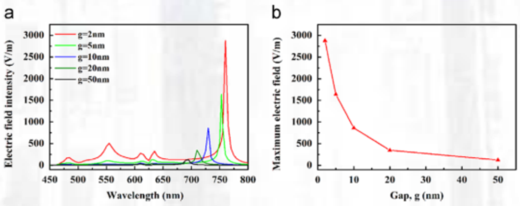

图16. (a) 复合结构缝隙大小对电场增强和共振波长的影响；(b) 最大电场增强随缝隙大小的变化。

Fig16. (a) Calculated /*E*/ spectra in the center point of the gap for periodic NSNAs of different gap size between two nanospheres. (b) Maximum electric field /*E*/ as function of gap *g* for periodic NSNAs.

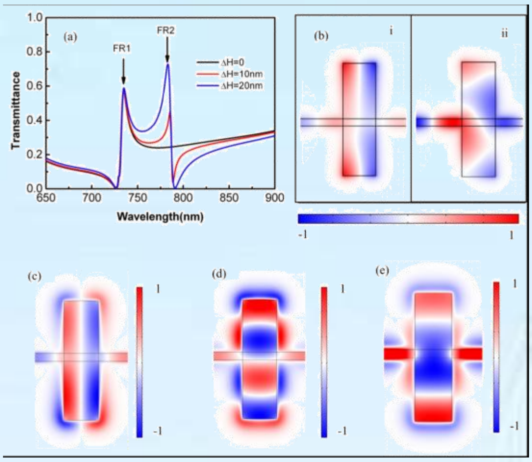

图17. (a)不同参数的等离子共振结构的透射光谱 L = 220 nm, H = 760 nm, D = 50 nm, ΔH = 0 (黑线); ΔH = 10 nm (红线); ΔH = 20 nm (蓝线). (b) FR 1 （735 nm ）(i) 时和 FR 2 （783 nm）(ii) 时 等离子共振结构中归一化的磁场z分量(H)z 的分布图，此时结构参数为： L = 220 nm, H = 760 nm, D = 50 nm, ΔH = 20 nm。 (c)-(e) 分别为等离子共振结构参数为L = 220 nm, H = 760 nm 时的三个本征模式TM1,0 模（735 nm），TM0,3 模 （783 nm），和 TM$_{0,2}$ 模 （1082 nm）的归一化的磁场z分量(H)z 的分布图。

Fig17. (a)The transmission spectra of the plasmonic structure with L = 220 nm, H = 760 nm, D = 50 nm and ΔH = 0 (black line); ΔH = 10 nm (red line); ΔH = 20 nm (blue line). (b)The normalized z-direction magnetic field (H)z in the structure with L = 220 nm, H = 760 nm, D = 50 nm and ΔH = 20 nm: (i) FR 1 at 735 nm, (ii) FR 2 at 783 nm. (c)-(e) The distribution of the normalized z-direction magnetic field (H)z of the eigenmodes TM1,0 mode at 735 nm,TM0,3 mode at 783 nm and TM$_{0,2}$ mode at 1082 nm respectively in the rectangular cavity with L = 220 nm, H = 760 nm.

我们提出了一种由一个 MIM（金属 - 绝缘体 - 金属）波导和一个矩形腔构成的非对称等离子共振结构，这种等离子共振结构可以支持由不同机制引起的双Fano共振。其中一个 Fano 共振源自于矩形空腔的水平谐振模式和垂直谐振模式之间的耦合。另一种 Fano 共振是由等离子共振结构的不对称性引起的。正是因为两个 Fano 共振的物理机制不同，所以每个 Fano 共振都可以通过改变矩形腔的不同参数进行地独立地调控。并且，在调控过程中，两个Fano共振的 FOM（品质因子）几乎保持很大数值不变，两者皆大于 650。这样，我们通过改变矩形腔的参数可以对这种等离子共振结构的透射光谱进行自由地调控，形成各种不同位置、不同半高宽（FWHM）的透射窗口。这种结构在传感器，非线性和慢光器件等领域中将有非常广泛的应用。

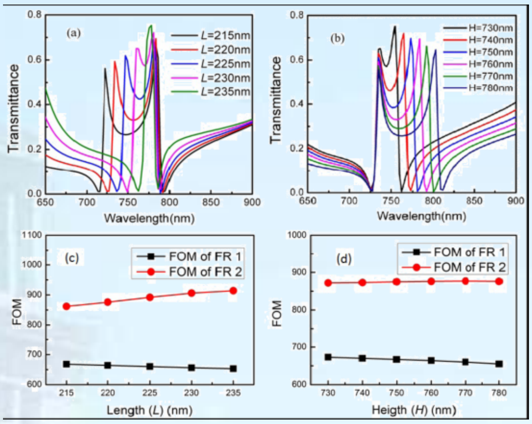

图18. 透射光谱与结构参数之间的关系。(a) H = 760 nm， ΔH = 20 nm， D = 50 nm固定不变，改变L时的光谱变化；（b）L= 760 nm， ΔH = 20 nm， D = 50 nm固定不变，改变H时的光谱变化；（c）和（d）分别为改变结构参数L和H时，FR 1（黑线）和FR 2（红线）的FOM值的变化曲线。

Fig18. The dependence of tansmission on the structure parameters. (a) Different L with fixed H = 760 nm, ΔH = 20 nm and D = 50 nm; (b) different H with fixed L = 760 nm, ΔH = 20 nm and D = 50 nm. (c) and (d) The change curves of FOM of FR 1 (black line) and FR 2 (red line) with the change of the structure parameters, L and H respectively.

We reported an asymmetric plasmonic structure composed of a MIM (metal-insulator-metal) waveguide and a rectangular cavity, which can support double Fano resonances originating from two different mechanisms. One of Fano resonance originates from the interference between a horizontal and a vertical resonance in the rectangular cavity. And the other is induced by the asymmetry of the plasmonic structure. Just because the double Fano resonances originate from two different mechanisms, each Fano resonance can be well tuned independently by changing the parameters of the rectangular cavity. And during the tuning process, the FOMs (figure of merit) of both the Fano resonances can keep unchanged almost with large values, both larger than 650. Such, the transmission spectra of the plasmonic structure can be well modulated to form transmission window with the position and the full width at half maximum (FWHM) can be tuned freely, which is useful for the applications in sensors, nonlinear and slow-light devices.

我们数值模拟研究了一种纳米谐振腔结构的表面等离子共振性质，该结构由两个MIM（金属-绝缘体-金属）波导和一个开口环型腔构成。通过调整环形腔的开口位置，结构中的多级表面等离子共振模式可以被激发、减弱或者截至。这一特殊的现象是由环形腔开口位置处的电场偏振态决定的。当开口处电场的偏振方向垂直于开口位置，奇数模式将会被激发。当开口处电场的偏振方向平行于开口位置，偶数模式将会被激发。此时的谐振腔结构可以看作一个LC振荡回路。随着开口宽度的增大，LC 回路的电容减小，共振波长将会发生蓝移。我们的结果显示此种结构在可调多通道滤波器和生物传感器等纳米集成光子器件中存在广泛的应用前景。

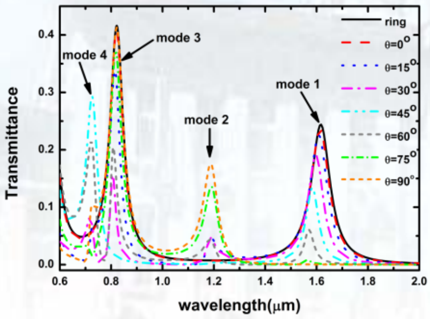

图19. 不同开口角度情况下，开口环形共振器的透射光谱。

Fig19. The transmission spectra of the split-ring resonator with different split angles.

A nanoscale resonator composed of two metal–insulator–metal (MIM) waveguides and a split ring is investigated numerically. The multipolar plasmonic resonance modes can be excited, weakened, or even cut off by adjusting the split angle. These novel phenomena are due to the electric polarization in the split area. Odd modes exhibit when the electric field is polarized perpendicular to the split. The resonator acts as a LC circuit for the electric field polarized parallel to the split, in which even modes are excited. The capacitance diminished when the split depth is increased, and the resonance wavelengths of even modes exhibit blue shift. Our results imply an extensive potential for tunable multichannel filters and biosensor devices in integrated nano-optics.

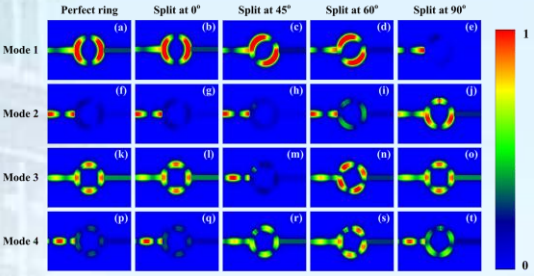

图20. 不同开口角度下的y方向的磁场模分布情况：(a)－(e)M =1，(f)－(j) M =2，(k)－(o) M= 3， (p)－(t) M= 4。

Fig20. The normalized field distributions of │Hy│at different split angels with mode number M: (a)－(e)M =1,(f)－(j) M =2, (k)－(o) M= 3 and (p)－(t) M= 4, respectively.

我们发现了多层金属球壳中的杂化等离子模式翻转效应。等离子杂化理论被广泛的应用于金属纳米结构的等离子反应研究中。我们从纳米颗粒消光谱以及电荷密度分布的角度，研究了金-硅-金多层纳米球壳的等离子杂化图像。我们发现，减小金核心和金外壳的间距，导致高能消光峰从$\left|\omega_{-}^{+}\right\rangle$模式变为$\left|\omega_{+}^{-}\right\rangle$模式。我们认为，这是由于增强的金核心与金外壳之间的等离子相互作用导致了$\left|\omega_{-}^{+}\right\rangle$模式和$\left|\omega_{+}^{-}\right\rangle$模式的能量翻转。我们的研究能够很好的用$\left|\omega_{+}^{-}\right\rangle$模式解释高能消光峰在中间硅层和周围环境折射率不同的情况下有趣的反向移动现象。我们发现的杂化等离子模式的能量翻转效应，对深入理解等离子杂化理论，给出了新的视角。此外，我们的研究提供了一种基于电荷分布分析的方法用来研究金属纳米结构的等离子特性，可以作为等离子杂化理论的必要补充。

We find the effect of hybrid plasmon modes reversion in metal multilayer nanoshells. The plasmon hybridization theory

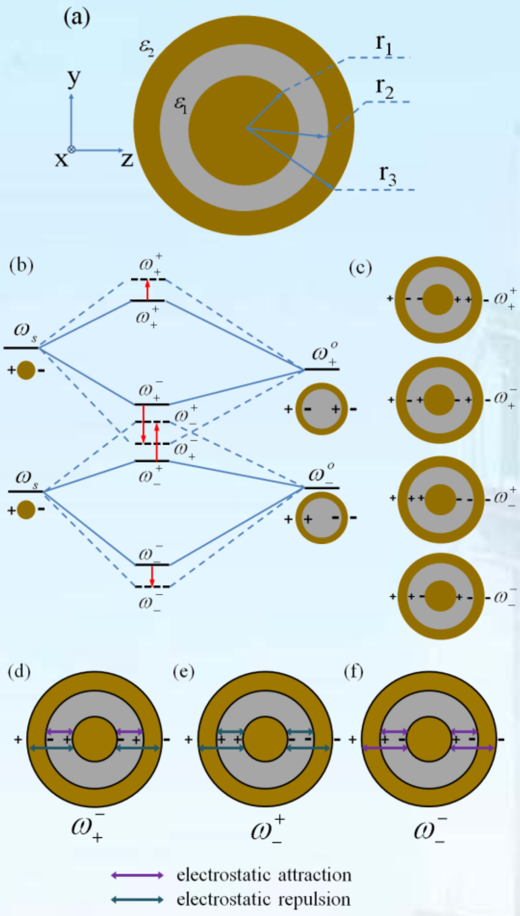

图21. (a) 金-硅-金多层纳米球壳示意图；(b) 金核与金外壳的等离子杂化图像，虚线代表增强的内核与外壳间的相互作用，等离子模式的能量翻转在图中标出； (c) 金-硅-金多层纳米球壳杂化等离子模式电荷分布示意图；(d), (e),和(f) $\left|\omega_+^-\right\rangle$, $\left|\omega_-^+\right\rangle$ and $\left|\omega_-^-\right\rangle$ 模式中电荷相互作用示意图。

Fig21. (a) Mid-sectional view of the Au-silica-Au multilayer nanoshells. (b) Schematic of energy diagram of the inner Au core and outer Au shell, representing plasmon hybridization. The dashed line indicates the coupling modes under enhanced interaction between the Au core and Au shell. (c) Schematic of the charge distribution of the coupling modes in the Au-silica-Au multilayer nanoshells according to the plasmon hybridization. (d), (e) and (f) Schematic of the charge interaction between the Au core and the Au shell in the $\left|\omega_+^-\right\rangle$, $\left|\omega_-^+\right\rangle$ and $\left|\omega_-^-\right\rangle$ plasmon modes of Au-silica-Au multilayer nanoshells.

is widely used to study the plasmon response of metallic nanostructures. We study the plasmon hybridization picture of the Gold-Silica-Gold multilayer nanoshells from the viewpoint of the optical extinction spectrum and the charge density distribution. We find that reducing the distance between the Au core and Au shell causes the conversion from $\left|\omega_-^+\right\rangle$ to $\left|\omega_+^-\right\rangle$ modes of the high energy extinction peak. According to our opinion, it is because the increased plasmon interaction between the Au core and the Au shell induces the energy reversion of the $\left|\omega_-^+\right\rangle$ and $\left|\omega_+^-\right\rangle$ plasmon modes. The interesting contrary shift effect of the high energy extinction peaks with different dielectric constant of the middle silica shell and outer surrounding is well explained by the $\left|\omega_+^-\right\rangle$ modes. The energy reversion of hybrid plasmon modes we reported would give new insight into the plasmon hybridization theory. Moreover, our study could offer a modified way basing on the charge interaction analysis, which is necessary supplement to the plasmon hybridization theory, for studying plasmon responses in optical spectrum of metal nanostructures.

我们研究了双重对称性破缺下的金-硅-金多层纳米球壳的光学特性。利用了离散偶极近似方法和等离子杂化理论，研究了同时包含切壳型和偏心型破缺的金-硅-金多层纳米球壳（DSMNS）的光学特性。我们考察了入射光偏振以及颗粒几何参数对该结构等离子共振特性的影响。在两种对称性破缺的影响下，该结构能够产生多个对偏振敏感的等离子共振峰。改变入射光偏振 90 度，该结构的两个光谱透明窗口，能够进行非常灵活的调节。这种偏振控制的光谱透明在很多方向，如滤波以及彩色显示等，都有重要的应用价值。此外，我们还研究了该结构的折射率敏感性，当环境折射率变化时，该结构发生三个消光峰的同时移动，表明其在生物传感方面的潜在应用价值。

We studied the optical properties of the gold-silica-gold multilayer nanoshells with dual symmetry breaking. In this study, the optical properties induced by dual symmetry breaking including both shell cutting and core offsetting in the gold-silica-gold multilayer nanoshells have been studied by the discrete dipole approximation simulations and the plasmon hybridization theory. The influences of the incident polarization and geometrical parameters on the plasmon resonances of this dual-symmetry-breaking Au-silica-Au multilayer nanoshells (DSMNS) are investigated. Under the combined effect of the two types of symmetry breaking, it is found that the polarization dependent multiple plasmon resonances can be induced in the DSMNS. By changing the polarization of 90^{o}, the switching of the two transparency windows can be flexibly adjusted in the DSMNS with different types of Au core offsetting. This polarization controlled transparency is likely to generate a wide range of photonic applications such as filters and color displays. Furthermore, the local refractive index sensitivity of the DSMNS is also investigated, and the triple extinction peaks simultaneous shift is found as the surrounding medium changed, which suggests the potential applications for biological sensors.

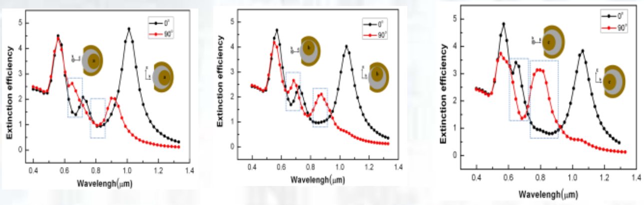

图22. a型, b型, c型DSMNS结构在入射光偏振0度和90度时的消光谱。虚线框表示透明窗口。

Fig22. Extinction efficiency of the ‘a’ type of DSMNS, the ‘b’ type of DSMNS, the ‘c’ type of DSMNS at the rotational angle $\beta = 0^{o}$ (transverse coupling) and $\beta = 90^{o}$ (axial coupling) along y-axis respectively. The dashed boxes indicate the transparency windows.

我们提出了由一个等边三角形和一个C 型环构成的等离子体共振腔，由于对称破缺的存在，我们发现这个共振腔的消光特性对入射光的偏振灵敏度高，从而引起很强的Fano 共振。这个 Fano 共振起源于正三角形和开口环之间的强耦合作用。正三角形的大小和相对取向很好的控制电磁耦合的强度和金属间隙区域的有效电容，从而这些参数能够很好地调控 Fano 共振。通过正三角形和 C 型环微纳结构的不同组合，我们可以用偏振相关的方法主动的调节 Fano 共振谱特性。计算结果表明，体折射率灵敏度超过 800 纳米每折射率单位，并且 FOM 值超过 6.8 在近红外区域。这些特性使我们提出的等离子体微纳腔在 Fano 开关和传感方面具有应用潜力。

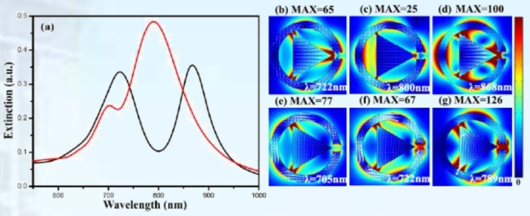

图23. (a) RTSR-I腔的消光光谱，其中正三角形的边长L=180纳米. 黑线和红线分别是偏振沿着x轴和y轴的消光谱。(b)–(g) 在共振波长处的电场增强和电荷密度矢量分布. 最大电场增强标注在每幅图的上面。

Fig23. (a) Extinction spectra of the RTSRI cavity with L=180 nm. The black and red lines are the spectra when the polarization is along the x and y axes, respectively. (b)–(g) The electric field enhancement and current density vector distribution. The maximum field enhancement is indicated above each plot.

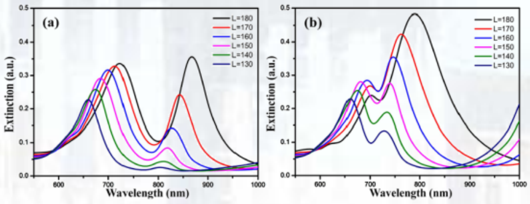

图24. RTSR-I腔的消光光谱随着正三角形的边长L的演化曲线。图（a）和（b）是偏振分别沿着x轴和y轴。

Fig24. Evolution of the extinction spectra of the RTSR-I cavity versus the side length L of the RT for the incident polarization along the (a) x axis and (b) y axis.

The extinction properties of a plasmonic nanocavity consisting of a regular triangle embedded in a split ring (RTSR) plasmonic nanostructure have been investigated. Due to symmetry breaking of the RTSR cavity, we

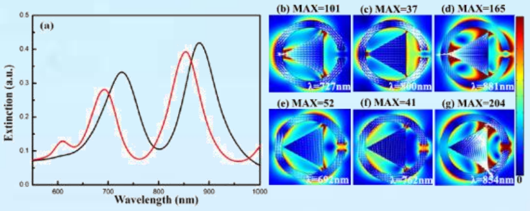

图25. (a) RTSR-II腔的消光光谱，其中正三角形的边长L=180纳米．黑线和红线分别是偏振沿着x轴和y轴的消光谱。(b)–(g) 在共振波长处的电场增强和电荷密度矢量分布．最大电场增强标注在每幅图的上面。

Fig25. Extinction spectra (a) and the electric field enhancement (lEl) and current density vector distribution (b)–(g) of the RTSRII with L=180 nm. The details of the figures are listed in the text.

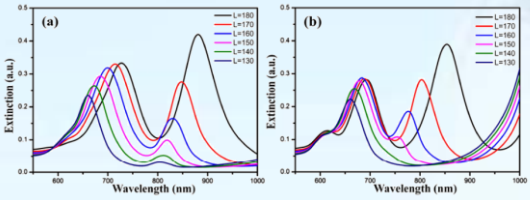

图26. RTSR-II腔的消光光谱随着正三角形的边长L的演化曲线。图（a）和（b）是偏振分别沿着x轴和y轴。

Fig26. Evolution of the extinction spectra of the RTSR-II cavity versus the side length L of the RT for the incident polarization along the (a) x axis and (b) y axis.

find that the extinction properties of the RTSR cavity are highly sensitive to the polarization of the incident light, resulting in strong Fano resonances. The Fano resonances originate from strong coupling between the regular triangle and the split ring. It is found that the size and relative orientation of the regular triangle are crucial parameters for the Fano resonance since these parameters finely control the strength of the electromagnetic coupling and the effective capacitance of the metallic gap region. By using combinations of different symmetrical nanostructures we can actively modulate the Fano resonance spectra in a polarization dependent manner. Calculation results show that bulk refractive index sensitivities exceeding 800 nm/RIU, with a figure of merit exceeding 6.8 in the near infrared, are obtained with the RTSR cavity. These properties give the RTSR cavity potential applications in plasmonic Fano switches and sensing.

我们提出了一种由等边三角形和圆环构成的等离子体平板超材料,实现了等离子体诱导的透明现象。正三角形的偶极共振和圆环的四级共振之间的干涉导致了透明窗口的出现. 通过不同对称性的纳米结构的结合，我们实现了等离子体诱导的透明现象，并且展示出对入射光偏振的不敏感性。透射峰的透射效率高达 95.77%并且在我们的计算精度范围内波动范围在保持在 0.01%。

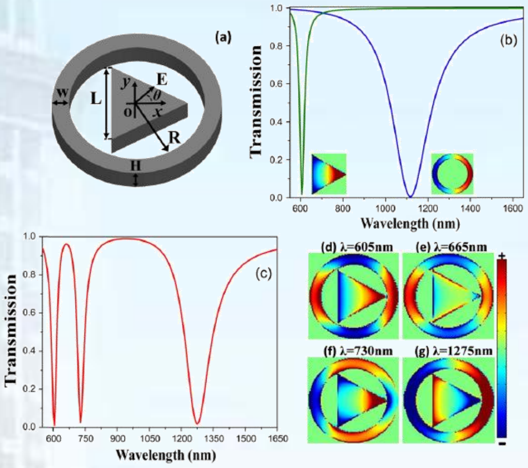

图27. 等离子体超材料的几何结构和模拟计算的光学属性。（a）等离子体超材料单元的几何结构：半径R=100纳米，厚度H=30纳米。（b）正三角形阵列（绿线）和圆环阵列（蓝线）的透射特性，内插图显示了共振波长处的电荷密度分布（c）提出的超材料的透射特性，几何参数：L=160纳米，宽度W=30纳米，偏振角θ=0°。(d)–(g)波长605纳米，665纳米，730纳米，1275纳米处的电荷密度分布在图23(c)。

Fig27. Structural geometry and simulated optical properties of the metamaterial. (a) The schematic illustration of the planar metamaterial cell and the incident light polarization. R (=100 nm) denotes the radius, H (=30 nm) is the thickness, W is the width and L is the side length. (b) The transmission spectra of the RT array (green line) with L = 160 nm and the ring array (blue line) with W= 30 nm. The insets show the charge density distributions at the dips. (c) The transmission spectra of our metamaterial array (L = 160 nm and W= 30 nm) under polarization angle θ=0°. (d)–(g) The corresponding charge density distributions of the transmission peak and dips at 605, 665, 730 and 1275 nm in figure 23(c).

We demonstrate plasmonic-induced optical transparency (PIT) in a planar

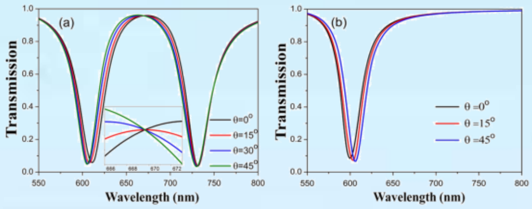

图28. 不同偏振角下的透射曲线。图（a）和（b）分别是平板超材料和正三角形的透射谱。内插图显示了669nm附近的透射谱。

Fig28. The transmission spectra for (a) the planar metamaterial and (b) the RT array at a different polarization angle θ. The inset shows the transmission spectra around 669 nm.

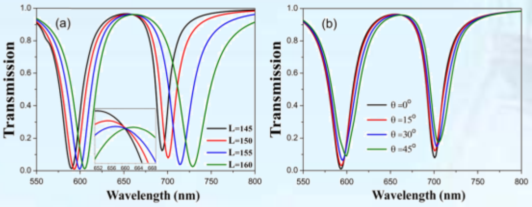

图29. (a) 偏振角θ = 0°情况下，超材料的透射谱随着边长L的演化曲线;（b）超材料的透射谱随着偏振角θ的演化曲线，其中L=150纳米。内插图展示了661纳米附近的透射谱。

Fig29. Transmission spectra of the planar metamaterial with (a) a different length L at polarization angle θ = 0° and (b) with a different polarization angle θ at length L = 150 nm. The inset shows the transmission spectra around 661 nm.

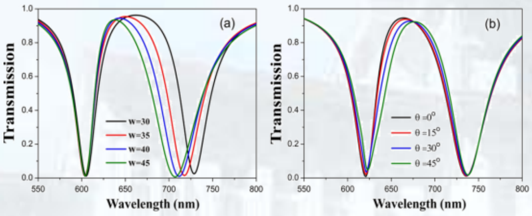

图30. (a) 偏振角θ = 0°情况下，超材料的透射谱随着宽度W的演化曲线;（b）超材料的透射谱随着偏振角θ的演化曲线，其中W=40纳米。

Fig30. Transmission spectra of the planar metamaterial (a) with a different width W at polarization angle θ = 0° and (b) with different polarization angle θ at width W= 40 nm.

metamaterial consisting of a metallic regular triangle (RT) embedded in a ring nanostructure. The interference between the bright dipole mode of the RT and the dark quadrupole mode of the ring leads to the emergence of a transparent window in the visible regime. By combining nanostructures with different degrees of symmetry, the PIT transmission properties of our metamaterial remain stable with respect to the incident polarization, showing polarization insensitivity to the incident wave. The transmission efficiency of the PIT peak for different polarizations can be maintained at greater than 95.77% with a fluctuation range of 0.01% in our calculation accuracy.

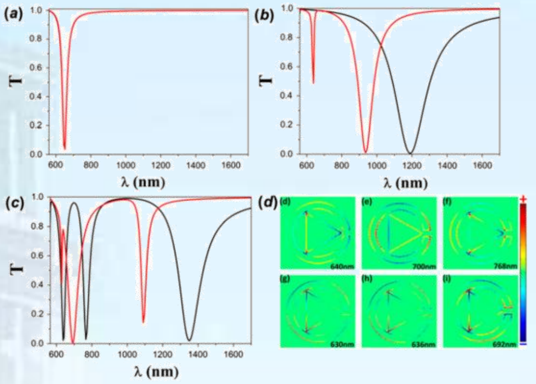

图31. (a)和（b）正三角形阵列（L=180纳米）和劈裂环阵列的透射谱;（c）提出的超材料的透射特性，几何参数：L=180纳米，黑线和红线分别对应于θ = 0° and 90°情况; (d) 透射峰或透射谷处的电荷密度分布在图2. (c)。

Fig31. The transmission spectra for the RT array with L = 180 nm (a) and the SR array (b). The transmission spectra for the RTSR metamaterials (c) with L = 180 nm. (d) The charge density distributions of the transmission peak or dip with wavelength less than 850 nm in the Figure 2(c). The black line and red line correspond to θ = 0° and 90°, respectively.

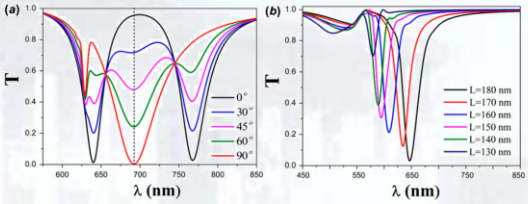

图32. （a）超材料在不同偏振角从0° 到 90°下的透射曲线。（b）正三角形在不同边长下的透射谱。

Fig32. (a) The transmission spectra for the RTSR metamaterials with L = 180 nm at different polarization angle θ from 0° to 90°. (b) The transmission spectra for the RT array with the incident polarization angle θ = 0° and L range from 130 to 180 nm.

我们研究了在等离子体微纳结构中的电磁感应透明现象，这种微纳结构单元由正三角形和劈裂环构成。基于正三角形和劈裂环之间不同的耦合方式，我们通过改变入射光的偏振角实现了对于电磁感应透明谱的主动调制。基于这一点，我们提出的超材料

能被用作光学开关，其开关效率能够达到95%。正三角形的尺寸很好地控制着其与劈裂环之间的耦合强度，从而能够很好地调制电磁感应透射谱响应。此外，透射谱对于周围的环境显示出高的敏感度，在传感方面展示了潜在的应用。

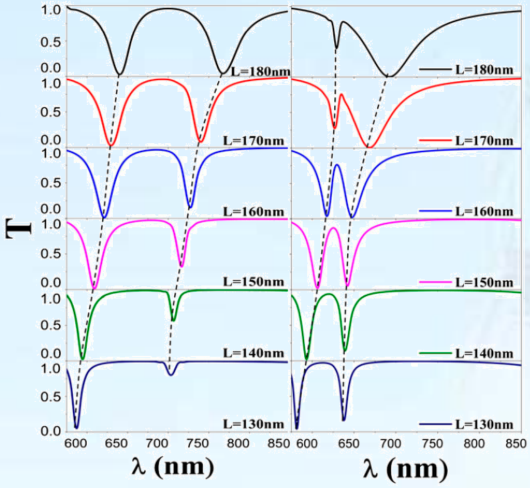

图33. 偏振角θ = 0°（左栏）和θ = 90 °（右栏）情况下，超材料的透射谱随着边长L的演化曲线。

Fig33. The transmission spectra of the RTSR metamaterials at different L excited by incident light with the polarization angle θ = 0° (left column) and 90° (right column).

We have investigated an analog of electromagnetically induced transparency (EIT) in planar metamaterials by a metallic regular triangle (RT) embedded in split ring (SR) nanostructure. It is demonstrated that, depending on the different coupling ways between the RT and the SR, the EIT-like spectral response can be actively modulated by simply adjusting the incident light polarization angle. Based on this observation, an on-to-off active modulation of the EIT-like transparency window can be realized, and it can serve as the base for an optical switching with the switching efficiency exceeding 95%. The size of the RT finely controls the coupling strength between the RT and the SR. It is shown that the EIT-like transparency window can be enhanced or suppressed by adjusting the size of the RT, which shows the big modulation to the EIT-like spectral response. Furthermore, the transmission spectra show potential applications in sensing due to high sensitivity of about 600 nm/RIU with figure of merit exceeding 36 to the surrounding environment.

(3) 光子晶格体系中的光传输

Light propagation in photonic lattices

我们理论研究了一维光子晶格中基于三个负缺陷的导光特性，线性的情形下这三个缺陷可以实现分光的功能，发现分光能力的大小可以通过调节缺陷的深度来实现。我们发现当缺陷的深度为零时，分光现象消失，但是利用非线性又可以重新实现分光的功能，我们还发现相同的结构可以同时实现多色光的分束。

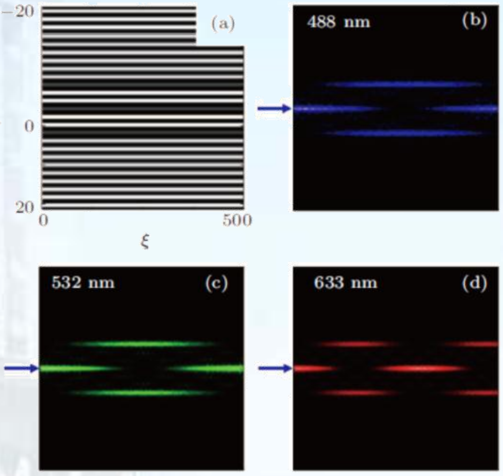

图34. 不同波长的光在相同的三缺陷晶格中的分光与合光现象。

Fig34. Splitting dynamics of a light beam with different wavelengths in the same setting of the tri-core photonic lattices.

We report on theoretical investigations of beam control in one-dimensional tri-core photonic lattices (PLs). Linear splitting is illustrated in tri-core PLs; the effect of defect strength on the splitting is discussed in depth for single-wavelength light. We reveal that splitting disappears when the defect strength trends to zero, while reoccurring under nonlinearity. Multi-color splitting and active control are also proposed in such photonic structures.

我们理论与实验研究了两翼夹角为非90 度情形下畸变二维艾里光束的加速及传播特性。我们的结果表明这些畸变的二维艾里光的加速度取决于初始两翼的夹角。其主

瓣仍然沿着抛物线的轨迹传播，但是与两翼为 90 度不同，其能量的最大值位置与主瓣的轨迹不同，具有双轨迹的特征。这两个轨迹都可以通过两翼的夹角来控制。由于自修复特性，这些畸变的艾里光束通过一段距离的传播后都倾向于演化成一维或者是二维的艾里光。我们的理论结果与实验结果符合的很好，能够清楚的解释为什么两翼的夹角越大，畸变艾里光束的加速度会越大。

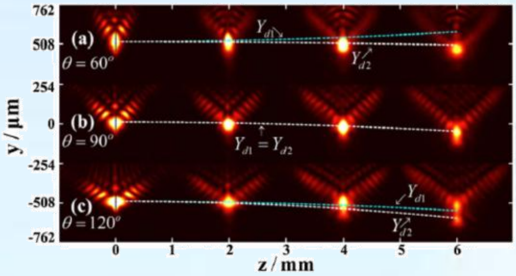

图35. 不同夹角的艾里光束在不同传播距离处横向光强分布的实验结果。

Fig35. Experimental results showing the transverse intensity patterns captured at different propagation distances for 2D Airy beams with different initial angles between the two wings.

We study both numerically and experimentally the acceleration and propagation dynamics of 2D Airy beams with arbitrary initial angles between their “two wings.” Our results show that the acceleration of these generalized 2D Airy beams strongly depends on the initial angles and cannot be simply described by the vector superposition principle (except for the normal case of a 90 ° angle). However, as a result of the “Hyperbolic umbilic” catastrophe (a two-layer caustic), the main lobes of these 2D Airy beams still propagate along parabolic trajectories even though they become highly deformed. Under such conditions, the peak intensity (leading energy flow) of the 2D Airy beams cannot be confined along the main lobe, in contrast to the normal 90 °case. Instead, it is found that there are two parabolic trajectories describing the beam propagation: one for the main lobe, and the other for the peak intensity. Both trajectories can be readily controlled by varying the initial wing angle. Due to their self-healing property, these beams tend to evolve into the well-known 1D or 2D Airy patterns after a certain propagation distance. The theoretical analysis corroborates our experimental observations, and explains clearly why the acceleration of deformed Airy beams increases with the opening of the initial wing angle.

我们研究了一维耦合波导阵列界面的异常光折射行为。结果表明，当在体系中引入适量的结构无序（如宽度无序）时，一维无序耦合波导阵列界面上的光折射性质与周期波导阵列界面上的光折射性质截然不同（如图 36 所示）。当入射光初始横向波矢位于第一布里渊区时，光波在无序耦合波导阵列体系中基本上沿初始激发波导方向（即垂直于界面方向）向前传输。这主要是由于一维无序耦合波导阵列中位于第一通带中的本征模式的横向传播速度趋于零所致。无序体系中这种反常折射行为提供了一种有效的光波准直方法。

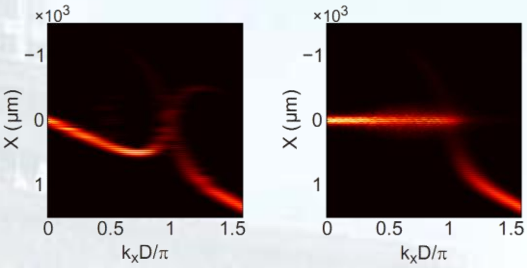

图36. 出射面光束位置与入射倾角（以入射光横向波矢k_x表示）的关系。(a)为均匀周期波导阵列对应的结果。(b)为引入Δ_w=2.0 μm宽度无序波导阵列对应的结果。

Fig36. Transverse positions of the output beam at different input tilts. (a) is the case for a uniform periodic waveguide array, and (b) is the case for a width-disordered waveguide array, respectively.

We have studied the anomalous light refraction behavior at the entrance surface of the disordered one-dimensional waveguide arrays. By introducing the lattice disorder into the uniform periodic waveguide arrays, anomalous refractive behaviors can be observed (as shown in Fig. 32). The results show that the light will always be confined tightly around and propagate along the initially exciting waveguides when the transverse wave vector components of the incident light are within the first Brillouin zone of the waveguide array. This is due to the fact that the transverse propagation velocities of the eigenmodes in the first band are dramatically suppressed. This also provides an effective way to couple and collimate a diverging light beam into a disordered waveguide array.

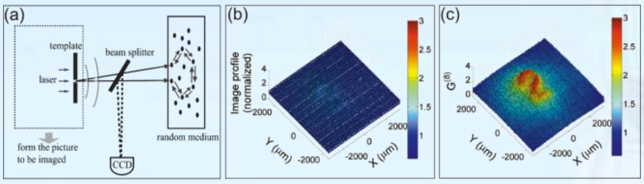

图37. (a) 基于相干背散射效应的无透镜成像实验示意图。(b) 对于一个图形“2”，直接测量得到的无透镜成像实验结果。(c) 采用光子相关测量技术，测量8阶光强相关函数得到的成像结果。

Fig37. (a) is the experimental setup for lensless imaging based on coherent backscattering from random medium. (b) is the direct normalized image profile for an object '2', and (c) is the image formed by performing the 8th-order intensity correlation measurement on the image plane, respectively.

我们在理论上和实验上系统地研究了基于随机散射体相干背散射光的无透镜成像效应（实验示意图如图 37(a) 所示），给出了成像系统的点扩散函数。以聚苯乙烯微球悬浊液为例，实验上研究了散射体中的散射粒子的粒径、含量以及介质体系与图像之间的距离对成像质量的影响，通过优化实验参数，提高了像的对比度以及分辨率。进一步采用光子相关测量技术，通过在像平面测量相应的高阶光强相关函数，极大地提高了复杂图像成像的对比度和分辨率（如图 37(c) 给出的对图形“2”的成像结果）。理论分析和实验结果表明，采用光子相关测量技术，对于复杂物体这种无透镜成像技术仍然是线性响应的，即可以对含有不同灰度信息的图像进行成像并获得很高的对比度而不发生畸变。

We studied the lensless imaging technique based on coherent backscattering in random medium both theoretically and experimentally (as shown in Fig. 33(a)). The corresponding point spread function of such imaging system has been derived. By optimizing various parameters, such as the volume fraction of the scatterer in the random scattering medium, the diameter of the scatterer, the distance between the object to be imaged and the surface of the random scattering medium, the image contrast and resolution can be improved. Moreover, for complicated objects, high contrast and quality images can be achieved through the high-order intensity correlation measurement on the image plane (as shown in Fig. 33(c)), and we theoretically and experimentally demonstrated that the imaging system is linear with the high-order intensity correlation measurement for complicated objects.

(4) 飞秒超快探测技术

Detection technology using fs laser pulses

我们利用非简并波长交换技术测量了 ZnS 非简并双光子吸收系数以及热电子的激发态弛豫时间。实验基于泵浦探测实验装置，将飞秒光（1kHz, 800 nm, 200fs）分为两束，将其中一束倍频获得 400nm 的脉冲光。首先利用 800 nm（1.55 eV）作为泵浦光，400nm（3.10eV）作为探测光。由于 ZnS 的带隙为 3.54 eV，当泵浦光和探测光在时间和空间上重合时，可以观察到非简并双光子吸收，测得非简并双光子吸收系数为 7.52 cm/GW。其次，通过增加 400nm 光的强度并减小 800 纳米光的强度，从而交换了泵浦光和探测光的波长。在 400 nm 泵浦，800 nm 探测的情况下，观察到了两个非线性过程，包括非简并双光子吸收和三光子吸收。前者是瞬态的，而后者的弛豫过程则体现了由泵浦光简并双光子吸收产生的激发态电子的寿命，测得 ZnS 的导带自由电子的寿命为 0.35 ns。这种技术为我们更全面的理解基于 ZnS 或其他材料光开关的工作原理提供了极大的帮助。

A wavelength swapping nondegenerate pump-probe technique to measure the magnitudes of the nonlinear optical dynamics as well as the relaxation time of electrons in high energy levels is presented using a ZnS single crystal wafer as an example. By pumping the sample with 800 nm femtosecond pulses and probing at 400 nm, nondegenerate two-photon absorption (N-2PA) happens exclusively, and the measured curves only show instantaneous features without relaxation tails. The N-2PA coefficient was derived explicitly as 7.52 cm/GW. Additionally, when the wavelengths of the pump and probe beams are swapped, extra information about the relaxation time of the hot electrons excited in the conduction band is obtained. The combined results above are helpful for evaluating the characteristics of an optical switches based on ZnS or other materials with respect to its nonlinear optical dynamic aspect.

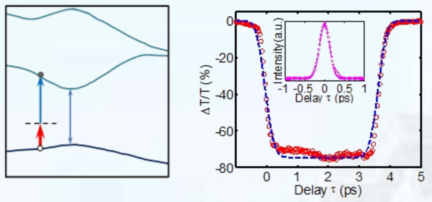

图38. (a) 800nm泵浦400nm探测时的非简并双光子吸收过程。(b) 400nm探测光的差分透过率随时间的变化。

Fig38. (a) The N-2PA process involved in the configuration of pumping at 800 nm and probing at 400 nm. (b) Differential transmittance change of the probe (400 nm) in ZnS. Blue dashed curve is the fit of experimental data. The inset shows autocorrelation trace of the fundamental 800 nm pulses.

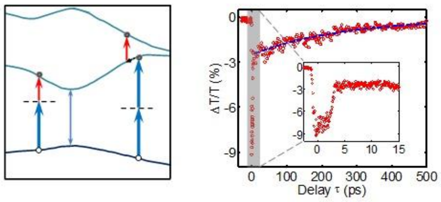

图39. (a) 400nm泵浦800nm探测时的简并双光子吸收、非简并双光子吸收和激发态吸收过程。(b) 800 nm探测光的相对透过率随时间的变化。

Fig39. (a) Schematic representation of the transitions involved in N-2PA, D-2PA, in addition the free-carrier absorption from subband 1 to subband 2 under 800 nm light is shown. (b) Relative nonlinear transmission to the linear transmittance (ΔT/T) versus time delay under excitation at 400 nm and probing at 800 nm. The blue dashed line is a mono-exponential fit of the relaxation tail. The inset gives the details near the zero delay time.

由于光克尔效应，一束飞秒泵浦光会在克尔非线性介质中形成瞬态克尔透镜。当另外一束被传统光学透镜汇聚的探测光与泵浦光共线的通过这一透镜时，探测光的传播方向也会受到影响，这一效应将会反映在透过远场中心光阑的透过率上，和传统的闭孔 Z 扫描现象相似。如果探测光的焦点在瞬态透镜之前，光束将被再次汇聚，导致远场透过率的增加；如果探测光的焦点在瞬态透镜之后，光束整体焦点被进一步提前，从而导致远场透过率的降低。如果该效应是由飞秒泵浦光所诱导，对于探测光而言就可以作为一个瞬态光学快门，可用于分辨探测光的时域特性。由于瞬态克尔透镜效应广泛存在于各种光学介质中，且对光的偏振没有要求，因此这种基于闭孔 Z 扫描配置的光学快门技术不需要特殊非线性介质和相位匹配条件，同时也对泵浦-探测光的偏振关系没有要求。

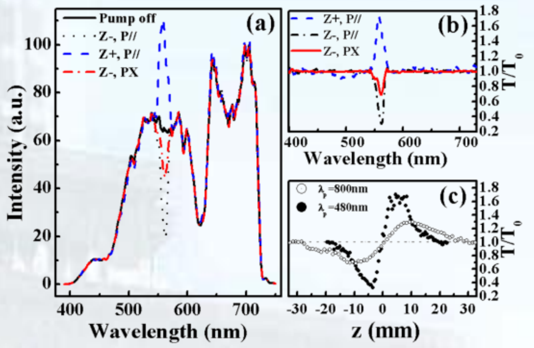

图40. 基于闭孔Z扫描配置的瞬态克尔透镜光学快门技术原理。

Fig40. (a) WLC reference spectrum generated in water and Kerr lens gated WLC spectra by IR pump with polarization parallel or perpendicular to the WLC probe for FS plate at Z- or Z + respectively. (b) Normalized transmission spectra of (a). (c) Closed aperture Z-scan signal of the IR pump at 800nm and the probe at 480nm.

A convenient polarization independent, broadband femtosecond optical gating technique utilizing transient Kerr lens effect is demonstrated by measuring the chirp structure of linearly polarized or non-polarized white light continuum generated in water and a photonic crystal fiber, respectively. Comparing with previous time-resolved spectroscopic techniques, this Kerr lens gating method is not limited by the requirement of specific nonlinear media with broadband response, critical phase-matching conditions, and especially the pump-probe polarization relationship. By replacing the white light continuum with other broadband light signals of interest, this method can be exploited in other femtosecond time-resolved spectroscopy, e.g., femtosecond photoluminescence.

当一束探测光非共线的通过一束泵浦光在克尔介质中诱导的克尔瞬态透镜时，探测光的传播方向会发生瞬态偏折，导致远场透过率的瞬态改变，我们论证了该效应可以实现飞秒时间分辨光学快门的功能。由于该效应的来源是瞬态克尔透镜效应，这种光学快门技术具有之前的基于光克尔透镜的快门技术的所有优点，比如不需要泵浦-探测光的相位匹配条件，不需要特殊非线性介质，不需要泵浦-探测光的特殊偏振要求等。同时，由于是非共线配置，不需要过滤泵浦光，从而可探测的带宽也得到了进一步的拓展。

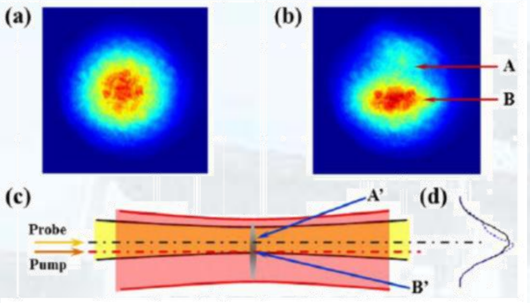

图41. 单色光的光束偏折效应的直接成像和原理。探测光非共轴的通过泵浦光诱导的克尔透镜时，一部分光向透镜轴的方向偏折，导致远场光斑的畸变，如（b）所示，这反映到远场强度分布的改变，如（d）所示。

Fig41. Direct imaging of the transient beam deflection of the single color probe. (a) Initial profile of the probe; (b) distorted beam profile of the probe due to beam deflection for an average pump power at 0.8 mW; (c) illustration of the deflection mechanism using side view picture of the pump (red) and probe (yellow); (d) intensity profile of the probe in (c) with (blue dashed line) and without (black solid line) deflection effect.

A simple but robust ultra-broadband femtosecond optical gating method utilizing transient beam deflection effect is demonstrated with direct CCD imaging of the distorted single-color probe and the measurement of the chirp structure of a white light continuum generated from a CaF2 plate. The non-collinear configured beam deflection gating technique not only preserves all the advantages of the previous optical Kerr lens based gating methods, such as having no phase matching conditions, little dependence on probe intensity or special nonlinear media, and no requirements on the pump-probe polarization relationship, but it also extends the measurable probe bandwidth. Meanwhile, it is also proved that the current gating technique is easy-aligned, free from the influence of the pump-probe pulse-front mismatch and the probe beam profile, which is much convenient for the characterization of ultra-broadband light pulses in the applications of ultrafast spectroscopy.

(5) 生物光子学
Biophotonics

Fluo-3 AM 染色效果直接关系到钙信号的成像质量。Fluo-3 AM 染色可分为负载和酶切两部分，通过控制负载温度和酶切温度，发现在 4℃负载和 20℃酶切条件下，成骨细胞（一种贴壁细胞）核区荧光强度明显高于胞浆区的荧光强度，约为胞浆区荧光强度的 2 倍（图 42）。根据 Fluo-3 在细胞核内与核外的发光性质不用，即：在相同的钙浓度情况下，细胞核液中 Fluo-3 的荧光强度比胞浆液中高出 1 倍，我们推测造成核亮的原因很取决在于细胞内的酯酶以及同时存在于核膜和细胞膜上的主动转输蛋白工作状态。酯酶负责将细胞中的Fluo-3 AM分解成游离态的 Fluo-3，游离态的 Fluo-3 很快和细胞内游离的钙离子结合发出荧光。酯酶的活性受温度影响，20℃~37℃时比较活跃。游离的 Fluo-3 带电荷，只能被主动转运蛋白转送到细胞外。而这种蛋白对温度敏感，在 37℃时非常活跃，在 20℃时活性较低，而在 4℃时活性几乎为 0。所以 4℃负载时，Fluo-3 AM 在被酶切之前尽可能多地进入细胞核，保证 Fluo-3 AM 在细胞中的均匀分布；20℃酶切既确保了酯酶活性又限制了主动转运蛋白

的活动，从而保证游离态 Fluo-3 细胞中的均与分布。因此，在 4℃负载和 20℃酶切条件下，Fluo-3 荧光成像呈现出核区明亮的现象。同时我们发现核亮的现象与细胞贴壁效果好坏有关，在贴壁效果不好的 BV-2 细胞中，核亮的现象并不明显。本工作为 Fluo-3 AM 应用提供了新的方法，理想的细胞核钙荧光成像为利用快速成像研究细胞核钙和胞浆钙活动的差异性提供了有力的技术支持。

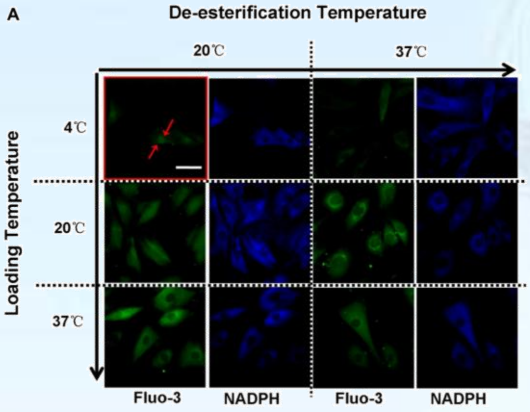

图42. 不同负载温度和酶切温度对Fluo-3 AM探针在成骨细胞中染色效果的影响。

Fig42. Fluorescence data for osteoblast cells stained at different loading and de-esterification temperatures. Representative fluorescence images of Fluo-3 and NAD(P)H. Osteoblast cells were loaded for 20 min at 4℃, 20℃ and 37℃, respectively. Then they were de-esterified at for 30 min at 20℃ or 37℃, respectively. The images of NADPH (blue) always exhibited dark nuclear area.

Fluo-3, a potent calcium indicator, has been extensively used to study intracellular calcium in various cell types in vitro. There are two conventional methods for staining: (1) direct injection and (2) Fluo-3 acetoxymethyl ester (AM) loading. AM-loaded cells usually show a darker fluorescence in nucleus than in cytoplasm, while direct injection always results in a brighter nucleus which is more responsive to nuclear calcium. Considering the disadvantages of direct injection, like cell damage, time waste, and operation complexity, it is necessary to develop a new method of Fluo-3 AM staining to acquire a brighter nucleus without such problem as encountered in the direct injection. In the present work, we mainly focused on the staining effects of loading and de-esterification temperatures on the fluorescence intensity of Fluo-3 in response to $[Ca^{2+}]_n$ and $[Ca^{2+}]_c$ in adherent cells, including osteoblast, HeLa and BV2 cells. Fortunately, we found that cold loading (4℃) and room temperature de-esterification (20 ℃) definitely induced a brighter fluorescence in nucleus than in cytoplasm in osteoblast cells. Brighter nuclei were also obtained HeLa and BV2 cells with the same experimental condition. Besides, loading time had effect on fluorescence intensity. Furthermore, we found that the method was suitable for strongly adherent cells but not for weekly adherent cells, indicating dependence on cell adhesion quality. Finally, the results can be explained in the framework of a qualitative model considering a competition between diffusion, de-esterification and organic anion-driven transport processes.

类风湿关节炎（Rheumatoid arthritis，RA）是一种以关节滑膜炎为主要特征的慢性全身性免疫疾病，主要病理环节依次为免疫功能的异常，关节滑膜细胞的积聚与滑膜增厚，关节软骨和骨的破坏。滑膜病变在 RA 的病理过程中起到“承上启下”的关键作用。RA 滑膜细胞中存在和表达多种温度敏感的瞬时受体电位（transient receptor potential，TRP） 通道蛋白家族成员，包括 TRPA1、TRPV1、TRPV4、TRPM8 等。这类受体通道在响应胞外刺激被激活后，通过引发细胞外钙离子内流等信号机制介导调节滑膜细胞的病生理过程。我们的工作主要研究 TRPM8 在类风湿关节炎滑膜细胞中的功能。该通道可被冷刺激和薄荷醇激活，参与温度觉和疼痛觉调控，尤其在调节细胞生长和死亡方面具有重要作用。我们通过实验检测了滑膜细胞中 TRPM8 通道的表达情况，进一步发现 TRPM8 通道被薄荷醇激活后能剂量依赖性诱发细胞内钙浓度升高，氧自由基的大量产生，线粒体膜去极化以及凋亡相

关蛋白 caspase3/7 的活化等过程，最终导致滑膜细胞凋亡（图 43）。由于 RA 滑膜病变的主要表现之一为滑膜细胞的异常增生和抗凋亡能力增强，因此抑制滑膜增生诱导细胞凋亡可作为潜在的 RA 的治疗靶点，我们的这些研究结果为寻找和探索有效的 RA 的治疗药物和药物靶点提供了一些细胞生物学的基础和依据。

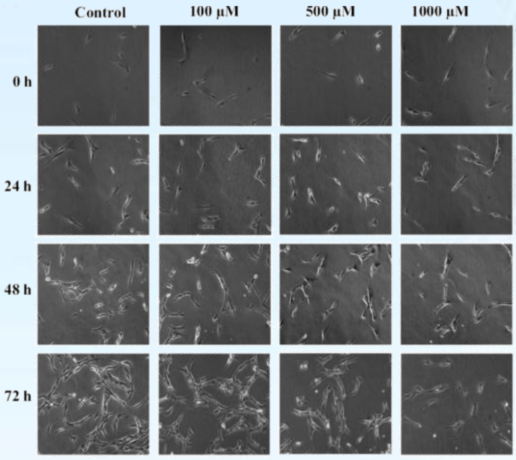

图43. 薄荷醇抑制类风湿关节炎滑膜细胞的增殖。

Fig43. Menthol decreased the survival of synoviocytes. Synoviocytes were stimulated by menthol (100, 500, 1000 μM) for 24, 48 and 72 h, respectively.

Rheumatoid arthritis (RA) is an autoimmune and chronic disease characterized by inflammatory synovitis, leading eventually to cartilage and bone destruction. Transient receptor potential melastatin (TRPM) channels, the largest subfamily of TRP class, perform diverse functions ranging from detection of cold, osmolarity, redox state and cell proliferation or death. In the present study, it was observed that menthol, the specific agonist of transient receptor potential melastatin subtype 8 (TRPM8), could induce sustained increases of cytosolic calcium concentration ($[Ca^{2+}]_c$) in synoviocytes isolated from collagen-induced arthritis rats in dose-dependent manner, which was evidently blocked by applying an extracellular Ca^{2+}-free buffer. Besides, RT-PCR indeed demonstrated presence of TRPM8 in the synoviocytes. Meanwhile, it was found that menthol evoked intracellular reactive oxygen species (ROS) production. Further experiments showed that menthol reduced the cell numbers and survival of synoviocytes. This reduction was associated with apoptosis as suggested by mitochondrial membrane depolarization, nuclear condensation and a caspase 3/7 apoptotic assay. Taken together, our data indicated that menthol resulted in synoviocyte death associated with apoptosis via calcium entry and ROS production depending on TRPM8 activation. Our findings in this work could provide some cellular basis for the anti-inflammatory utility of menthol, and may facilitate the development of new therapeutic drugs against RA targeting TRPM8 receptors.

骨骼的形成与重建是成骨细胞主导的骨生长与破骨细胞介导的骨吸收之间达到动态平衡的结果，破骨细胞会释放多种蛋白酶、碳酸酐酶、乳酸及柠檬酸等来溶解并且吸收骨基质。此时将导致细胞外 Ca^{2+}浓度的变化，血液中 Ca^{2+}浓度为 1.1 mM 到 1.3 mM，而在破骨细胞的重吸收过程中细胞外 Ca^{2+}浓度可达到 8 mM 到 40 mM。胞外钙浓度上升直接抑制破骨细胞的活性，刺激成骨细胞活性。有报道表明，细胞外 Ca^{2+}浓度升高会促进成骨细胞的增殖、矿化等过程，但是具体机制目前尚未明了。在本研究中，我们发现细胞外钙浓度依赖的诱发成骨细胞内钙浓度升高（图 44），并进一步证明是钙库控制的钙内流机制（Store operated calcium entry, SOCE）。SOCE 的活化依赖于细胞膜 Ca^{2+}敏感受体（Calcium-Sensing Receptors，CaSR）介导的 PLC-IP_3-Ca^{2+}释放信号途径，进一步证明外钙激活的 CaSR-SOCE 机制与促成骨细胞增殖效应相关。本工作为成骨细胞的增殖机制提供了新的思考视角，并为阐明骨形成与重构的生理过程提供了一定细胞生物学的依据。

In bone microenvironment, the resorption of osteoclasts results in a local accumulation of extracellular calcium concentration ($[Ca^{2+}]_o$) which can stimulate osteoblastic proliferation and promote bone formation. However, the intracellular signaling activated by extracellular Ca^{2+} in osteoblasts is not clear. In many cell types, the store operated calcium entry (SOCE) plays critical roles in regulating cell proliferation through inducing sustained increases in cytosolic Ca^{2+} concentration ($[Ca^{2+}]_c$). Thus, in the present work, we examined whether elevating $[Ca^{2+}]_o$ can induce $[Ca^{2+}]_c$ increase in osteoblasts, then investigated the mechanisms underlying this $[Ca^{2+}]_c$ increase, and finally tested the contribution of $[Ca^{2+}]_o$-induced SOCE in osteoblastic proliferation. The significances of this study are that we found that elevation of $[Ca^{2+}]_o$ triggered SOCE in osteoblasts, the SOCE was dependent on the activation of calcium-sensing receptors (CaSR) and phospholipase C (PLC), and the CaSR/PLC-related SOCE activation contributed to high $[Ca^{2+}]_o$-induced osteoblastic proliferation. These findings described in this manuscript could lead to new insights in the mechanisms of osteoblastic proliferation, and provide some cellular basis for physiological regulation of bone remodeling.

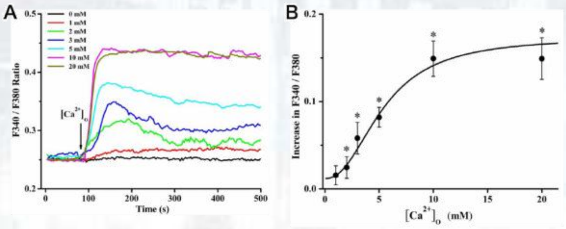

图44. 细胞外钙以浓度依赖的方式诱发成骨细胞内钙浓度升高。

Fig44. Elevated $[Ca^{2+}]_o$ resulted in $[Ca^{2+}]_c$ increases in rat calvarial osteoblasts. (A) Representative tracings of $[Ca^{2+}]_c$ responses induced by $[Ca^{2+}]_o$ at 0, 1, 2, 3, 5, 10 and 20 mM, respectively. (B) The statistic peak values of increase in F340/F380 ratio were plotted against $[Ca^{2+}]_o$, * showed $P<0.05$..

.

光谱表征及传感技术/Spectral Charaterization and Sensing Techniques

负责人：宋 峰

本方向涉及制备稀土发光材料，研究稀土材料发光的机理及其应用，以及应用光谱学和光谱仪器等方面。取得的代表性成果如下：

In this field, we mainly focused on the preparation of rare earth luminescent materials, the research of their mechanisms of luminescence and their applications, applied spectroscopy and spectral instrument. Some representative results are as follows:

用高温固相法制备了 Mn^{2+}，Sm^{3+}单掺和 Mn^{2+}/Sm^{3+}双掺的磷酸盐透明玻璃。通过测量材料的吸收谱、激发谱，分析了 Mn^{2+}/Sm^{3+}的能量传递过程，通过掺杂 Mn^{2+}金属离子，监测 Sm^{3+}的 597 发射波长，激发范围拓宽到 300nm-560nm 的范围，这种 Mn^{2+}/Sm^{3+}掺杂磷酸盐宽激发范围能够有效的把更多太阳光中对植物光合作用无效的光子转变为红橙范围的光子。

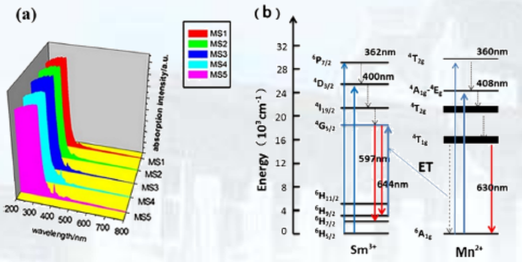

图1. （a）Mn^{2+}/Sm^{3+}双掺的吸收谱（b）Mn^{2+}/Sm^{3+}之间的能量传递过程。

Fig1. The absorption spectra of (a) Mn^{2+}/Sm^{3+} co-doped samples and (b) energy level diagrams of Sm^{3+} and Mn^{2+}.

Transparent Mn^{2+}, Sm^{3+}, Mn^{2+}/Sm^{3+} co-doped phosphate glasses for greenhouses have been feasibly prepared through high temperature melting method. The absorption and excitation spectra have been investigated. Based on the above spectra, the energy transfer from Mn^{2+} to Sm^{3+} have been assumed. By monitored at 597 nm, the excitation range for the co-doped samples is broadened from 300 nm to 560 nm in the case of combining Sm^{3+} and Mn^{2+} together. The broad excitation range for the Mn^{2+}/Sm^{3+} co-doped phosphate glasses can significantly help to turn more useless photons which are useless for plant photosynthesis in solar spectra to red–orange scope.

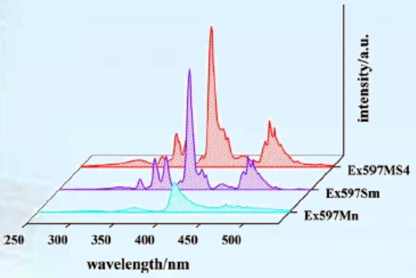

图2. 监控597nm波长下单掺Mn^{2+}，Sm^{3+}，双掺Mn^{2+}/Sm^{3+}的激发谱。

Fig2. The excitation spectra of Mn2+ single doped, Sm3+ single doped and MS4 (marked as Ex597Mn, Ex597Sm and Ex597MS4, respectively) monitored at 597 nm.

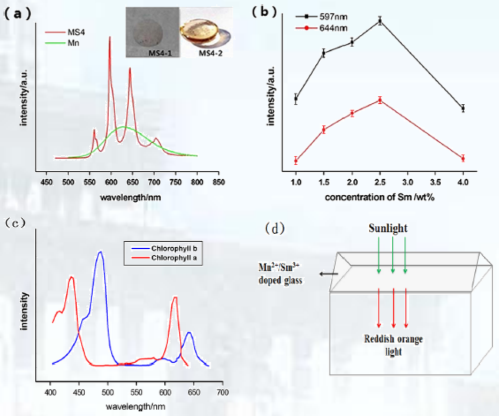

图3. （a）单掺Mn^{2+}和双掺Mn^{2+}/Sm^{3+}的发射光谱；（b）发射强度跟Sm^{3+}强度关系；（c）叶绿素a，叶绿素b的吸收谱；（d）Mn^{2+}/Sm^{3+}双掺材料对太阳光的转化图。

Fig2. (a) The emission spectra of Mn^{2+} single doped (excited by 408 nm) and MS4 (excited by 400 nm) phosphate glass; the inset is real photos of MS4: the MS4-1 is taken inside the room without direct sunrays and the MS4-2 is taken under sunlight. (b) Emission peak intensity dependence on the concentration of Sm^{3+}. (c) Absorption spectra of chlorophyll a and chlorophyll b. (d) Schematic diagram of solar conversion with Mn2+/Sm3+ co-doped glass in greenhouses.

通过对比单掺Mn^{2+}和Mn^{2+}/Sm^{3+}的发射谱，我们可以看到 Mn^{2+}/Sm^{3+}红橙光的发射

强度有很大的提高，比较叶绿素 a 和叶绿素 b 的吸收谱，可以明显的看到 Mn^{2+}/Sm^{3+}发射红橙光范围 590nm-680nm 刚好位于叶绿素 a 和叶绿素 b 的最大吸收范围。

In comparison to emission spectra of Mn^{2+}, Mn^{2+}/Sm^{3+}, we can clearly observe that the intensity has been greatly enhanced. More significantly, the emission range of Mn^{2+}/Sm^{3+} codoped sample, namely, 590nm-680nm, matches well with the absorption spectra of chlorophyll a and chlorophyll b. This higher luminescent efficiency will be helpful to promote the utilization of sunlight in greenhouses.

同时我们也研究了橙/红比随着 Sm^{3+}浓度的变化，研究结果表明，随着 Sm^{3+}掺杂浓度的增大，橙红比是不断减小的，很好的诠释了能量从 Mn^{2+}-Sm^{3+}传递过程，因此我们可以通过调节 Mn^{2+}，Sm^{3+}浓度来调节红橙比。

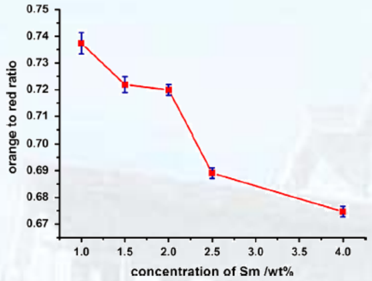

图4. 橙红比跟Sm^{3+}浓度之间的关系。

Fig4. The orange to red ratio dependence on the concentration of Sm^{3+}.

From the emission spectra of all Mn^{2+}/Sm^{3+} co-doped samples, the orange/red emission ratio change regulation with the Sm^{3+} concentration has been calculated to investigate light quality variation for different plants. All of the results are shown in Fig. 4. We can observe that orange/red ratio decreases with Sm^{3+} concentration increasing and the result of MS1, MS2, MS3, MS4, MS5 is 0.7374: 0.7219: 0.7199: 0.6891:0.6747. This result commendably acts in cooperation with the energy transfer efficiency. Another regulation is that the absolute value of total orange or red emission shows the same regulation with peak intensity. So we can draw a conclusion that we can easily adjust total emission amount and the light quality (orange/red) by changing doping amount and ratio of Sm^{3+}/Mn^{2+}.

通过溶胶凝胶法制备了 Er^{3+}，Yb^{3+}掺杂的 $Y_2Ti_2O_7$ 纳米晶以及不同退火温度对其发光的影响。图 5 可知，Er^{3+}，Yb^{3+}掺杂的样品在 975nmLD 激发下，产生了绿光和红光的荧光发光。位于 525nm/546nm 的绿光上转换发光带对应于 Er^{3+}：$^2H_{11/2}/^4S_{3/2}\rightarrow{}^4I_{15/2}$ 的跃迁。620nm 到 720nm 的红光上转换发光对应于 Er^{3+}：$^4F_{9/2}\rightarrow{}^4I_{15/2}$ 的跃迁。在 800℃的退火下，由于纳米晶的存在，红光和绿光的上转换发光发生能级劈裂。在 800℃的退火温度下，红光发光强度为 700℃退火下发光强度的 25 倍。

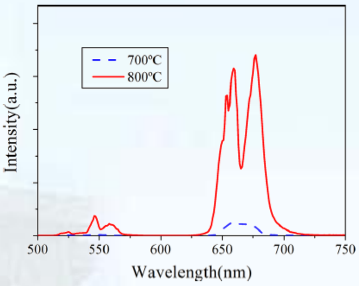

图5. Er^{3+}，Yb^{3+}掺杂的$Y_2Ti_2O_7$纳米晶在700℃和800℃退火之后，975nm泵浦激发下可见区域的上转换发光。

Fig5. Upconversion fluorescence spectra of 700 ℃ and 800 ℃ annealed samples under 975nm excitation.

Er^{3+}-Yb^{3+} rare earth ions co-doped $Y_2Ti_2O_7$ luminescent materials have been prepared by sol-gel method and investigated the influences of luminescence in various annealing temperature. Fig. 5 depicts the upconversion emissions spectra of the samples annealed at 700 ℃ and 800 ℃ under 975 nm LD excitation. The green and the red fluorescence emissions originate from the inner 4f-4f electronic transitions of the Er^{3+} ions. The green UC emission band at 525-546 nm corresponds to the transitions of Er^{3+}: $^2H_{11/2}/^4S_{13/2}\rightarrow{}^4I_{15/2}$, and the red UC emission band corresponding to the transition of

$^4F_{9/2}\rightarrow{}^4I_{15/2}$ ranges from 620 nm to 720 nm. As Fig. 5 shows, it is obvious that the red UC emission band of the sample annealed at 800 ℃ splits into two main bands which peaked at 659 nm and 677 nm on account of the presence of nanocrystalline. Similarly, the green UC emission corresponding to $^4S_{13/2}\rightarrow{}^4I_{15/2}$ also splits in contrast to the amorphous sample. The intensity of red fluorescence emission is much stronger than that of the two green emissions.Furthermore, the intensity of red UC emission of the 800 ℃ annealed sample is about 25 times as strong as that of the 700 ℃ annealed amorphous sample.

如图 6 所描述，通过监测 Er^{3+}，Yb^{3+}掺杂样品的近红外区域的荧光发光，出现了 1528nm 的发光，对应于 Er^{3+}: $^4I_{13/2}\rightarrow{}^4I_{15/2}$ 的跃迁。与上转换发光类似，样品在 800℃退火下，1528nm 的近红外发光强度是 700℃退火下发光强度的 20 倍。

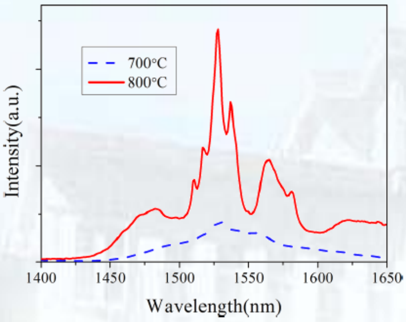

图6. Er^{3+}，Yb^{3+}掺杂的$Y_2Ti_2O_7$纳米晶在700℃和800℃退火之后，975nm泵浦激发下近红外区域的上转换发光。

Fig6. Near-infrared emission spectra of 700℃ and 800℃ annealed samples under 975nm excitation.

As pictured in Fig. 6, the broad near-infrared band peaks at 1528 nm in the range of 1450 nm-1650 nm which originates from the transition of $^4S_{13/2}\rightarrow{}^4I_{15/2}$ of Er^{3+} ions. Similar as the UC emissions, the intensity of NIR emission of the sample annealed at 800 ℃ is about 20 times stronger than that of the sample annealed at 700℃.

上转换和近红外发光强度随泵浦功率的变化显示了样品的泵浦饱和效应：在较高的功率泵浦条件下，上转换红光和绿光强度对泵浦功率的双对数图像的拟合直线的斜率分别为 0.9 和 0.99，对于双光子效应引起的上转换红光和绿光来说，这个斜率本该接近于 2；近红外发光强度随着泵浦功率的增加反而出现了下降。对于这两个反常的现象，从速率方程出发，基于各种发光机制（激发态吸收—ESA，能量转移—ET，能量反向传递—EBT，无辐射多声子弛豫，辐射衰减），详细推导了Er^{3+}/Yb^{3+}共掺模型下的Er^{3+}的各发光能级的粒子数布居 N 对泵浦功率 P 的依赖关系，理论结果与我们的实验现象相符。

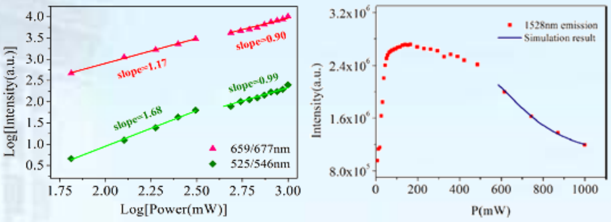

图7. Er^{3+}，Yb^{3+}掺杂的$Y_2Ti_2O_7$纳米晶在975nm激发下，上转换红光和绿光强度对泵浦功率的双对数图像（左）近红外发光强度随着泵浦功率的变化（右）。

Fig7. (Left)Log–log plots of the upconversion emission intensity vs. the excitation power for the Er^{3+}/Yb^{3+} co-doped $Y_2Ti_2O_7$ nanocrystals under 975nm LD excitation; (Right) The pump power dependence of the NIR emission intensity of the nanocrystals samples annealed at 800℃ under 975 nm LD excitation.

Left of Fig. 7 shows the double logarithmic graph of the sample annealed at 800℃ for the dependence of green and red UC emissions integrated intensity on pump power with 975 nm LD excitation. According to the formula: $I_{up} \propto P^m$, where I_{up} is the UC emission intensity, P is the pump laser power, and m denotes the number of laser photons absorbed when emitting an UC photon, and the above analysis, the green and red UC emissions should be two-photon processes, therefore, the m values should be close to 2. However, in left of Fig. 7, the slopes of green and red emissions are 1.68 and 1.17 at low pump power; but under relatively higher pump power, they abnormally drop to 0.99 and 0.90, respectively, which means that the green emissions vary from two-photon processes to one-photon process, and the $^4F_{9/2}$ level is also undergoing change. Right picture of Fig. 7 indicates the $^4I_{13/2}$ energy level has reached saturation when the pump power is about 180mW.

We developed a theoretical model of Er^{3+}/Yb^{3+} co-doped system to have a deep understanding of the power dependence behavior of UC and NIR luminescence and the saturation of the $^4I_{13/2}$ level, which match well with our experimental results.

为适应光谱仪微型化、集成化的发展趋势，详细分析了 MEMS 微镜应用于微型长波近红外光谱仪的方法和涉及的主要问题，例如分光系统的设计、MEMS 微镜的选择、探测器与前置放大电路的设计等。并将 50Hz 谐振频率、峰峰驱动电压为 10V 的 MEMS 微镜、高灵敏度的 InGaAs 单元探测器，结合立特罗式分光光路，设计和实现了 900-2050nm 波段的微型长波近红外光谱仪样机，其中 1000-1965nm 谱段的光谱分辨率介于 9.4-16nm 之间。采用 MEMS 扫描微镜技术后，一方面简化了光谱仪中的复杂机械结构，使尺寸可以更小；另一方面实现了单探测器的长波近红外光谱仪，与阵列长波近红外探测器光谱仪相比，成本有所降低。作为应用实例，此样机成功对纯水以及乙醇-水溶液的长波近红外光谱进行了测量，实现了乙醇-水溶液的浓度预测分析，其中本样机测量的纯水长波近红外光谱与文献相符。

Long Wavelength Near Infrared spectrometer has wide applications. Miniaturization and low-cost are two major goals of the development of LW-NIR spectrometer in the industrial or research community. Under the background that having a trend of spectrometer miniaturization and integration, method and main problems involved in miniaturization of LW-NIR spectrometer through MEMS scanning mirror, such as the design strategy of the light-splitting optical system, selection considerations of the MEMS scanning mirror, design method of the preamplifier circuit, etc, have been presented in detail. A prototype of miniaturized LW-NIR spectrometer, with the spectrum range of detection of 900 to2055nm, is designed and implemented using MEMS scanning mirror, InGaAs single detector unit with high sensitivity. Littrow optical layout is used for its light-splitting optical system, and the spectral resolution is between 9.4 to 16nm at 1000 to 1965nm detection wavelength range. The prototype is successfully applied in LW-NIR spectrum measurement on pure water and ethanol aqueous solution, and a forecast analysis on ethanol aqueous solution concentration is also demonstrated. Through adopting MEMS scanning mirror into the spectrometer system, the complexity of the mechanical scanning fixtures and its controlling mechanism is greatly reduced therefore the size of the spectrometer is reduced. Furthermore, due to MEMS scanning mirror technology, LW-NIR spectrometer with single InGaAs detector is achieved, thus the cost reduction of the NIR spectrometer system is also realized because the expensive InGaAs arrays are avoided.

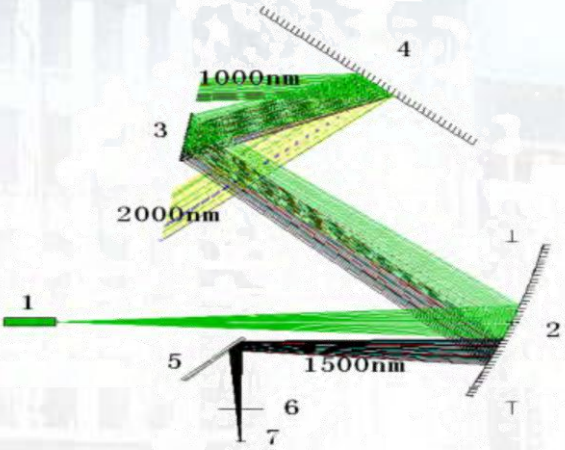

图8. 微型近红外光谱仪采用传统的立特罗式光路分光系统。

Fig8. Optical layout schematic of the spectrometer (including fiber 1, focusing mirror 2, MEMS scanning mirror 3, grating 4, reflector 5, slit 6, detector 7).

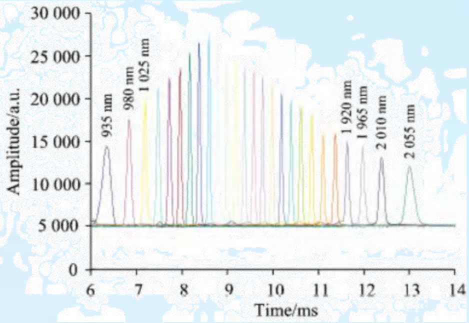

图9. 样机光谱范围和光谱分辨率测试结果。

Fig9. Test result for spectral range and spectral resolution.

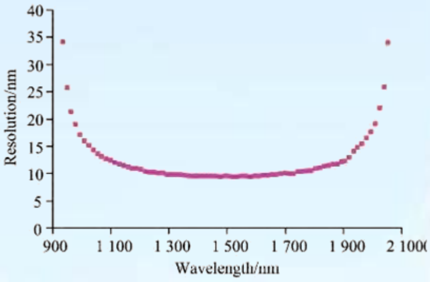

图10. 光谱分辨率随测量波段中心波长变化曲线。

Fig10. Optical resolution varies with wavelength.

为了解决 CCD 不能测量在单次测量中测量全光谱范围的问题，我们提出了一个新的波长拟合算法，结合多项式算法应用到固定光栅的光栅方程。光栅旋转角度和 CCD 像素坐标位置均被关联在我们的波长拟合算法之中。在汞谱线 576.96nm 和 579.07nm 的测试中，应用上述波长拟合算法，我们可以确定在 576.96 nm 时，波长误差为 0.002 到 0.1nm 之间、在 579.07nm 时，波长误差为 0.006 到 0.06nm 之间。计算结果表明，新波长拟合算法可以获得更精确的波长精度。

In order to solve the problem that CCDs cannot measure the full spectral range in a single measurement, we propose a new wavelength-fitting algorithm that combines the polynomial algorithm applied to the fixed grating with grating equation without CCD or spectrum assembling. Both the grating rotating angle and pixel coordinate of the CCD are written in our wavelength-fitting function. With the calibration of the 576.96 and 579.07 nm mercury spectral line, we can determine that wavelength error of 576.96 nm is between 0.002 and 0.1 nm and wavelength error of 579.07 nm is between 0.006 and 0.06 nm. The calculation results show that the new algorithm can gain more precise wavelength accuracy without a complex assembling operation.

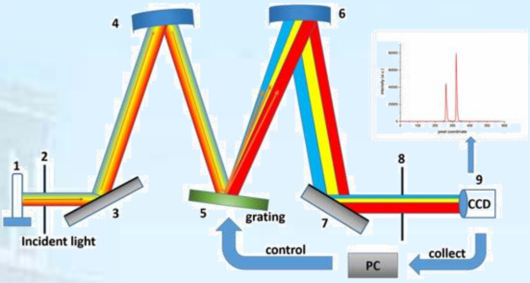

图11. 测试系统光路结构。

Fig11. Optical system for data acquisition, 1. mercury lamb, 2 and 8. tunable slit, 3 and 7. planar mirror, 4 and 6. concave mirror, 5. grating, 9. CCD.

光场调控及其应用/Manipulation of Optical Fields and Its Application

负责人：王慧田

本方向主要开展连续光和飞秒脉冲矢量光场和光学涡旋等新型光场的调控生成、焦场工程、非线性光学效应、微加工和微操纵等方向的研究。取得的代表性成果如下：

In this field, we mainly focused on the generation of the new optical fields such as vector fields and optical vortex by continuous wave and femtosecond pulse; the focusing engineering, the nonlinear effect, the micro manipulation and fabrication by the new optical fields. This year, we obtained some respective results as following.

随着矢量光场各种应用的提出，仍有必要提出更加丰富的矢量光场。我们继续设计并生成了几种非柱对称矢量光场，而且也期望发现其新的性质和应用。这些新型矢量光场包括抛物对称矢量光场、椭圆对称矢量光场等。

As a series of applications of vector optical fields are presented, it is still necessary to enrich the family of vector fields. We continued to design and generate new kinds of vector optical fields without cylindrical symmetry, and we want to find properties and applications of them as well. These new vector optical fields include parabolic-symmetry vector optical fields, elliptic-symmetry vector optical fields and so on.

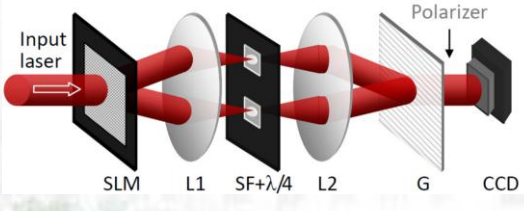

图 1. 矢量光场生成系统示意图。

Fig1. Schematic for generating the vector optical fields.

利用图1所示的矢量光场生成方法，我们设计并生成了如图2所示的抛物对称矢量光场。这种矢量光场的强度沿特定的抛物线保持不变。图3展示了一种抛物对称矢量光场紧聚焦的强度图，其总强度图是一种具有高品质因子的条状光斑。

With the method for the generation of vector fields presented in Fig. 1, we design and generate the parabolic-symmetry vector optical fields, as shown in Fig. 2. The intensity of this kind of vector optical fields reminds the same along certain parabolas. Fig. 3 shows an intensity pattern of the tight focusing fields of parabolic-symmetry vector optical fields, and the total intensity pattern exhibits a flattop sharp line with high figure of merit.

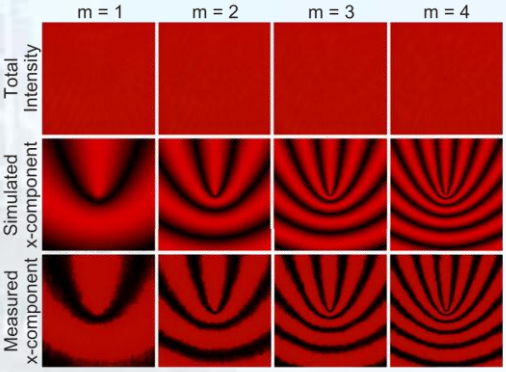

图 2. 抛物对称矢量光场。

Fig2. Parabolic-symmetry vector optical fields.

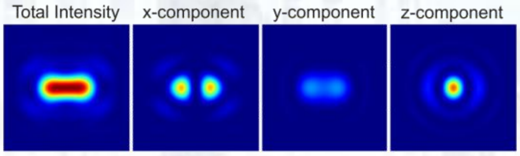

图 3. 抛物对称矢量光场的紧聚焦场光强分布图。

Fig3. Intensity distributions of the tightly focused parabolic-symmetry vector optical fields.

同时，我们还设计和生成了一类具有椭圆对称性的局域线偏振矢量光场，其打破了常见矢量光场的柱对称性，如图 4 所示。这种矢量光场具有较高的灵活性，我们也利用了控制光场的新自由度发现新颖的紧聚焦性质。

Meanwhile, we design and generate a

kind of vector optical fields with elliptical symmetry of linear polarization, which breaks the cylindrical symmetry of most vector optical fields, as shown in Fig. 4. There is more flexibility for this kind of vector fields, and new tight focusing properties are found with the help of new degree of freedom to control the vector fields.

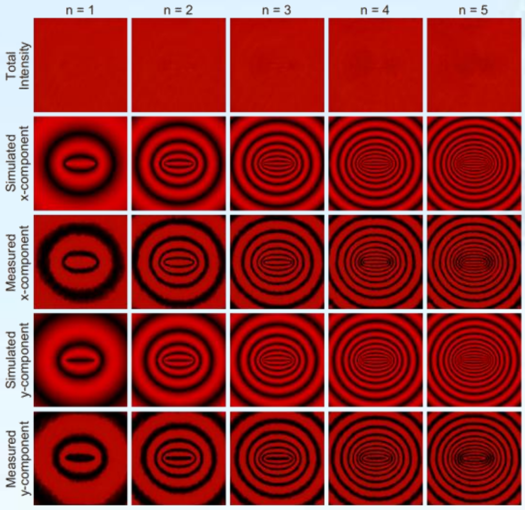

图 4. 椭圆偏振矢量光场。

Fig4. Elliptic-symmetry vector optical fields.

发表论文/Publications in Journal

1. Yonatan Plotnik*, Mikael C. Rechtsman*, Daohong Song*, Matthias Heinrich, Julia M. Zeuner, Stefan Nolte, Natalia Malkova, Jingjun Xu, Alexander Szameit, Zhigang Chen, Mordechai Segev. “Observation of unconventional edge states in ‘photonic graphene’”. Nature Materials 13, 57–62 (2014).[*]
2. Xiang-Feng Zhou, Xiao Dong, Artem R. Oganov, Qiang Zhu, YongJun Tian and Hui-Tian Wang, “ Semimetallic Two-Dimensional Boron Allotrope with Massless Dirac Fermions”, *Phys. Rev. Lett.* 112 , 085502 (2014).
3. Xiang-Feng Zhou, Artem R. Oganov, Xi Shao, Qiang Zhu and Hui-Tian Wang, “ Unexpected Reconstruction of the alpha-Boron (111) Surface”, *Phys. Rev. Lett.* 113, 176101 (2014).
4. Chongpei Pan, Mengxin Ren*, Qunqing Li*, Shoushan Fan, and Jingjun Xu*, “Broadband asymmetric transmission of optical waves from spiral plasmonic metamaterials”, Applied Physics Letters 104, 121112 (2014)
5. Q.-W. Sheng, M. Feng, W. Xin, H. Guo, T.-Y. Han, Y.-G. Li, Y.-G. Liu, F. Gao, F. Song, Z.-B. Liu, and J.-G. Tian, "Tunable graphene saturable absorber with cross absorption modulation for mode-locking in fiber laser," *Applied Physics Letters* 105, 041901 (2014).
6. Zhi-Li Li, Yan-Ge Liu , Min Yan, Wen-Yuan Zhou , Cui-Feng Ying, Qing Ye, Jian-Guo Tian, “A simplified hollow-core microstructured optical fibre laser with microring resonators and strong radial emission” Appl. Phy. Lett. 105(1), 071902 (2014)
7. Zhancheng Li, Shuqi Chen, Chengchun Tang, Wenwei Liu, Hua Cheng, Zhe Liu, Jianxiong Li, Ping Yu, Boyang Xie, Zhaocheng Liu, Junjie Li, and Jianguo Tian, “Broadband diodelike asymmetric transmission of linearly polarized light in ultrathin hybrid metamaterial,” Appl. Phys. Lett. 105, 201103 (2014).
8. L. Rebohle, M. Braun, R. Wutzler, B. Liu, J.M. Sun, M. Helm and W. Skorupa, “Strong electroluminescence from SiO_2-Tb_2O_3-Al_2O_3 mixed layers fabricated by atomic layer deposition”, Appl. Phys. Lett. 104, 251113 (2014). (IF=3.515)
9. F. Xing, G.-X. Meng, Q. Zhang, L.-T. Pan, P. Wang, Z.-B. Liu, W.-S. Jiang, Y. Chen, and J.-G. Tian, "Ultrasensitive Flow Sensing of a Single Cell Using Graphene-Based Optical Sensors," *Nano Letters* 14, 3563-3569 (2014).
10. X.-Q. Yan, J. Yao, Z.-B. Liu, X. Zhao, X.-D. Chen, C. Gao, W. Xin, Y. Chen, and J.-G. Tian, "Evolution of anisotropic-to-isotropic photoexcited carrier distribution in graphene," *Physical Review B* 90, 134308 (2014).
11. Teng-Qian Sun, Qing Ye, Xiao-Wan Wang, Jin Wang, Zhi-Chao Deng, Jian-Chun Mei,Wen-Yuan Zhou, Chun-Ping Zhang, Jian-Guo Tian, “Scanning focused refractive-index microscopy”, Sci. rep. 4, 5647(2014)
12. Ming Yang, Qiang Wu, Zhandong Chen, Bin Zhang, Baiquan Tang, Jianghong Yao, Irena Drevensek-Olenik, and Jingjun Xu, “Generation and erasure of femtosecond laser-induced periodic surface structures on nanoparticle-covered silicon by a single laser pulse ”, Optics Letters, 39(2), 343-346 (2014).
13. Sheng-Xia Qian, Ling-Jun Kong, Yongnan Li, Chenghou Tu and Hui-Tian Wang, “ Recording and reconstruction of vector fields in a Fe-doped $LiNbO_3$ crystal”, *Opt. Lett.* 39, 1917-1920 (2014).
14. Sheng-Xia Qian, Yongnan Li, Ling-Jun Kong, Chenghou Tu and Hui-Tian Wang, “ Phase conjugation of vector fields by degenerate four-wave mixing in a Fe-doped LiNbO3”, *Opt.*

---

[*] 选录论文/Selected papers

Lett. 39, 4907-4910 (2014).

15. Fang Bo, Steven He Huang, Sahin Kaya Ozdemir, Guoquan Zhang, Jjingjun Xu, and Lan Yang, “Inverted-wedge silica resonators for controlled and stable coupling”, Optics Letters 39(7), 1841-1844 (2014).

16. X. Li, P. Wang, F. Xing, X.-D. Chen, Z.-B. Liu, and J.-G. Tian, "Experimental observation of a giant Goos–Hänchen shift in graphene using a beam splitter scanning method," *Optics Letters* 39, 5574-5577 (2014).

17. Zhaocheng Liu, Shuqi Chen, Jianxiong Li, Hua Cheng, Zhancheng Li, Wenwei Liu, Ping Yu, Ji Xia, and Jianguo Tian, “Fully interferometric controllable anomalous refraction efficiency using cross-modulation with plasmonic metasurfaces,” Opt. Lett. 39, 6763 (2014).

18. Yu-E Wu, Zhenhua Wang*, Xinzheng Zhang, Wenhua Li, Ligang Huang, Feng Gao, Wei Li, Qiang Wu, and Jingjun Xu, “Polarization independent broadband femtosecond optical gating using transient Kerr lens effect”, Opt. Express, 22, 6691-6698 (2014)

19. Feng Xia, Xinzheng Zhang*, Meng Wang, Sanming Yi, Qian Liu, and Jingjun Xu, “Numerical analysis of the sub-wavelength fabrication of MTMO grayscale photomasks by direct laser writing”, *Opt. Exp.* 22(14), 16889-16896 (2014)

20. Wenhua Li, Zhenhua Wang*, Xinzheng Zhang, Yu-E Wu, Wenying Liao, Ligang Huang, Feng Gao, Wande Fan, Wei Li, Qiang Wu, and Jingjun Xu, “Convenient ultra-broadband femtosecond optical gating utilizing transient beam deflection effect”, *Opt. Express*, 22, 31417-31425 (2014).

21. Yue Pan, Yongnan Li, Si-Min Li, Zhi-Cheng Ren, Ling-Jun Kong, Chenghou Tu and Hui-Tian Wang, “Elliptic-symmetry vector optical fields”, *Opt. Express* 22, 19302-19313 (2014).

22. Qi Jiwei, Chen Zongqiang, Chen Jing, Li Yudong, Qiang Wu, Xu Jingjun, Sun Qian. “Independently tunable double Fano resonances in asymmetric MIM waveguide structure”, Optics Express, 22(12), 14688-14695 (2014).

23. W. Xin, Z.-B. Liu, Q.-W. Sheng, M. Feng, L.-G. Huang, P. Wang, W.-S. Jiang, F. Xing, Y.-G. Liu, and J.-G. Tian, "Flexible graphene saturable absorber on two-layer structure for tunable mode-locked soliton fiber laser," *Optics Express* 22, 10239-10247 (2014).

24. Tongqing Sun, Pai Shan, Hong Chen, Xuanwen Liu, Hongde Liu, Shaolin Chen, Yaan Cao, Yongfa Kong and Jingjun Xu, “Growth and properties of a noncentrosymmetric polyphosphate $CsLa(PO_3)_4$ crystal with deep-ultraviolet transparency”, CrystEngComm 16(45), 10497-10504 (2014). (IF=3.858)

25. H. Yi, F. Li, L. Wu, L.W. Wu, H.R. Wang, B. Wang, Y. Zhang, Y.F. Kong and J. J. Xu, “Site occupancy and photoluminescence properties of Eu^{3+}-activated $Ba_2ZnB_2O_6$ phosphor ”, RSC Advances, 4, 64244-64251 (2014). (IF=3.708)

26. L. Wu, B. Wang, Y. Zhang, L. Li, H.R. Wang, H. Yi, Y.F. Kong and J.J. Xu, “Structure and photoluminescence properties of a rare-earth free red-emitting Mn^{2+}-activated $KMgBO_3$”, Dalton Trans. 43 (37), 13845-13851 (2014). (IF=4.097) **(Selected as the inside front cover of the issue)**

27. Zhi-Cheng Ren, Sheng-Xia Qian, Chenghou Tu, Yongnan Li and Hui-Tian Wang, “ Focal shift in tightly focused Laguerre–Gaussian beams”, *Opt. Commu*n. 334, 156-159 (2015).

28. Qiangquan Chen, Yiping Zuo, Wei Cai, Bin Zhang, Leiting Pan, Jianghong Yao, Qiang Wu, Jingjing Xu, “Giant field enhancement and resonant wavelength shift through a composite nanostructure”, Optics Communications, 321, 47-50 (2014).

29. Jin Wang, Qing Ye, Zhichao Deng, Wenyuan Zhou, Jianchun Mei, Chunping Zhang, Jianguo Tian, “Application of matching liquid on the refractive index measurementof biotissue: A theoretical and experimental study”, Opt. comm. 319, 36-41(2014)

30. Yi Liang, Yi Hu, Zhuoyi Ye, Daohong Song, Cibo Lou, Xinzheng Zhang, Jingjun Xu, Roberto Morandotti, and Zhigang Chen, "Dynamical deformed Airy beams with arbitrary angles between two wings," J. Opt. Soc. Am. A 31, 1468-1472 (2014)
31. Ying Li, Haitao Liu, Hongwei Jia, Fang Bo, Guoquan Zhang, and Jingjun Xu, "Fully vectorial modeling of cylindrical microresonatorswith aperiodic Fourier modal method", J. Opt. Soc. Am. A 31(11), 2459-2466 (2014).
32. Lei Xu, Yi Yin, Fang Bo, Jingjun Xu, and Guoquan Zhang, "Anomalous refraction in the disordered one-dimensional photonic lattices", J. Opt. Soc. Am B 31(1), 105-109 (2014).
33. Yingdong Han, Feng Song, Qiong Li, Fengxiao Wang, Chengguo Ming, Jianguo Tian, “Broad excitation spectra and bright reddish-orange emission of transparent phosphate glass excited by sunshine for greenhouses”, Optical Materials, 37, 756-759 (2014).
34. Fengxiao Wang, Feng Song, Gong Zhang, Yingdong Han, Qiong Li, Chengguo Ming, Jianguo Tian, “Upconversion and pump saturation mechanisms in Er^{3+}/Yb^{3+} co-doped $Y_2Ti_2O_7$ nanocrystals ”, Journal of Applied Physics, 115, 134310 (2014)
35. Wei Li, Peng Du, Jun Zhang, Shudong Shi, Shujing Liu, Nianjiang Chen, Hong Zhao, Feng Song, “Passivation process in quasi-continuous laser derusting with intermediate pulse width and line-scanning method”, APPLIED OPTICS, 53, 6, 1103-1109 (2014)
36. Haoyu Li, Suyang Fu, Xiaoxuan Xu, Bin Wang, Meng Wang, Xipeng Sun, Senpeng Huang, Tingke Guo, Chunlan Zhao, and Yufang Wang, “New wavelength-fitting algorithm of CCD in the circumstance of grating rotation”, APPL OPTICS 53, 4729-4733 (2014).
37. Yinxiao Xiang, Pidong Wang, Wei Cai*, Cui-Feng Ying, Xinzheng Zhang, and Jingjun Xu*. “Plasmonic Tamm states: dual enhancement of light inside the plasmonic waveguide”, *J. Opt. Soc. Am. B* 31, 2769-2772 (2014)
38. Yinxiao Xiang, Wei Cai*, LeiWang, Cuifeng Ying, Xinzheng Zhang*, and Jingjun Xu, “Design methodology for all-optical bistable switches based on a plasmonic resonator sandwiched between dielectric waveguides”, *J. Opt.* 16, 025003 (2014)
39. Yongnan Li, Zhen-Cheng Ren, Sheng-Xia Qian, Chenghou Tu and Hui-Tian Wang, “Analytical formulae of tightly focused Laguerre–Gaussian vector fields”, *J. Opt.* 16, 2040-8978 (2014).
40. Sheng-Xia Qian, Ling-Jun Kong, Yongnan Li, Chenghou Tu and Hui-Tian Wang, “ Security enhancement of double-random phase encryption by iterative algorithm”, *J. Opt.* 16, 2040-8978 (2014).
41. Wudeng Wang, Yudong Li, Pengwei Xu, Zongqiang Chen, Jing Chen, Jun Qian, Jiwei Qi, Qian Sun, Jingjun Xu, “Polarization-insensitive plasmonic-induced transparency in planar metamaterial consisting of a regular triangle and a ring”, Journal of Optics 16(12), 125013 (2014).
42. Wudeng Wang, Yudong Li, Jingyang Peng, Zongqiang Chen, Jun Qian, Jing Chen, Jingjun Xu, Qian Sun, “Polarization dependent Fano resonance in a metallic triangle embedded in split ring plasmonic nanostructures”, Journal of Optics, 16, 035002 (2014).
43. Xiaoyang Duan, Shuqi Chen, Wenwei Liu, Hua Cheng, Zhancheng Li, and Jianguo Tian, “Polarization-insensitive and wide-angle broadband nearly perfect absorber by tunable planar metamaterials in the visible regime,” J. Opt. 16, 125107 (2014).
44. Wudeng Wang, Yudong Li, Jing Chen, Zongqiang Chen, Jingjun Xu, Qian Sun, “Plasmonic analog of electromagnetically induced transparency in planar metamaterials: manipulation and applications”, Journal of Modern Optics 61(20) 1679-1684(2014).
45. Wenjie Wang,’ Yan Sheng, Xiaoying Niu, Ming Huang, Shoujun Zheng and Yongfa Kong, “Second harmonic Čerenkov radiation in bulk birefringent quadratic medium without any $\chi^{(2)}$ modulation”, Opt. Laser Tech. 58, 16-19 (2014). (IF=1.649)

46. Fen Hu, Leiting Pan*, Kai Zhang, Fulin Xing, Xinyu Wang, Imshik Lee, Xinzheng Zhang, and Jingjun Xu*, “Elevation of extracellular Ca^{2+} induces store-operated calcium entry via calcium-sensing receptors: a pathway contributes to the proliferation of osteoblasts”, *PLoS ONE* 9, e107217 (2014)

47. Tongqing Sun, Yu Zhang, Pai Shan, Zichang Zhang, Shaolin Chen, Yongfa Kong and Jingjun Xu, “Growth, structure, thermal properties and spectroscopic characteristics of Nd^{3+}-doped $KGdP_4O_{12}$ crystal”, PLOS ONE 9(6), e100922 (2014). (IF=3.534)

48. L. Wu, M.Y. Ji, H. R. Wang, Y.F. Kong and Y. Zhang, “Site occupancy and photoluminescence of Sm^{3+} in $KSr_4(BO_3)_3$:Sm^{3+} phosphors”, Opt. Mater. Express 4(8), 1535-1544 (2014). (IF=2.923)

49. Shoujun Zheng, Yongfa Kong, Rong Zhang, Hongde Liu, Shaolin Chen, Ling Zhang, Shiguo Liu, Romano Rupp and Jingjun Xu, “Green light direct writing of ferroelectric domains in Mg-doped $LiNbO_3$”, Opt. Mater. Express 4, 272-279 (2014). (IF=2.923)

50. Shuyan Zhu, Yuxiang Wang, Leiting Pan*, Shuang Yang, Yonglin Sun, Xinyu Wang and Fen Hu, “Involvement of transient receptor potential melastatin-8 (TRPM8) in menthol-induced calcium entry, ROS production and cell death in rheumatoid arthritis rat synovial fibroblasts”, *European Journal of Pharmacology* 725, 1-9 (2014)

51. Guixian Meng, Leiting Pan*, Cunbo Li, Fen Hu, Xuechen Shi, Imshik Lee, Irena Drevenšek-Olenik, Xinzheng Zhang and Jingjun Xu, “Temperature-induced Labelling of Fluo-3 AM Selectively Yields Brighter Nucleus in Adherent Cells”, Biochem. Biophys. Res. Commun. 443, 888-893 (2014)

52. Yu-E Wu, Mengxin Ren*, Zhenhua Wang, Wenhua Li, Qiang Wu, Sanming Yi, Xinzheng Zhang*, and Jingjun Xu, “Optical nonlinear dynamics in ZnS from femtosecond laser pulses”, *AIP Adv.* 4, 057107 (2014)

53. Meng Wang, Chuang Wang, Ye Tian, Jianming Zhang, Chuanfei Guo, Xinzheng Zhang*, Qian Liu*, "Study on optical and electric properties of ultrafine-grained indium films", *Appl. Surf. Sci.* 296, 209–213, (2014)

54. Meng Wang, Ye Tian, Jianming Zhang, Chuanfei Guo, Xinzheng Zhang*, and Qian Liu*, “Raman scattering in In/InOx core-shell structured nanoparticles”, *Chin. Phys. B* 23(8) 087803-4 (2014)

55. Wei Li, Wei Cui, Wenjie Zhang, Andreja Kastelic, Irena Drevensek-Olenik*， and Xinzheng Zhang, "Characterisation of POLICRYPS structures assembled through a two-step process", *Liquid Crystals* 41(9) 1315-1322 (2014)

56. Si-Min Li, Sheng-Xia Qian, Ling-Jun Kong, Zhi-Cheng Ren, Yongnan Li, Chenghou Tu and Hui -Tian Wang, “An efficient and robust scheme for controlling the states of polarization in a Sagnac interferometric configuration”, *Europhysics Letters* 105, 0295-5075 (2014).

57. Yue Pan, Yongnan Li, Zhi-Cheng Ren, Yu Si, Chenghou Tu and Hui-Tian Wang, “Parabolic-symmetry vector optical fields and their tightly focusing properties”, *Phys. Rev. A* 89, 035801 (2014).

58. Ye Zhuo-Yi, Xia Shi-Qiang, Song Dao-Hong, TangLi Qin, and Lou Ci Bo, ”Beam control in the tri-core photonic lattices,” Chinese Phyiscs B, 23(2): 024211 (2014)

59. Yuanmei Gao, Daohong Song , Shanshan Chu and Zhigang Chen，“Artificial graphene and related photonic lattices generated with a simple method”，IEEE Photonics Journal,6,2201806 (2014)

60. Jing Chen, Yudong Li, Zongqiang Chen, Jingyang Peng, Jun Qian, Jingjun Xu and Qian Sun. “Tunable Resonances in the Plasmonic Split-Ring Resonator”, IEEE Photonics Journal, 6(3), 4800706 (2014).

61. Jun Qian, Yudong Li, Jing Chen, Jingjun Xu, and Qian Sun, “Localized Hybrid Plasmon Modes Reversion in Gold−Silica−Gold Multilayer Nanoshells” J. Phys. Chem. C, 118, 8581−8587 (2014).

62. Jun Qian, Zongqiang Chen, Wudeng Wang, Yudong Li, Jingjun Xu, Qian Sun, “Dual Symmetry Breaking in Gold-Silica-Gold Multilayer Nanoshells” Plasmonics, 9,1361–1369 (2014).

63. Yiling Dou, Lei Xu, Bin Han, Fang Bo, Jingjun Xu, and Guoquan Zhang, “Quantum correlation of path-entangled two-photon states in waveguide arrays with defects”, AIP Advances 4, 047117 (2014)..

64. Lei Xu, Hao Yang, Peilong Hong, Fang Bo, Jingjun Xu, and Guoquan Zhang, "Lensless imaging based on coherent backscattering in random media", AIP Advances 4, 087124 (2014)

65. D. Bin, W. Peng, L. Zhi-Bo, C. Xu-Dong, J. Wen-Shuai, X. Wei, X. Fei, and T. Jian-Guo, "Large tunable optical absorption of CVD graphene under total internal reflection by strain engineering," *Nanotechnology* 25, 455707 (2014).

66. Wei-Guo Yan, Ji-Wei Qi, Zu-Bin Li,* Jian-Guo Tian,* "Fabrication and Optical Properties of Au-Coated Polystyrene Nanosphere Arrays with Controlled Gaps," *Plasmonics*, 9(3): 565-571 (2014).

67. Wei-Guo Yan,* Chun-Li Luo, Jian Zhao, Mei-Li Guo, Qing Ye, Zu-Bin Li, Jian-Guo Tian,* Fabrication of Au nanoparticle composite TiO2 shell arrays by controlled decomposition of polymer particles, Superlattices and Microstructures, 7, 371–377 (2014).

68. Huanhuan Zeng, Jin Wang, Qing Ye, Zhichao Deng, Jianchun Mei, Wenyuan Zhou, Chunping Zhang, Jianguo Tian，“Study on the refractive index matching effect of ultrasound on optical clearing of bio-tissues based on the derivative total reflection method”, *Biomed. Opt. Exp.* 5(10), 3482-3493（2014）.

69. Jin Wang, Qing Ye, Zhichao Deng, Wenyuan Zhou, Chunping Zhang, and Jianguo Tian, “Refractive index as an indicator for non-homogeneous solid identification”, Rev. sci. intrum. 85, 016102(2014)

70. Zhi-Li Li, Wen-Yuan Zhou, Yan-Ge Liu, Min Yan, Jian-Guo Tian, “Simplified hollow-core microstructural optical fiber laser with intense output and polarized radial emission,” Proc. SPIE 8960, Laser Resonators, Microresonators, and Beam Control XVI, 89600K (4 March 2014);

71. Blaž Tašič, Aleš Mrze, Miro Huskič, Xinzheng Zhang, and Irena Drevenšek-Olenik*, “Alignment of MoS2 Nanotubes in a Photopolymerizable Liquid−Crystalline Material”, *J. Phys. Chem. C* 118, 26396-26401, (2014). (第五单位)

72. Peng Zhang, Yanlong Yu, Enjun Wang, Jingsheng Wang, Jianghong Yao and Yaan Cao*, “Structure of nitrogen and zirconium co-doped titania with enhanced visible-light photocatalytic activity”, ACS Appl. Mater. Interfaces 6, 4622-4629 (2014) (IF=5.900)

73. Yanlong Yu, Yue Tang, Jixiang Yuan, Qiang Wu, Wenjun Zheng and Yaan Cao*, “Fabrication of N-$TiO_2/InBO_3$ heterostructures with enhanced isible photocatalytic performance”, J. Phys. Chem. C 118, 13545-13551 (2014) (IF=4.835)

74. Yanlong Yu, Peng Zhang, Limei Guo, Zhandong Chen, Qiang Wu, Yihong Ding, Wenjun Zheng and Yaan Cao*, “The design of TiO_2 nanostructures (nanoparticle, nanotube, and nanosheet) and their photocatalytic activity”, J. Phys. Chem. C 118, 12727-12733 (2014) (IF=4.835)

75. Yanlong Yu, Peng Zhang, Yuanjiang Kuang, Yihong Ding, Jianghong Yao, Jingjun Xu and Yaan Cao*, “Adjustment and Control of Energy Levels for $TiO_2-N/ZrO_{2-x}N_x$ with Enhanced

Visible Light Photocatalytic Activity", J. Phys. Chem. C 118, 20982-20988 (2014) (IF=4.835)

76. Bin Yu, Jianhua Deng, Baohui Li and An-Chang Shi, "Patchy nanoparticles self-assembled from linear triblock copolymers under spherical confinement: a simulated annealing study", Soft Matter, 10(35), 6831-6843 (2014) (IF=4.151)

77. Dandan Zhao, Yanlong Yu, Huijin Long and Yaan Cao*, "Improved photocatalytic activity of self-assemble TiO_2 nanobelts with Au nanoparticles", Appl. Surf. Sci. 315, 247-251 (2014) (IF=2.538)

78. Hui Guo, Hua Yu, Aiqing Lao, Lifen Chang, Shaohua Gao, Haoxiong Zhang, Taojie Zhou and Lijuan Zhao, "Investigation of sensitizer ions tunable-distribution in fluoride nanoparticles for efficient accretive three-center energy transfer", J. Appl. Phys. 116, 103503 (2014) (IF=2.185)

79. Wei Li, Di Wu, Yanlong Yu, Peng Zhang, Jing Yuan, Yongqiang Cao, Yaan Cao* and Jingjun Xu, "Investigation on a novel ZnO/TiO_2–B photocatalyst with enhanced visible photocatalytic activity", Physica E 58, 118-123 (2014) (IF=1.856)

80. L. Rebohle, Y. Berencén, M. Braun, B. Garrido, D. Hiller, B. Liu, J. M. Ramírez, J. M. Sun, R. Wutzler, M. Helm and W. Skorupa, "Rare earth doped metal-oxide-semiconductor structures: a promising material system or a dead end of optoelectronic evolution?", ECS Trans. 61(5), 175-185 (2014).

81. Tingting Wu, Lijuan Zhao, Zijian Lan, Lifen Chang, Yiming Li and Hua Yu, "modulation of up- and down-conversion emission by Er^{3+} concentration in Er^{3+}/Yb^{3+} co-doped oxyfluoride glass ceramics", Chin. J. Lumin. 2(35), 131-136 (2014)

82. 吴限，潘雷霆*，刘颖，邢梦溪，张心正，许京军，"多途径介导的小胶质细胞间钙波传递"，生物化学与生物物理进展 41, 179-184 (2014)

83. 谭信辉，蔡卫，冀志超，刘国栋，孟涛，李威，张心正*，"光诱导金纳米颗粒光栅及表面等离子激元的激发"，*中国激光*，41(12) 1202011-5 (2014)。

84. 齐继伟，彭景阳，陈宗强，李玉栋，许京军，孙骞，"外加磁场对掺铁铌酸锂晶体中折射率光栅擦除过程的影响"，人工晶体学报， 43(8), 1895-1900(2014)。

85. 梅剑春，叶青，田建国，"钢管管端内外径测量系统的设计与实现"，光学精密工程 22(4)，815-821(2014)

86. 叶坤涛，董太源，贺文熙，李玉晓，程显明，李广勇，李昊宇，徐晓轩，"基于 MEMS 微镜的长波近红外光谱仪的设计与实现"， 光谱学与光谱分析 34（10），2858-2862（2014）。

87. 王景声，王恩君，于彦龙，郭丽梅，曹亚安*，"三维有序结构 In 掺杂 TiO2 薄膜可见光催化活性的研究"，物理化学学报, 30, 513-519 (2014) (IF=0.886)

88. 林妙玲，赵丽娟，兰子鉴，常丽芬，余华，"氟氧化物微晶玻璃散射效率的研究"，光散射学报 26(4), 1-5 (2014)

89. 杨金凤，黄存新，孙军，徐海霞，张玲，许京军，"铌酸锂晶体锂含量的精确测量研究"，人工晶体学报 43(4), 738-742 (2014).

出版专著：

1. Guoquan Zhang，Daohong Song, Zhibo Liu, Mengxin Ren, Zhigang Chen, JIanguo Tian, Jingjun Xu, Chapter1，English Version："Recent progresses on weak-light nonlinear optics" in *Advances in Nonlinear Optics*, De Gruyter 978-3-11-030430-5 (2014).

2. 张国权，宋道红，刘智波，任梦昕，陈志刚，田建国，许京军，“弱光非线性光学若干新进展”（章节，中文版，书名：非线性光学研究前沿），上海交通大学出版社 978-7-313-11548-5/O (2014)。
3. Hui Guo, Hua Yu, Lijuan Zhao, and Yiming Li, “Structure investigations of rare earth doped nanoparticles: extracted from oxyfluoride glass ceramics by thermal induction and corrosion treatment” in Developments in Corrosion Protection, InTech. 978-953-51-1223-5（2014）

专利/Patents

申请专利/ Patents Applied

[1] 201410012447.0；一种高增益可见和近红外硅基光电探测器及其制备方法；发明；吴强，赵丽，马寅星，杨明，陈战东，潘玉松，栗瑜梅，姚江宏，张心正，许京军。（2014.1.2）

[2] 201410108057.3；一种基于激光直写的微纳区域液晶定向的方法及其系统；发明；张心正，许京军，李威，Irena Drevensek-Olenik，崔伟，石彬，王振华，吴强，孔勇发。（2014.3.19）

[3] PCT/ CN2014/075876；A method and system for liquid crystal alignment in micro/nano region based on laser direct writing；发明 PCT；张心正，许京军，李威，Irena Drevensek-Olenik，崔伟，石彬，王振华，吴强，孔勇发。（2014.4.22）

[4] 201410578885.3；一种基于声光作用的全光纤延迟线切换开关；高峰，黄礼刚，张国权，许京军。（2014.12.1）

[5] 201410289213.0；扭曲角度可控的多层石墨烯结构制备方法；发明；刘智波，陈旭东，田建国；（2014.6.23）

[6] 201410160833.4；基于新型空心微结构光纤的染料激光器　　发明；周文远，李志莉，刘艳格，晏敏，田建国。（2014.4.18）

[7] 201310712517.9；波导光学照明测色探头；发明；徐晓轩，孙希鹏，王斌。（2014.1.15）

[8] 201410012214.0；水体荧光物质测量装置；发明；王斌，付苏阳，徐晓轩，李昊宇，孙希鹏，赵春兰，郭廷珂。（2014.2.11）

授权专利/ Patents Approved

[1] ZL20120196836.4；一种基于石墨烯偏振效应的折射率实时测定方法和装置；发明；刘智波，邢飞，叶青，邓志超，田建国。（2014.8.13）

[2] ZL201210322007.6；一种基于物理吸附的石墨烯薄膜转移方法；发明；刘智波，陈旭东，田建国。（2014.7.9 ）

[3] ZL2012100621421；聚焦全内反射法测量物质折射率分布；　　发明；叶青，孙腾骞，王槿，邓志超，张春平，田建国。（2014.3.26）

[4] ZL2012100424743；钢管管端内外径双臂四探头测量装置及其测量方法；发明　；叶青，梅剑春，田建国。（2014.11.5）

[5] ZL201010207689.7；掺钒铌酸锂晶体；发明；刘士国，董印锋，孔勇发，张玲，陈绍林，许京军。（2014.3.5）

[6] ZL201110022624.x；一种暖白光荧光粉的制备方法和用途；发明；武莉，田澍，季鸣元，张毅。（2014.7.9）

国际合作与交流/International Cooperation and Exchange

来访人员名单/Visitors List

序号	姓名	国家或地区	单位	技术职称	报告题目	来访时间	来访目的
1.	Irena Drevenšek Olenik	斯洛文尼亚	斯特藩研究所	副教授		2014.2.11-18	合作研究
2.	Romano Rupp	奥地利	维也纳大学	教授		2014.2.11-18	合作研究
3.	Sergey N. Bagayev	俄罗斯	Institute of Laser Physics SB RAS	院士	Ultra-precise optical clock of new generation – leap into future	2014.4.29-5.4	工作访问 学术交流
4.	Dmitry Khokhlov	俄罗斯	Moscow State University	教授	Terahertz probing of local electron states in doped lead telluride-based semiconductors	2014.4.29-5.4	工作访问 学术交流
5.	Boris Nyushkov	俄罗斯	Institute of Laser Physics SB RAS	教授	Hybrid highly-nonlinear fiber for spectral supercontinuum	2014.4.29-5.4	工作访问 学术交流
6.	Aleksei Taichenachev	俄罗斯	Institute of Laser Physics SB RAS	副所长	New methods and approaches in high-resolution spectroscopy of ultracold atoms and ion 上	2014.4.29-5.4	工作访问 学术交流
7.	Igor Ryabtsev	俄罗斯	Rzhanov Institute of Semiconductor Physics SB RAS	Head of Laboratory	Laser and microwave spectroscopy of cold Rydberg atoms	2014.4.29-5.4	工作访问 学术交流
8.	Andrey Turlapov	俄罗斯	Institute of applied physics, RAS	博士	Joining Bose and Fermi physics in experiments with ultracold atoms	2014.4.29-5.4	工作访问 学术交流

9.	Kucherik Alexey	俄罗斯	Vladimir State University	博士	Laser-induced nanostructured cluster materials： progress in fabrication of photonics elements associate with macroscopic quantum states	2014.4.29-5.4	工作访问 学术交流
10.	Stella Kutrovskaya	俄罗斯	Vladimir State University	博士	Laser formation of the colloidal systems and controlled deposition of the bimetallic complex on the solid substrate	2014.4.29-5.4	工作访问 学术交流
11.	Victor Zadkov	俄罗斯	Moscow State University	教授	Quantum Optics of quantum emitters (atoms, molecules, quantum dots) in the vicinity of a plasmonic nanoparticle	2014.4.29-5.4	工作访问 学术交流
12.	Blaz Tasic	斯洛文尼亚	斯特藩研究所	博士生		2014.5.2-6.1	合作研究
13.	Qiang (David) Wang	美国	Colorado State University	副教授	Novel, Efficient, and Accurate Methods for Calculating Pressure in Lattice Monte Carlo Simulations	2014.6.12-24	工作访问 讲学
14.	秦国奎	美国	MIT	博士后	Exploration for biosynthesis and processing of new bio-inspired polymer materials with multifunctional applications	2014.06.19-21	交流
15.	Chunlei Guo	美国	The Institute of Optics, University of Rochester	教授	Laser-Matter interactions at high Intensities	2014.07.06-08	交流
16.	石志敏	美国	美国 University of South Florida	助理教授	Tailoring Surface Plasmon Polaritons Using Linear and Nonlinear methods 和 Utilizing Orbital Angular Momentum of Photons for Secure Quantum Communication	2014.8.12-14	工作访问 学术交流
17.	An-Chang Shi	加拿大	McMaster University	教授		2014.9.11-14	工作访问 讲学

18.	Jianzhong Wu	美国	University of California, Riverside	教授	Density Functional Theory: A Chemical Engineering Approach	2014.9.11-14	工作访问学术交流
19.	Mikhail Chamonine	德国	雷根斯堡应用科学大学	教授	International Cooperation in the fields of Microsystems Technology and Optoelectronics	2014.9.20-26	访问交流
20.	Heiko Unold	德国	雷根斯堡应用科学大学	教授	Scientific Talk from the field of current research in Electrical Engineering	2014.9.20-26	访问交流
21.	Rupert Schreine	德国	雷根斯堡应用科学大学	教授	Scientific Talk from the field of current research in Microsystems Technology	2014.9.20-26	访问交流
22.	Andrii ILYIN	乌克兰	乌克兰科学院物理所	研究员	Speeding up "slow" liquid crystals	2014.10.9-11.17	合作研究
23.	杨兰	美国	美国圣路易斯华盛顿大学	副教授	Recent explorations in whispering-gallery microresonators for functional devices	2014.10.12-14	工作访问讲学
24.	Sahin Kaya Ozdemir	美国	美国圣路易斯华盛顿大学	研究员	Controlling light with whispering gallery microcavities	2014.10.13-15	工作访问讲学
25.	Masao Doi	日本	北航，外专千人	教授	Solvent evaporation of a polymer solution	2014.12.10	工作访问学术交流
26.	Luka Cmok	斯洛文尼亚	斯特藩研究所	博士生	Nematic fluctuations in swollen liquid-crystal elastomers	2014.12.11-12.18	合作研究
27.	Hou-Tong Chen	美国	Los Alamos National Laboratory	研究员	Emergent Functionalities in Few-Layer Metamaterials	2014.12.14-18	合作研究
28.	Na Liu	德国	Max-Planck-Institute for Intelligent Systems	教授	Active 3D DNA Plasmonics	2014.12.18-21	合作研究

出访人员名单/Personnel exchange Researchers List

序号	姓名	国家或地区	单位	职称或职位	出访时间	出访目的
1.	薄方	美国	圣路易斯华盛顿大学	访问学者	2013.6.13-2014.8.31	访问交流
2.	李祖斌	美国	Northeastern University	副教授	2013.9-2014.9	访问学者
3.	周向峰	美国	纽约州立大学石溪分校地球科学系	副教授	2014.01-2014.12	合作研究
4.	周文远	美国	南开大学	教授	2014.2.4-11	Phonics West会议
5.	宋峰	美国		教授	2014.3	APS 会议
6.	孙骞	英国	牛津大学、伦敦城市大学	教授	2014.7	访问

研究生交流情况/Personnel exchange Students List

序号	姓名	国家或地区	单位	博士生/硕士生	出访时间	出访目的
1.	廖宏艳	斯洛文尼亚	斯特藩研究所	硕士生	2014.6.22-2014.7.26	合作研究
2.	董校	美国	纽约州立大学石溪分校地球科学系	博士生	2012.10-2014.4	联合培养
3.	孔令军	新加坡	南洋理工大学数理科学学院	博士生	2014.9-2015.3	联合培养
4.	刘悦	美国	Rutgers, The State University of New Jersey	博士生	2012.9	联合培养
5.	李志莉	美国	南开大学	博士生	2014 年 2.4-11	Phonics West 会议

国内、国际会议报告/Talks at Conferences

1 Zhigang. Chen, “Deep penetration of light needles through scattering nanosuspensions", Dynamics Days, South America, Vina del Mar, Chile, November 3-7 (2014). (**Invited talk**)

2 Zhigang. Chen, “Nonlinear optics in nanosuspensions”, Active Photonic Materials VI, SPIE Optics and Photonics Congress, San Diego, August 17-21 (2014). (**Invited talk**)

3 Zhigang. Chen and Daohong. Song “Edge states and pseudospins in photonic graphene”, The 35th Progress in Electromagnetics Research Symposium (PIERS),Guangzhou, China, August 25-28(2014).(**Invited talk**)

4 潘雷霆，李存波，史学琛，张心正，许京军，“长波紫外光辐照对人红细胞和嗜中性粒细胞生理功能的影响”，中国微循环协会血液治疗专业委员会第一届学术大会，苏州，2014.6.27-29。（**邀请报告**）

5 任梦昕，许京军，“超材料的非线性增强及荧光偏振操控”， 第十七届激光科学研讨会，太原，2014.10.20-23。（**大会报告**）

6 蔡卫，“基于石墨烯带的等离激元效应研究”，“Plasmonics and Quantum Nanophotonics”青年学者研讨会，北京（2014.11.30-12.1）。 (**邀请报告**)

7 陈志刚, “Amazing optical spatial solitons",全国光孤子学术研讨会, 广州（2014.11.7-11）。（**特邀报告**）

8 张国权，“耦合波导阵列中光场的类量子调控”，第十六届全国基础光学与光物理学术讨论会，北京（2014.12.11-14）。（**邀请报告**）

9 李勇男，涂成厚，王慧田，“光的角动量研究”，中国物理学会 2014 秋季物理学术会议，哈尔滨（2014.9.12-14）。（**光物理分会邀请报告**）

10 宋峰，“液晶发光研究”，2014 年中俄激光物理会议, 天津（2014.4.30-5.3）（**邀请报告**）

11 孙甲明，“高效率级联式纳米稀土层状掺杂的硅基 MOS 结构电致发光器件”，第五届全国掺杂纳米材料发光性质学术会议（NMLP2014），哈尔滨（2014.8.11-15）（**邀请报告**）

12 李宝会，王铮，“两亲嵌段共聚物在选择性溶剂中自组装的模拟研究”，中国化学会 2014 年大分子体系理论、模拟与计算研讨会，长春（2014.6.17-20）(**邀请报告**)

13 王铮，李宝会，“嵌段共聚物在选择性溶剂中自组装行为的模拟研究”，第九届全国软物质与生命物质物理学术会议，温州（2014.11.7-9）(**邀请报告**)

14 孔勇发，刘士国，田甜，陈绍林，张玲，许京军，“掺钼铌酸锂晶体”，第十七届全国凝聚态光学性质会议，通辽（2014.7.19-22）（**邀请报告**）

15 吴强，杨明，陈战东，赵丽，许京军，“飞秒微构造硅材料的物理及其应用”，第十六届全国基础光学与光物理学术研讨会，北京 （2014.12.12-13）。（**邀请报告**）

16 Fang Bo,Sahin Kaya Ozdemir, Faraz Monifi, Jing Zhang, Guoquan Zhang, Jingjun Xu，and Lan Yang, “Oscillatory Coupling between a Microdisk Resonator and a Tapered Fiber”, 4th Advances in Optoelectronics and Micro/nano-optics (AOM), Xi'an, China, Sep 17-20

(2014) .(oral)

17 Daohong Song, Liqin Tang, Yi Zhu, Mark Ablowitz, Vassilis Paltoglou, Nikolaos K. Efremidis, Jingjun Xu, and Zhigang Chen," Direct observation of "pseudospin"-mediated vortex generation in photonic graphene," CLEO conference, San Jose, California ,June 8-13(2014). (Oral)

18 Shiqiang. Xia, Yuanyuan. Zong, Daohong. Song, L. Tang, and Z. Chen, "Observation of self-trapping and rotation of higher-gap quadruple-like lattice solitons," in Frontiers in Optics,. San Jose, California, United States, October 19-23 (2014). (Oral)

19 Yi Hu, Amirhossein Tehranchi, Stefan Wabnitz, Zhigang Chen, Raman Kashyap, and Roberto Morandotti, "Tunable Raman Soliton Self-Frequency Shift via an Asymmetric Airy Pulse," CLEO: QELS, San Jose, California, United States, June 8-13 (2014). (Oral)

20 Yi Hu, Amirhossein Tehranchi, Stefan Wabnitz, Zhigang Chen, Raman Kashyap, and Roberto Morandotti, "Intra-Pulse Raman Scattering Controlled via Asymmetric Airy Pulses," Advanced Photonics, Barcelona, Spain, July 27-31(2014). (Oral)

21 Leiting Pan, Cunbo Li, Xuechen Shi, Pengchong Jiang, Xinzheng Zhang, Jingjun Xu, "Immuno-suppressive effects of non-lethal UVA (365 nm) irradiation in human neutrophils in vitro", 12th International Conference on Photonics and Imaging in Biology and Medicine, Wuhan, China, June 14-17 (2014). (Oral)

22 Fang Bo, Steven He Huang, S ̧ahin Kaya Ozdemir, Guoquan Zhang, Jingjun Xu, and Lan Yang, "Inverted-wedge silica resonators for controlled and stable coupling", CLEO:2014, San Jose, USA , Jun 8-13 (2014). (poster)

23 Bin Zhang, Qiang Wu, Shibiao Wang, Ming Yang, Yiping Zuo, and Jingjun Xu, "Time-resolved Imaging of Propagation of THz Wave in SRR Metamaterials", CLEO: 2014, The Optical Society, San Jose, United States, June 7-15 (2014). (poster).

24 Zhibo Liu, Xiao-Qing Yan, Jianguo Tian, "The novel graphene-based optical sensor", The 3rd International conference on Frontiers of Optical Coatings, Shanghai, Oct 20-24 (2014). (invited talk)

25 Xiao-Qing Yan, Zhi-Bo Liu, Jun Yao, Xin Zhao, Xu-Dong Chen, Xiang-Tian Kong, Fei Xing, Yongsheng Chen, and Jian-Guo Tian. "polarization-dependent ultrafast optical response in graphene," Graphene 2014, Toulouse, France, May 06-09, 2014 (Poster).

26 Xudong Chen, Zhibo Liu, Wenshuai Jiang, Wei xin, Fei Xing, Peng Wang, Bin Dong, Xiaoqing Yan, Yongsheng Chen, Jianguo Tian. "The Design and Fabrication of Twisted Multilayer Graphene with Fine Tunable Rotated Angle," Graphene 2014, Toulouse, France, May 06-09, 2014 (Poster).

27 Shuqi Chen, Xiaoyang Duan, Haifang yang, Hua Cheng, Junjie Li, Wenwei Liu, Changzhi Gu, and Jianguo Tian, "Polarization insensitive and wide-angle plasmonically induced transparency by planar metamaterial," TechConnect World, Maryland, U.S.A., May 13-16 (2013).

28 Qing Ye, Tengqian Sun, Jin Wang, Xiaowan Wang, Zhichao Deng, Wenyuan Zhou, Chunping

Zhang, Jianguo Tian, “Measurement of refractive index distribution of biotissue by scanning focused refractive index microscopy”, Denver, USA, March 3-7(2014)

29 Jiaming Sun, Ben Liu, Na Li, “Rare earth doped silicon based MOS light emitting devices fabricated by atomic layer deposition technology”, The 2nd International Conference on ALD Applications & 3rd China ALD Conference, Shanghai, China, Oct 15-17(2014). (Invited talk)

30 Zheng Wang, Baohui Li, “Self-assembly of amphiphilic diblock copolymers in selective solvents: a simulation study”, Nanjing, China, Jun 8-12(2014). (Invited talk)

31 Ben Liu, Chunyan Jin, Jiaming Sun, “Structure and photoluminescence of the titanium dioxide films grown by atomic layer deposition using etrakis-dimethylamino titanium and ozone”, The 2nd International Conference on ALD Applications & 3rd China ALD Conference, Shanghai, China, Oct 15-17(2014). (Poster)

32 Zheng Wang, Baohui Li，“A simulation study of self-assembly of amphiphilic diblock in selective solvents”, The 10th Korea-China Bilateral Symposium on Polymer Materials, Busan, Korea, Aug 17-21(2014). (Poster)

33 李文华，吴玉娥，王振华*，吴强，张心正，许京军，“基于瞬态克尔透镜效应的宽带飞秒时间分辨光谱技术”，第十七届全国凝聚态光学性质学术研讨会(OPCM2014)，中国通辽（2014.7.19-22）。（口头报告）

34 罗维维，蔡卫，苏晓强，韩家广，张心正，许京军，“石墨烯微结构太赫兹波段等离激元研究”，第十七届全国凝聚态光学性质学术研讨会(OPCM2014)，中国通辽，（2014.7.19-22）。（口头报告）

35 蔡卫，张心正，王垒，刘鹏翃，许京军*，“Surface Plasmons in Various Graphene Structures”，第十七届全国凝聚态光学性质学术研讨会(OPCM2014)，中国通辽（2014.7.19-22）。（口头报告）

36 王杰，薄方，崔娇，Sahin K.Ozdemir，孔勇发，张国权，Lan Yang，许京军，“多晶铌酸锂晶体和二氧化硅复合腔的制备和表征”，中国物理学会2014年秋季学术会议，哈尔滨（2014.9.11-14）。（口头报告）

37 韩彬，徐雷，张国权，“弱调制一维准周期光子晶格中光束的传输特性”，第十六届全国基础光学与光物理学术讨论会，北京（2014.12.11-14）。（口头报告）

38 高峰，“全光纤声光结构的进展与应用”，第四届全国原子分子光物理青年科学家论坛，山西太原，（2014.10.11-12）。(口头报告)

39 王晓杰，薄方，陈绍林，孔勇发，许京军，张国权，“紫外光诱导掺镁铌酸锂晶体异常电导效应的研究”，第十七届全国凝聚态光学性质学术会议，内蒙古通辽（2014.7.19-22）。（口头报告）

40 徐雷，窦宜领，薄方，许京军，张国权，“双光子路径纠缠态在一维波导阵列中的量子行为研究”，第十六届全国量子光学会议，吉林，延吉 （2014.8.4-6）。（口头报告）

41 徐雷，杨浩，洪佩龙，薄方，许京军，张国权，“无序介质中基于相干背散射效应的无透镜成像研究”，中国物理学会2014年秋季学术会议，黑龙江，哈尔滨 （2014.9.11-14）。（口头报告）

42 齐继伟，李玉栋，李萌，杨刘思扬，许京军，孙骞，“阳极氧化铝的不同形貌及其表面增强拉曼散射效应的研究”，第四届全国原子分子光物理青年科学家论坛，太原（2014.10.11-12)。

43 李莹，王晓鸥，薄方，高峰，张国权，许京军，“镀银膜反楔形玻璃微腔中表面等离子激元模式的调控”，中国物理学会 2014 年秋季学术会议，哈尔滨（2014.9.11-14）。（张贴报告）

44 薄方，王杰，崔娇，Sahin K.Ozdemir，孔勇发，张国权，Lan Yang，许京军“铌酸锂二氧化硅复合微腔的制备、表征和光开关应用”，第四届全国原子分子光物理青年科学家论坛，太原 (2014.10.11-12)。（张贴报告）

45 李利明，“分立型混乱光源的 Hanbury Brown-Twiss 干涉效应”，第十六届全国量子光学学术报告会，延吉（2014.8.3-6）。（张贴报告）

46 李利明，洪佩龙，张国权，“分立型混乱光源的 Hanbury Brown-Twiss 干涉效应”，第十六届全国量子光学学术报告会，延吉（2014.8.3-6）。（张贴报告）

47 李志向，张国权，"电磁感应透明对掺镨硅酸钇晶体的双折射调制 "，第十六届全国量子光学学术报告会，延吉（2014.8.3-6）。（张贴报告）

48 黄礼刚，彭伟华，高峰*，薄方，张国权，许京军，“基于声光可调谐滤波器和锥形光纤的环形腔可调谐激光器”，中国物理学会 2014 秋季学术会议，黑龙江哈尔滨，（2014.9.11-14）。

49 黄礼刚，张文定，彭伟华，高峰*，薄方，张国权，许京军，“压电陶瓷倍频信号驱动声光可调谐滤波器” 中国物理学会 2014 秋季学术会议，黑龙江哈尔滨，（2014.9.11-14）。

50 刘智波，鄢小卿，田建国，“石墨烯光学性质的偏振依赖及其应用”，第十七届全国凝聚态光学性质学术会议，通辽（2014.7.19-22）。

51 钱升霞，李勇男，孔令军，涂成厚，王慧田，“铌酸锂晶体中共轭矢量场的再现”，中国物理学会 2014 秋季物理学术会议，哈尔滨（2014.9.12-14）。（光物理分会口头报告）

52 张会会，蔡孟强，涂成厚，李勇男，王慧田，“基于时变矢量光场阵列制备复杂微纳结构”，中国物理学会 2014 秋季物理学术会议，哈尔滨（2014.9.12-14）。（光物理分会口头报告）

53 潘岳，李思黾，钱升霞，李勇男，涂成厚，王慧田，“Uniform elliptically polarized vector optical fields”，中国物理学会 2014 秋季物理学术会议，哈尔滨（2014.9.12-14）。（光物理分会张贴报告）

54 高旭珍，潘岳，李思黾，李勇男，涂成厚，王慧田，“矢量光场焦场破缺的信息恢复”，中国物理学会 2014 秋季物理学术会议，哈尔滨（2014.9.12-14）。（光物理分会张贴报告）

55 李萍萍，钱升霞，涂成厚，李勇男，王慧田，“掺镁铌酸锂晶体中飞秒辅助反转畴结构的制备”，中国物理学会 2014 秋季物理学术会议，哈尔滨（2014.9.12-14）。（光物理分会张贴报告）

56 付苏阳，褚航，李昊宇，徐晓轩，王斌，“一种基于颜色传感酶致色变的血液中酒精含量测量方法研究”，2014 全国光电技术与系统学术会议，南京（2014.10.25-27）

57 刘宏德，王晓慧，张荣，葛新宇，郑大怀，孔勇发，许京军，“铌酸锂晶体中光诱导铁电畴翻转研究”，第十七届全国凝聚态光学性质会议，通辽（2014.7.19-22）

58 郑大怀，孔勇发，张心铭，刘士国，张玲，许京军，“铋镁双掺铌酸锂晶体生长及光折变性能研究”，第十七届全国凝聚态光学性质会议，通辽（2014.7.19-22）

59 张心铭，孔勇发，刘士国，陈绍林，张玲，许京军，“氯化钠掺杂铌酸锂晶体的生长及光折变性能研究”，第十七届全国凝聚态光学性质会议，通辽（2014.7.19-22）

60 张冠南，崔娇，孔勇发，“脉冲激光沉积法在 Si 衬底上生长 c 轴取向铌酸锂薄膜”，第十七届全国凝聚态光学性质会议，通辽（2014.7.19-22）

61 要佳莹，孔勇发，张立新，胡振芃，许京军，“铌酸锂晶体缺陷和能带结构的第一性原理计算”，第十七届全国凝聚态光学性质会议，通辽（2014.7.19-22）

62 郑大怀，孔勇发，刘士国，张玲，许京军，“铋镁双掺铌酸锂晶体的抗光损伤增强及相匹配温度展宽”，第十六届全国基础光学与光物理学术讨论会，北京（2014.12.11-13）

63 于彦龙，曹亚安，“N-TiO2/InBO3 复合催化剂的制备及其光催化性能”，第 3 届光功能材料与光电化学学术研讨会，长春（2014.8.9-11）

64 靳亚粉，李娜，孙甲明*，“溶胶-凝胶法制备高效率 SiO2:Tb 绿色硅基发光材料”，第五届全国掺杂纳米材料发光性质学术会议（NMLP2014），哈尔滨（2014.8.11-15）（张贴报告）

学术组织与期刊任职/Academic Service

国内外学术组织任职/Service to the Professional Societies

序号	姓名	任职机构	职位	任期
1	许京军	中国高校知识产权研究会	副理事长	2008-
2	许京军	中国光学学会	理事	2006-
3	许京军	天津市光学学会	副理事长	2010-
4	许京军	天津市激光技术学会	副理事长	2010-
5	许京军	应用光学国家重点实验室	主任	2009-
6	孔勇发	中国材料研究学会青年工作委员会	理事	2011-2014
7	宋　峰	天津市物理学会	常务理事兼秘书长	2008.7-
8	宋　峰	天津市激光技术学会	副理事长	2009-2014
9	田建国	天津市光学学会	常务理事	
10	孙　骞	天津市光电子学会	常务理事	
11	孙　骞	中国光学学会光电技术委员会	委员	2006-
12	孙　骞	教育部实验室建设专家委员会	委员	2013-2017
13	张天浩	天津市照明学会	常务理事	2008-
14	宋　峰	中国仪器仪表学会光机电技术与系统成分会	常务理事	2007.6-
15	孔勇发	中国硅酸盐学会晶体生长与材料分会	理事	2012-2015
16	孙甲明	中国物理学会发光分会	委员	2010－2014
17	孙甲明	全国掺杂纳米发光学会	委员	2010－2014
18	孙甲明	中国电工技术学会半导体光源系统专委会	委员	2014.10－
19	徐晓轩	中国仪器仪表学会近红外光谱专业分会	专业委员	2013－2016
20	孙　军	国家标准化管理委员会人工晶体标准化技术委员会	委员	2012.9－
21	潘雷霆	中国微循环学会微循环与血液治疗专业委员会	常委	
22	潘雷霆	中国生物物理学会自由基生物学与自由基医学学会	青年委员	
23	徐晓轩	中国仪器仪表学会物理光学仪器专业委员会	专业委员	2013－2016
24	宋　峰	科学出版社	第二届教材建设委	2010.10-2015.12

			员会物理学科委员	
25	宋　峰	信息科学部	第五届专家咨询委员会学术秘书	2011.4-2014.4
26	宋　峰	“军用固体激光技术”国防重点实验室学术委员会	委员	2007.8-
27	宋　峰	全国中学生物理竞赛委员会	常委	2010.4-
28	孙　骞	喀什师范学院	兼职教授	2014-2015
29	张国权	OSA	高级会员（Senior Member）	2013-

国内外期刊任职/Service to the Journals

序号	姓名	任职机构	职位	任期
1	许京军	journal of Optics	topic editor	
2	许京军	Frontiers of Physics in China	编委	2008-2011
3	宋　峰	Applied Optics	编委	2009-2012
4	吴强	Scientific Reports	Topic Editor	
5	李宝会	《Scientific Reports》	Editorial Board Member	2014-2015
6	许京军	《光学学报》	副主编	2008-
7	宋　峰	《大学物理》	副主编	2009.5-
8	许京军	《红外与毫米波学报》	编委	
9	许京军	《物理》	编委	2007-2011
10	许京军	《物理学进展》	编委	2009-2012
11	许京军	Chinese Physics Letters	编委	2009-
12	许京军	《中国光学与应用光学》	编委	2008-
13	孔勇发	《激光技术》	编委	2010-2013
14	孔勇发	《人工晶体学报》	编委	2012-2016
15	张国权	《激光技术》	编委	2006-2018
16	张国权	《激光与光电子学进展》	编委	2010-
17	宋　峰	《清洗世界》	编委	2011-
18	张心正	《激光技术》	编委	2015-2018
19	孙骞	《激光技术》	编委	2012-2016

获奖情况/Awards & Honors

获奖教师/Award for excellent teachers

天津市“青年千人”
入选者：胡　毅

天津市“131”创新性人才培养工程第三层次人选
入选者：武　莉　吴　强

南开大学“百名青年学科带头人培养计划”
入选者：胡　毅

南开百名优秀青年学术带头人
入选者：蔡卫

获奖学生/Award for excellent students

中国物理学会 2014 秋季物理学术会议优秀张贴报告：黄礼刚
中国物理学会 2014 秋季物理学术会议优秀论文奖：潘岳
“南开十杰”获得者：钱升霞
南开大学党员青年先锋之“学术科研先锋“：潘岳

研究生国家奖学金：　博士生：钱升霞　于彦龙

　　　　　　　　　　硕士生：董　斌　曾欢欢

南开大学优秀研究生党员标兵：任志成
南开大学优秀毕业生：韦　晨
南开大学三好学生：潘　岳

南开大学奖学金：

特等奖学金：钱升霞
一等奖学金：吴玉娥　李　莹　陈旭东　孙腾谦　潘　岳　韩迎东　李昊宇
二等奖学金：潘崇培　王　萌　夏　峰　左一平　马增红　杨　浩　辛　巍　王晓婉
　　　　　　李健雄　蔡孟强　张会会　李　琼　落爱青
三等奖学金：于　萍

学位论文/Dissertations

1. 博士学位论文 Dissertation for Doctoral Degree

[1] 谭信辉，表面等离子激元的激发和相干性研究；导师：Romano Rupp

[2] 向吟啸，基于表面等离子体激元的新型器件功能与光学效应研究；导师：许京军

[3] 刘鹏翃，石墨烯微结构的表面等离子体学特性研究；导师：许京军

[4] 梁毅，弱光非线性传播及其应用研究；导师：许京军

[5] 杨明，飞秒激光诱导硅表面微纳结构研究；导师：许京军、吴强

[6] 陈战东，飞秒激光改性硅材料的物理机理及其性质研究；导师：曹亚安、吴强

[7] 洪佩龙，基于多路径叠加的光学高阶干涉效应；导师：张国权

[8] 徐雷，无序微结构体系中的光聚于及其应用；导师：张国权

[9] 窦宜领，光在一维耦合波导阵列中的量子传输行为与相关特性；导师：张国权

[10] 邢飞，全内反射下石墨烯的光学性质及应用；导师：田建国

[11] 李思黾，光场调控与非线性光学效应研；导师：王慧田

[12] 韦晨，3 μm中红外波段调Q/锁模Er3+-ZBLAN光纤激光器以及超连续谱产生的研究；导师：宋峰

[13] 赵红艳，金属纳米颗粒对中药有机成分蛇床子素和稀土离子（Eu^{3+})发光影响的研究；导师：宋峰

[14] 刘加东，金属纳米粒子光学特性及对分子发光的影响；导师：宋峰

[15] 李伟，激光清洗锈蚀的机制研究和设备开发；导师：宋峰

[16] 张荣纯，发展固体核磁共振新方法研究高分子复杂凝聚态结构与动力学；导师：李宝会

[17] 王景声，掺杂二氧化钛的结构和掺杂机理的研究；导师：曹亚安

[18] 郭丽梅，TiO_2基催化剂和硼酸盐催化剂的制备与光催化还原 CO_2合成 CH_4的研究；导师：姚江宏

[19] 刘敏，稀土掺杂氟氧化物玻璃和微晶玻璃形成机理及应用；导师：赵丽娟

[20] 龚亮，量子点结构与微波烧结粉体 ZnO 的数值模拟研究；导师：舒永春

2. 硕士学位论文 Dissertation for Master Degree

[1] 刘颖，基于耗散结构的细胞间钙信号通讯的理论模拟研究，导师：潘雷霆

[2] 杨淑英，紫外光和可见光辐照对细胞致死作用的研究，导师：潘雷霆

[3] 陈庆全，声子极化激元在铌酸锂晶体中的产生和调控的数值模拟；导师：吴强

[4] 曹天翔，聚合物纳微结构的光学加工形貌特性研究；导师：张心正

[5] 崔伟，聚合物液晶复合材料制备及其性能研究；导师：张心正

[6] 彭景阳，基于开口微环谐振器的近场光子学捕获；导师：孙骞

[7] 王杰，微米尺寸铌酸锂晶体回音廊模式微腔的制备及其非线性光学研究；导师：薄方

[8] 刘亭，回音廊模谐振腔性能及其应用的研究，导师：禹宣伊

[9] 辛巍，基于石墨烯的可调被动锁模光纤激光器的研究；导师：刘智波

[10] 王鹏，全内反射结构下石墨烯光学性质的偏振依赖性研究；导师：刘智波

[11] 蒋文帅，氧化还原石墨烯纳米球壳结构的柔性电子研究；导师：刘智波

[12] 高赫，基于压缩感知的光谱成像技术的应用研究；导师：周文远

[13] 陈贵阳，矢量光场的紧聚焦特性及其焦场调控的研究；导师：宋峰

[14] 郜惠斌，高功率连续激光对半导体和金属材料的温升、应力及融化效应研究；导师：宋峰

[15] 王立超 ，LD 泵浦 Nd: YAG 固体激光器热效应分析及简化传播圆理论应用的研究；导师：宋峰

[16] 孙希鹏，金属纳米结构 SERS 基底的制备及其活性研究；导师：徐晓轩

[17] 张逍遥，铌酸锂晶体光子学微结构及其机理研究；导师：孔勇发

[18] 解雅洁，高均匀性高掺镁铌酸锂晶体的生长及光学性能研究；导师：孔勇发

[19] 秦娇夷，嵌段共聚物在溶液中自组装形态的模拟退火研；导师：李宝会

[20] 史更新，环形聚合物刷体系标度关系及自组装形态的 Monte Carlo 模拟研究；导师：李宝会

[21] 张荣，铌酸锂晶体光致铁电畴反转的研究；导师：孔勇发/刘宏德

[22] 唐悦，ZnSn(OH)6 和 PbBiO$_2$Cl 的水热法制备及其光催化性质的研究；导师：曹亚安

[23] 黎莎，染料敏化钴和锡/硼双掺杂二氧化钛薄膜电极的性能研究；导师：曹亚安

[24] 武迪，二氧化钛/钒酸盐复合催化剂光催化二氧化碳合成甲烷的研究；导师：曹亚安

[25] 郝冰雪，核壳量子点异质结类型调控及载流子动力学过程研究；导师：姚江宏

[26] 张会平，稀土掺杂多孔硅发光性质的研究；导师：姚江宏

[27] 吴婷婷，Er^{3+}/Yb^{3+}共掺氟氧化物玻璃陶瓷上下转换发光的调控；导师：赵丽娟

[28] 戈进，氟氧化物玻璃陶瓷微晶结构和掺杂引起的结构畸变的研究；导师：赵丽娟

[29] 徐海霞，铌酸锂晶体光学加工的研究；导师：张玲

[30] 王立伟，掺铅铌酸锂晶体；导师：刘士国

[31] 李小静，MO-K$_2$O-B$_2$O$_3$（M=Ca, Ba, Sr）体系相关系及发光性能研究；导师：武莉

[32] 吴学谦，新型钨酸盐化合物的合成、结构及功能性的研究；导师：孙同庆

[33] 高玲玲，基于二阶姜-泰勒效应的非中心对称含铋钒酸盐的探索；导师：姚江宏/孙同庆

[34] 郭辉，氟化物纳米晶中基于稀土浓度诱导结构相变对能量传递过程的研究；导师：余华